

Label-Efficient Deep Learning in Medical Image Analysis: Challenges and Future Directions

Cheng Jin*, *Student Member, IEEE*, Zhengrui Guo*, *Student Member, IEEE*, Yi Lin, Luyang Luo, *Member, IEEE*, and Hao Chen, *Senior Member, IEEE*

Abstract—Deep learning has seen rapid growth in recent years and achieved state-of-the-art performance in a wide range of applications. However, training models typically requires expensive and time-consuming collection of large quantities of labeled data. This is particularly true within the scope of medical imaging analysis (MIA), where data are limited and labels are expensive to be acquired. Thus, label-efficient deep learning methods are developed to make comprehensive use of the labeled data as well as the abundance of unlabeled and weak-labeled data. In this survey, we extensively investigated over 300 recent papers to provide a comprehensive overview of recent progress on label-efficient learning strategies in MIA. We first present the background of label-efficient learning and categorize the approaches into different schemes. Next, we examine the current state-of-the-art methods in detail through each scheme. Specifically, we provide an in-depth investigation, covering not only canonical semi-supervised, self-supervised, and multi-instance learning schemes, but also recently emerged active and annotation-efficient learning strategies. Moreover, as a comprehensive contribution to the field, this survey not only elucidates the commonalities and unique features of the surveyed methods but also presents a detailed analysis of the current challenges in the field and suggests potential avenues for future research.

Index Terms—Medical Image Analysis, Label-Efficient Learning, Semi-Supervised Learning, Self-Supervised Learning, Multi-Instance Learning, Active Learning, Annotation-Efficient Learning, Weakly-Supervised Learning.

1 INTRODUCTION

COMPUTER-AIDED medical image analysis (MIA) plays a more and more critical role in achieving efficiency and accuracy in the early detection, diagnosis, and treatment of diseases. In recent years, MIA systems powered by deep learning (DL) have provided a more objective approach to learning from large and heterogeneous medical image datasets and improved disease diagnosis accuracy. However, DL models require abundant precisely annotated data to effectively capture anatomical heterogeneity and disease-specific traits [1] due to their data-driven nature. Unfortunately, due to a shortage of available annotators [2], there is a significant gap between the demand for annotation and the available annotated datasets. Hence, the urgency to curtail annotation expenses, expedite the annotation procedure, and alleviate the load on annotators has emerged as a crucial hurdle in DL-based MIA tasks. Traditional fully-supervised DL methods, on the other hand, depend solely on comprehensively annotated datasets. Recently, strategies based on semi-supervised, self-supervised, and multi-instance learning have been widely utilized to maximize the utility of existing medical data that may be only partially annotated by point, scribble, box, pixel-wise, *etc.* or even completely unannotated data. In this paper, we dub these methods as label-efficient learning. As seen in Fig. 1, label-

efficient learning methods have significantly proliferated in recent years. Meanwhile, label-efficient learning methods excelling in other MIA tasks like denoising, image registration, and super-resolution have also been rising beyond common classification, segmentation, and detection.

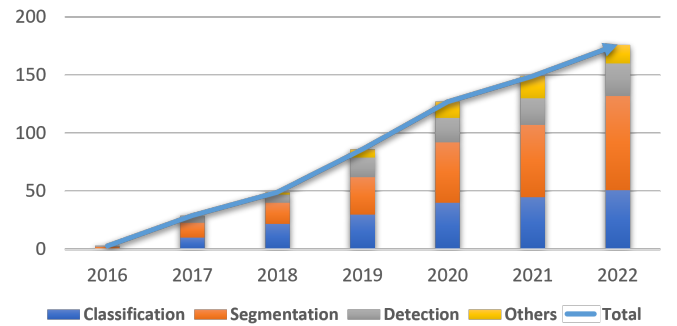


Fig. 1. The number of published label-efficient learning papers in MIA from 2016 to 2022.

Several surveys related to label-efficient learning in medical image analysis have been published in recent years. Cheplygina *et al.* [3] categorized methods under supervised, semi-supervised, multi-instance, and transfer learning and named them “not-so-supervised” learning, while Budd *et al.* [4] surveyed human-in-the-loop strategies for MIA tasks. However, methods in these surveys are either limited in scope or lag behind the current trends. To address this issue, we conduct a systematic review of current label-efficient methodologies, of which the outline is depicted in Fig. 2.

Aiming to provide a comprehensive overview and future

* Equal contribution

- The authors are with the Department of Computer Science and Engineering, The Hong Kong University of Science and Technology, Kowloon, Hong Kong. Hao Chen is also with the Department of Chemical and Biological Engineering, The Hong Kong University of Science and Technology, Kowloon, Hong Kong. (Corresponding author: Hao Chen)
E-mail: {cheng.jin, zhengrui.guo, yi.lin}@connect.ust.hk, cseluyang@ust.hk, jhc@cse.ust.hk

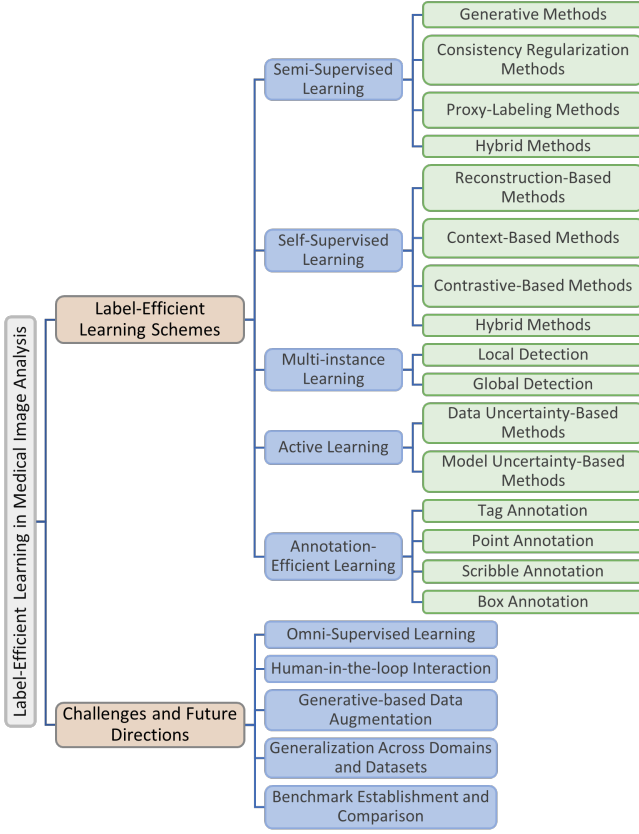


Fig. 2. The taxonomy for label-efficient MIA research.

challenges of label-efficient learning methods in MIA, we review more than 300 quality-assured and recent label-efficient learning methods based on semi-supervised, multi-instance, self-supervised, active, and annotation-efficient learning strategies. To pinpoint pertinent contributions, Google Scholar was employed to search for papers with related topics. ArXiv was combined through for papers citing one of a set of terms related to label-efficient medical imaging. Additionally, conference proceedings like CVPR, ICCV, ECCV, NIPS, AAAI, and MICCAI were scrutinized based on the titles of the papers, as well as journals such as MIA, IEEE TMI, and Nature Bioengineering. References in all chosen papers were examined. When overlapping work had been reported in multiple publications, only the publication(s) considered most significant were incorporated. We anticipate that the search terms used would encompass most, if not all, of the work integrating deep learning methods.

To the best of our knowledge, this is the first comprehensive review in the field of label-efficient MIA. In each learning scheme, we formulate the fundamental problem, offer the necessary background, and display the experimental results case by case. With the challenges proposed at the end of the survey, we explore feasible future directions in several branches to potentially enlighten the follow-up research on label-efficient learning.

The remainder of this paper is organized as follows. In Section 2, the necessary background and categorization is presented. In Sections 3–7, we introduce the primary label-efficient learning schemes in MIA, including semi-

supervised learning in Section 3, self-supervised learning in Section 4, multi-instance learning in Section 5, active learning in Section 6, and annotation-efficient learning in Section 7. We discuss the existing challenges in label-efficient learning and present several heuristic solutions for these open problems in Section 8, where promising future research directions are proposed as well. Finally, we conclude the paper in Section 9.

2 BACKGROUND AND CATEGORIZATION

In this section, we review the background of the learning schemes covering label-efficient learning. In addition, we present the categorization of each learning scheme in MIA.

2.1 Semi-Supervised Learning

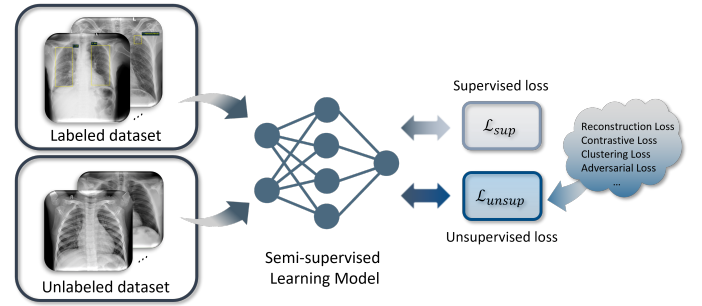


Fig. 3. Overview of semi-supervised learning paradigm. Semi-SL includes a small set of labeled data and a large amount of unlabeled data to conduct learning jointly, aiming at leveraging the unlabeled data to boost learning performance. Semi-SL typically seeks to optimize the combination of a supervised loss function \mathcal{L}_{sup} and an unsupervised loss function \mathcal{L}_{unsup} .

As illustrated in Fig. 3, **Semi-supervised learning (Semi-SL)** introduces an additional unlabeled dataset to help the model learn task-related invariant features and aim to achieve better performance than supervised learning. Concretely, one has a set of L labeled data points $X_L = \{(x_i, y_i)\}_{i=1}^L$, in which x_i represents the raw data sample from the given input space \mathcal{X} and y_i is the corresponding label. In the meantime, an unlabeled dataset $X_U = \{x_i\}_{i=L+1}^{L+U}$ with a much larger scale is involved, *i.e.*, $U \gg L$. And $X = X_L \cup X_U$ denotes the entire dataset. During the training process, the optimization problem¹ that Semi-SL intends to solve is defined as:

$$\min_{\theta} \sum_{(x,y) \in X_L} \mathcal{L}_s(x, y, \theta) + \alpha \sum_{x \in X_U} \mathcal{L}_u(x, \theta) + \beta \sum_{x \in X} \mathcal{R}(x, \theta), \quad (1)$$

where θ represents the model parameters, \mathcal{L}_s is the supervised loss function, \mathcal{L}_u represents the unsupervised loss function, and \mathcal{R} is a regularization term. In addition, $\alpha, \beta \in \mathbb{R}^+$ control the trade-off between unsupervised loss \mathcal{L}_u and regularization term \mathcal{R} .

Based on how the model incorporates and leverages unlabeled data, we will discuss the categories of Semi-SL methods and their applications in MIA starting from **proxy-labeling methods**, followed by **generative methods**,

1. Several assumptions and prior knowledge of Semi-SL can be referred to Appendix A.1.

consistency regularization methods, and finally **hybrid methods**. Meanwhile, we present a brief summary of the representative publications in Tab. 1².

2.2 Self-Supervised Learning

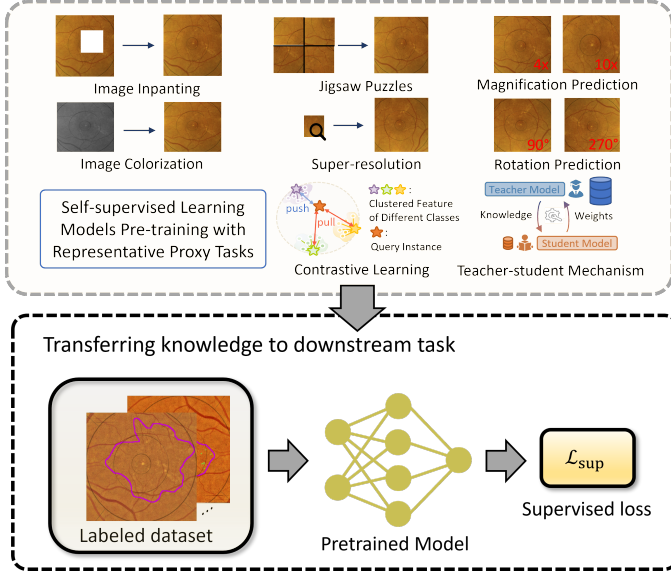


Fig. 4. Overview of self-supervised learning paradigm. Self-SL aims to learn a pre-trained model by developing various proxy tasks based solely on unlabeled data. Then the pre-trained model can be fine-tuned on different downstream tasks with labeled datasets. The process of Self-SL creates a generalizable model based on proxy tasks and avoids the overfitting which might occur if the model is trained solely with the labeled datasets of downstream tasks.

Self-supervised learning (Self-SL) was proposed to extract and learn the underlying features of a large-scale unlabeled dataset without human annotation. Generally, Self-SL methods build proxy tasks for the model to learn the latent features and representations from a massive amount of unlabeled data, thus facilitating the performance on downstream tasks, as shown in Fig. 4. Concretely, the training procedure of Self-SL can be divided into two stages: pre-training with proxy tasks and fine-tuning on different downstream tasks. During the pre-training phase, researchers design proxy tasks that satisfy the following two properties [5]: (1) The label of the input data for the proxy task can be generated automatically by the data itself; (2) the neural network can learn related representations or features of the input data by solving the proxy task.

After the pre-training with proxy tasks, the learned representations will be utilized to solve the main task. The advantages of utilizing proxy tasks are two-fold: on the one hand, by defining particular tasks, the model can be targeted to learn features or representations of the specific studied data; on the other hand, by using a large amount of unlabeled data for pre-training, the model can significantly avoid overfitting during fine-tuning compared to supervised learning, especially for small datasets, in downstream training.

2. The summary of all collected publications in Semi-SL and the rest of the learning schemes can be referred to in Appendix C.

Based on the characteristics of the proxy tasks, we group the mainstream Self-SL methods in MIA into the following four general categories: **Reconstruction-Based Methods**, **Context-Based Methods**, **Contrastive-Based Methods**, and **Hybrid Methods** with a summary of the representative publications in Tab. 2.

2.3 Multi-instance Learning

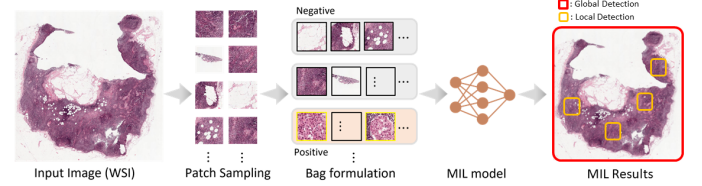


Fig. 5. Overview of multi-instance learning paradigm. The inputs are cut into patches and selected patches are used to form bags, in which each patch is an instance. Given the bag-level labels, the model are trained to predict the category of bags, instances, and/or the original inputs.

In **multi-instance learning (MIL)**, the concept of a *bag* is introduced. A bag X_i is composed of k instances: $X_i = \{x_{i,1}, x_{i,2}, \dots, x_{i,k_i}\}$, where $x_{i,j}$ denotes an instance in bag X_i , and the training dataset \mathcal{X} consists of N bags: $\mathcal{X} = \{X_1, X_2, \dots, X_N\}$. Next, suppose $Y_i \in \{1, 0\}$ and $y_{i,j} \in \{1, 0\}$ are the labels of bag X_i and the instance $x_{i,j}$ inside it, respectively, in which 1 denotes positive and 0 denotes negative for the binary classification scenario. Two common assumptions can be made based on this basic definition of MIL:

- If bag X_i is positive, then there exists at least one positive instance $x_{i,m} \in X_i$ and $m \in \{1, 2, \dots, k_i\}$ is unknown. This assumption can be summarized as: if $Y_i = 1$, then $\sum_{j=1}^{k_i} y_{i,j} \geq 1$.
- If bag X_i is negative, then all the instances in X_i are negative, namely, if $Y_i = 0$, then $\sum_{j=1}^{k_i} y_{i,j} = 0$.

Based on the assumptions, MIL methods can perform both bag-level and instance-level tasks (illustrated in Fig. 5), with the latter often used in weakly-supervised learning. Concretely, MIL algorithms leverage the instances to identify positive or negative bags, which contributes not only to the image-level diagnosis but also to precise abnormal region detection and localization. This great interpretability of the MIL algorithm fits well in MIA, as both the global structure and local details are crucial components for solving such problems.

In this survey, we categorize MIL methods that aim at detecting all the particular target patterns in the data, such as every patch with a special disease manifestation in a large histopathology image, as **local detection**; and methods that aim at simply detecting whether or not the particular target patterns exist in the given sample as **global detection**. Note that taxonomy is in line with the methodology of MIL, *i.e.*, to classify bag-level label (global detection) or to classify instance-level label (local detection). Tab. 3 presents an overview of the representative publications of each method.

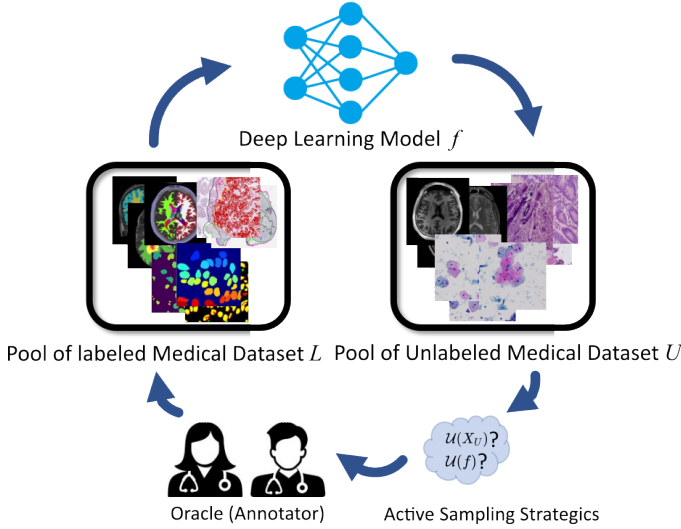


Fig. 6. Overview of active learning paradigm. In a cycle, a deep learning model f is trained from a labeled medical dataset X_L . Then, active sampling strategies based on different criteria (i.e., data uncertainty $\mathcal{U}(X_U)$, model uncertainty $\mathcal{U}(f)$) are implemented to select the data that is most valuable to the model from unlabeled medical dataset X_U . Finally, oracles are employed to annotate the selected data.

2.4 Active Learning

Active learning (AL) is a relatively understudied area in the MIA field. It attempts to maintain the performance of a deep learning model while annotating the fewest data with the help of an oracle, which resonates with the philosophy of label-efficient learning, *i.e.*, how to effectively use noisy, limited, and unannotated data throughout the deep learning process. More specifically, its goal is to select the most valuable samples and forward them to the oracle (*e.g.*, human annotator) for labeling to improve the generalization capability of the model. In active learning (AL) practice, the measurement of annotation uncertainty using various strategies is often considered as the metric for sample value. Meanwhile, in order to preserve the network’s generalization capability, different mechanisms have been developed to ensure that the sampled images are distributed diversely.

As Fig. 6 illustrates, before the start of the data selection process, a deep learning model is initialized or pre-trained from a labeled dataset X_L with its corresponding parameter θ . After that, AL sampling algorithms construct an uncertainty metric \mathcal{U} for each item of unlabeled dataset X_U . This metric determines whether an oracle is required for annotation, and we denote this newly annotated dataset as $X_{L'} \subset X_U$. Then the network model will either use the combined labeled data $X_L = X_L \cup X_{L'}$ to train from scratch or only use them to fine-tune the model. Denoting the fully labeled version of X_U as X_U^* , the goal of AL is to build a model $f(\theta | X_L^*)$ with $|X_L^*| \ll |X_U^*|$ to perform equivalently or better than $f(\theta | X_L^*)$.

Based on how the uncertainty is obtained, we categorize AL methods into **data uncertainty-based methods** and **model uncertainty-based methods**. Data uncertainty-based methods attempt to get a sample with the greatest uncertainty from a batched dataset, while model uncertainty-based methods tend to sample the samples that cause the greatest uncertainty of the deep learning model’s perfor-

mance. A brief summary of surveyed AL papers is presented in Tab. 4.

2.5 Annotation-Efficient Learning

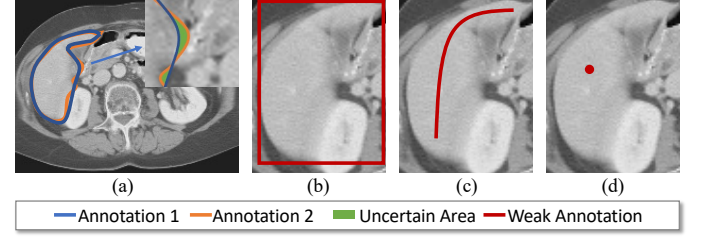


Fig. 7. Annotation types. (a) Pixel-wise annotation from two independent annotator; (b) Bounding box annotation; (c) Scribble annotation; (d) Point annotation.

Annotation-efficient learning is a technique that utilizes deep learning methods with partially labeled data for dense predictions to improve labeling efficiency. The intuitive approach to increase annotation efficiency is to provide markings other than fully dense annotations. While there may be overlapping techniques with the aforementioned categories, annotation-efficient learning methods specifically focus on leveraging the specific characteristics of the different forms of annotation to enhance the annotation efficiency and hence minimize the granularity difference between the annotation and the prediction. Fig. 7 shows different forms of annotation, and we will separately review the annotation-efficient learning methods that address the “not exact label” through a coarse-to-fine way. Specifically, we will discuss the techniques related to **Tag**, **Point**, **Scribble**, and **Box** annotations. Tab. 5 provides an overview of representative publications in this category.

3 SEMI-SUPERVISED LEARNING IN MIA

3.1 Proxy-labeling Methods

Proxy-labeling methods provide proxy labels for unlabeled data samples in X_U . They include those data samples with high-confidence proxy labels in the training dataset, training in an iterative manner. Proxy-labeling methods can be mainly categorized into two sub-categories: *Self-training methods* and *multi-view learning methods*.

3.1.1 Self-training Methods

Self-training methods aim to learn a prediction function f_θ with parameters θ by using a fraction of labeled data samples $x \in X_L$. After that, the trained prediction function f_θ is utilized to provide proxy labels of unlabeled data samples $x \in X_U$. Normally, a threshold τ is manually set and the sample-label pair $(x, \text{argmax}_f f_\theta(x))$ will be added to the labeled dataset X_L if the highest prediction probability in the output of f_θ outweighs τ . The updated labeled dataset will be consequently used to train the prediction function f_θ , and this process is conducted iteratively until f_θ cannot make predictions with enough confidence.

Entropy minimization [32] is a method that regularizes the model based on the low-density assumption, encouraging the model to generate low-entropy prediction for the

TABLE 1
Overview of Semi-supervised Learning-based Studies in Medical Image Analysis

	Reference _{Year}	Organ	Semi-SL Algorithm Design	Dataset	Result
Classification	Madani <i>et al.</i> [6] ₂₀₁₈	Lung	Semi-supervised GAN	NIH PLCO; NIH Chest X-Ray	Acc (Accuracy): 0.851
	Diaz-Pinto <i>et al.</i> [7] ₂₀₁₉	Retina	Semi-supervised DCGAN	ORIGA-light; DRISHTI-GS; RIM-ONE; HRF; DRD; sjchoi86-HRF; ACRIMA; DRIVE; Messidor	AUC: 0.9017
	Shi <i>et al.</i> [8] ₂₀₂₀	Lung; Breast	Graph Temporal Ensembling	TCGA-Lung; TCGA-Breast	TCGA-Lung: F1: 0.893; TCGA-Breast: F1: 0.930
	Yu <i>et al.</i> [9] ₂₀₂₁	Colon	Mean Teacher	Private Dataset: 13,111 Images	Patch-level AUC: 0.980; Patient-level AUC: 0.974
	Wang <i>et al.</i> [10] ₂₀₂₁	Breast; Retina	Virtual Adversarial Training + Self-training	RetinaIOCT; Private Dataset: 39,904 Images	Acc: 0.9513; Macro-R (Macro-Recall): 0.9330
	Liu <i>et al.</i> [11] ₂₀₂₂	Lung; Skin	Anti-curriculum Self-training	ChestX-ray14; ISIC 2018	ChestX-ray14: AUC: 0.8177; ISIC: AUC: 0.9436
	Zhang <i>et al.</i> [12] ₂₀₂₂	Spinal cord	Consistency Regularization + Pseudo-labeling + Active Learning	Private Dataset: 7,295 Images;	Acc: 0.9582; Macro-P (Macro-Precision): 0.8609
	Bai <i>et al.</i> [13] ₂₀₁₇	Heart	CRF-based Self-training	Private Dataset: 8050 Images	DSC: 0.920
	Li <i>et al.</i> [14] ₂₀₁₈	Skin	PI-model	ISIC 2017	DSC: 0.874; Acc: 0.943
	Nie <i>et al.</i> [15] ₂₀₁₈	Prostate	Self-training	Private Dataset: 70 Images	DSC: 0.970; ASD (Average Surface Distance): 1.401
Segmentation	Yu <i>et al.</i> [16] ₂₀₁₉	Heart	Uncertainty-aware Mean Teacher	ASG	DSC: 0.8888; 95HD: 7.32; JI: 0.8021
	Zhou <i>et al.</i> [17] ₂₀₁₉	Multi-Organ	Multi-planar Co-training	Private Dataset: 310 Volumes	DSC: 0.7794
	Li <i>et al.</i> [18] ₂₀₂₀	Liver; Retina; Skin	Transformation-consistent Mean Teacher	ISIC 2017; REFUGE; LiTS	ISIC: DSC: 0.8344; REFUGE: DSC: 0.9543; LiTS: DSC: 0.9427
	Liu <i>et al.</i> [19] ₂₀₂₀	Skin; Lung	Mean Teacher + Sample Relation Consistency	ISIC 2018; ChestX-ray14	ISIC: AUC: 0.9358; ChestX-ray8: AUC: 0.7923
	Li <i>et al.</i> [20] ₂₀₂₀	Heart	Shape-aware Consistency Regularization	ASG	DSC: 0.8954; JI (Jaccard Index): 0.8124
	Fan <i>et al.</i> [21] ₂₀₂₀	Lung	Attention Self-training	IS-COVID	DSC: 0.739
	Chaitanya <i>et al.</i> [22] ₂₀₂₁	Heart; Prostate; Pancreas	Semi-supervised GAN + Deformation and Additive Intensity Field	ACDC; DECATHLON	ACDC: DSC (Dice coefficient): 0.834; DECATHLON: DSC: 0.529
	Luo <i>et al.</i> [23] ₂₀₂₁	Nasopharynx	Uncertainty Rectified Pyramid Consistency	Private Dataset: 258 MR Images	DSC: 0.8076
	Luo <i>et al.</i> [24] ₂₀₂₁	Heart;	Dual-task Consistency	ASG; NIH PCT	ASG: DSC: 0.8942; NIH PCT: DSC: 0.7827;
	Li <i>et al.</i> [25] ₂₀₂₁	Lung; Skin; Liver	StyleGAN2	ChestX-ray14; JSRT Database; ISIC 2018; LiTS; CHAOS	DSC: Lung: 0.9668; ISIC: 0.8329; LiTS: 0.9169
	You <i>et al.</i> [26] ₂₀₂₂	Heart; Pancreas	Mean Teacher + Contrastive Learning	ASG; NIH PCT	ASG: DSC: 0.9085; NIH PCT: DSC: 0.7539
	Wang <i>et al.</i> [27] ₂₀₂₂	Heart; Prostate	Mean Teacher + Contrastive Learning	ACDC; ProMRI	ACDC: DSC: 0.914; ProMRI: DSC: 0.704
	Wu <i>et al.</i> [28] ₂₀₂₂	Heart; Pancreas	Uncertainty-based Mutual Consistency	ASG; NIH PCT; ACDC	DSC: ASG: 0.9107; NIH PCT: 0.8059; ACDC: 0.8851
	Luo <i>et al.</i> [29] ₂₀₂₂	Heart	Co-training Variant	ACDC	DSC: 0.864
Detection	Wang <i>et al.</i> [30] ₂₀₂₀	Lung	MixMatch + Focal Loss	LUNA; NLST	LUNA: CPM: 0.872
	Zhou <i>et al.</i> [31] ₂₀₂₁	Multi-Organ	Teacher-student Model + Adaptive Consistency Loss	DSB; DeepLesion	DSB: mAP: 0.694; DeepLesion: Sens (Sensitivity): 0.779

unlabeled data. **Pseudo-label** [33] is a simple yet effective self-training mechanism that inherits the concept of entropy minimization in the prediction space. The labeled samples are trained in a supervised way, and unlabeled data are assigned with the most confident predictions. In MIA, pseudo-label is employed as an auxiliary component to enhance model performance [12], [21]. In fact, proxy labels are normally noisy and may not reflect the ground truth. Therefore, various quality measurements such as uncertainty-aware confidence evaluation [34], conditional random field-based proxy label refinement [13], and adversarial training-based method [35] have been developed to ensure that reliable supervision signals can be generated based on pseudo labels. Pseudo-label has also been used in MIA to refine a given annotation with the assistance of unlabeled data. Qu *et al.* [36] introduce pseudo-label into nuclei segmentation and design an iterative learning algorithm to refine the background of weakly labeled images where only nuclei are annotated, leaving large areas ignored. Similar ideas can also be seen in [15].

3.1.2 Multi-view learning methods

Multi-view learning methods assume that each sample has two or multiple complementary views and features of the same sample extracted with different views are supposed to be consistent. Therefore, the key idea of multi-view learning methods is to train the model with multiple views of the sample or train multiple learners and minimize the disagreement between them, thus learning the underlying features of the data from multiple aspects. **Co-training** is a method that falls into this category. It assumes that data sample x can be represented by two views, $\mathbf{v}_1(x)$ and $\mathbf{v}_2(x)$, and each of them is capable of solely training a good learner, respectively. Consequently, the two learners are set to make

predictions of each view's unlabeled data, and iteratively choose the candidates with the highest confidence for the other model [37]. Another variation of multi-view learning methods is Tri-training [38], which is proposed to tackle the lack of multiple-view data and mistaken labels of unlabeled data produced by self-training methods. Tri-training aims to learn three models from three different training sets obtained with bootstrap sampling. Recently a deep learning version of Tri-training, i.e. Tri-Net, has been proposed in [39].

Co-training, or deep co-training, is dominant in multi-view learning in MIA, with a steady flow of publications [17], [40], [41], [42], [43]. To conduct whole brain segmentation, Zhao *et al.* [40] implements co-training by obtaining different views of data with data augmentation. A similar idea can be seen for 3D medical image segmentation in [41] and [17]. These two works both utilize co-training by learning individual models from different views of 3D volumes such as the sagittal, coronal, and axial planes. Further works have been proposed to refine co-training. To produce reliable and confident predictions, Wang *et al.* [42] develop a self-paced learning strategy for co-training, forcing the network to start with the easier-to-segment regions and transition to the difficult areas gradually. Meanwhile, to avoid the errors of different model components accumulating and causing deviation, Fang, and Li [43] develop an end-to-end model called difference minimization network for medical image segmentation by conducting co-training with an encoder shared by two decoders.

3.2 Generative Methods

Generative Semi-SL assumes that the entire dataset X is generated from the same latent distribution. In this sense, the key point of generative methods is to learn and simulate

the latent distribution with the help of unlabeled data. Then the model with a well-learned latent distribution aims to improve performance by combining supervised information.

Generative adversarial network (GAN) is a widely used model leveraging both labeled and unlabeled data. The standard GAN is composed of a generator \mathcal{G} and a discriminator \mathcal{D} , trying to satisfy the Nash equilibrium [44]. Typically, a generator is trained to generate plausible images and a discriminator is trained to distinguish the generated image and the real one. The unlabeled data can be involved during the adversarial training process, in which the discriminator aims to distinguish the generated fake input and real unlabeled data. By solving the two-player minimax game, GAN can learn the underlying distribution with the help of unlabeled data. The MIA field has seen publications with respect to generative Semi-SL methods based on GAN [6], [7], [22], [35], [45], [46]. Chaitanya *et al.* [22] directly incorporate the unlabeled data during the adversarial training of GAN to train a better generator for boosting medical data augmentation, arguing that utilizing unlabeled samples allows more variations in shape and intensity so as to make the model robust and guide the optimization. A similar idea can be seen in Hou *et al.* [45]. While Zhou *et al.* [35] develop a generator network to predict the pseudo lesion masks for unlabeled data and utilize the discriminator to facilitate the quality of the generated lesion mask. Other researchers have designed quite a number of methods modifying the discriminator \mathcal{D} . Instead of only distinguishing real or fake images, Odena *et al.* [47] seeks to learn the category information by predicting K classes and an additional real or fake class. In this way, the unlabeled data can contribute to the model during the classification of the $K + 1$ categories. In the context of MIA, the architecture proposed in [47] has produced fruitful results in various fields, such as retinal image synthesis [7], [46], glaucoma assessment [7], chest X-ray classification [6], and so on [45].

Variational autoencoder (VAE) is also useful and prospective in utilizing unlabeled data. It is an autoencoder rooted in Bayesian inference theory [48]. A typical VAE encodes a data sample into a latent variable and decodes it into the reconstruction of input by maximizing the variational lower bound. Our review of related literature shows that VAEs in MIA scenarios are mostly utilized for learning the inherent feature similarity from a large unlabeled dataset, thus contributing to a well-constrained latent space which can consequently avoid the need for numerous labeled data for training [49], [50]. Sedai *et al.* [49] propose a dual-VAE framework to conduct semi-supervised segmentation of the optic cup in retinal fundus images, in which one VAE learns the data distribution with unlabeled data and transfers the prior knowledge to the other VAE which conducts segmentation with the labeled data. Instead of using a mean vector and a variance vector for the latent representation, Wang *et al.* [50] adapts the VAE architecture into 3D medical image segmentation by introducing a mean vector and a covariance matrix to involve the correlation of different slices of an input volume.

3.3 Consistency Regularization Methods

Based on the smoothness or manifold assumption, **Consistency regularization methods** follow the idea that the

perturbation of data points does not change the prediction of the model. Meanwhile, this process does not require label information, which has proved an effective constraint for learning the unlabeled data.

Π -model [51] is a simple yet effective implementation of the above idea. This method uses a shared encoder to obtain different views of the input sample through augmentation and force the classifier to produce the same prediction for different augmentations of x . Meanwhile, label information is included in the training process to improve the performance of the classifier. By designing a Π -model-based semi-supervised algorithm, Li *et al.* [14] set a new record for skin lesion segmentation with only 300 labeled images, surpassing the state-of-the-art which was fully-supervised and used a set of 2,000 labeled images. A similar idea can be seen in [52], where Bortsova *et al.* conducts semi-supervised chest X-ray segmentation by learning prediction consistency given a set of transformations. **Temporal ensembling** [53] was developed to improve the prediction stability of the Π -model by adding exponentially moving average module for updating prediction. A number of researchers have implemented this module to address MIA-related problems [8], [54], [55], [56]. To conduct accurate breast mass segmentation, Cao *et al.* [54] introduces uncertainty into the temporal ensembling model by using uncertainty maps as guidance for the neural network to ensure the reliability of generated predictions. Similarly, Luo *et al.* [56] propose an uncertainty-aware temporal ensembling to learn from external partially labeled data for chest X-ray screening. Instead of directly feeding the augmented version of sample x_i into neural networks, Gyawali *et al.* [55] employ a VAE model to firstly extract the disentangled latent space and use it as stochastic embedding for the model input, leading to improved temporal ensembling in chest X-ray classification. During the training process of temporal ensembling, the activation of each training sample is only updated once in one epoch. By implementing exponentially moving average on model parameters rather than network activations, **Mean teacher** [57] overcomes this disadvantage and has been applied in the MIA field as well [16], [18], [58]. [18] is a typical application of the mean teacher model in MIA, which utilizes this model to conduct transformation-consistent medical image segmentation. However, with no ground truth given for unlabeled training data, the output of the teacher model can be inaccurate and noisy. Yu *et al.* [16] incorporate an uncertainty map with the mean teacher model to ensure the reliability of targets generated by the teacher. Wang *et al.* [58] further improve uncertainty-aware methods for segmentation of the left atrium and kidney by proposing a double-uncertainty-weighted method, which extends segmentation uncertainty to feature-level uncertainty.

3.4 Hybrid Methods

A burgeoning Semi-SL research direction is to combine the aforementioned types of methods together and unify them into a holistic framework for better performance [10], [12], [30]. These are called hybrid methods in this survey. For example, Wang *et al.* [10] and Zhang *et al.* [12] combine consistency regularization with self-training to solve medical image classification problems. Besides, Mixup [59] has

been utilized frequently as an effective data augmentation strategy in hybrid methods. In [60], the authors implement Mixup on both input and latent space to create more sample-label pairs based on both labeled and unlabeled data to facilitate medical image classification. By leveraging Mixup and focal loss, Wang *et al.* [30] improve MixMatch [61], which is a combination of consistency regularization and pseudo-labeling, in the field of 3D medical image detection. By leveraging multiple Semi-SL methods, the model is able to learn the underlying invariant features and meanwhile empowered with a strong predictive capability.

3.5 Discussion

Various unlabeled data inclusion and regularization approaches lead to numerous Semi-SL methods. Many research efforts are devoted to generating pseudo labels for unlabeled data to enrich the training dataset, during which the measurement of pseudo labels' quality and confidence plays an essential role. In addition, other researchers aim to leverage the unlabeled data to learn the distribution of real data such as generative methods, or learn a model with robust prediction ability such as consistency regularization methods. An open problem is how to ensure the model performs well when input unlabeled data are noisy, *i.e.*, to learn task-specific and perturbation-invariant features. Besides, a burgeoning research direction is to combine various Semi-SL methods to maximize the exploitation and utilization of unlabeled data and boost MIA tasks.

4 SELF-SUPERVISED LEARNING IN MIA

4.1 Reconstruction-Based Methods

Reconstruction-based methods in Self-SL focuses on exploring the inherent structures of data without the help of human annotations. These methods are conducted on several tasks including super-resolution [79], [84], inpainting [90], colorization [75], and the emerging MIA-specific application, multi-modal reconstruction [68], [81].

A straightforward way to establish the reconstruction task is proposed by Li *et al.* [80], who adopt an auto-encoder network to encode and reconstruct normal-dose computed tomography (CT) images for learning the latent features by minimizing the mean squared error (MSE) loss. After self-supervised pre-training, the encoder is utilized for feature extraction, and a supervised loss is computed with the encoded latent features. However, the self-supervised pre-training based on the minimization of reconstruction loss might neglect the basic structure of the input image and capture the color space distribution instead [75]. More proxy tasks have been motivated to solve this challenge.

The super-resolution reconstruction task is to generate fine-grained and realistic high-resolution images by utilizing low-resolution input images. In this proxy task, the targeted model can learn the underlying semantic features and structures of data. Zhao *et al.* [79] propose an anti-aliasing algorithm based on super-resolution reconstruction to reduce aliasing and restore the quality of magnetic resonance images (MRIs). In the meantime, super-resolution reconstruction is also an appropriate proxy task for gigapixel histopathology whole-slide images (WSIs) because

low-resolution WSIs are rather easy to store and process. From this application, Li *et al.* [84] conduct single image super-resolution for WSIs using GAN.

The image colorization task is to predict the RGB version of the gray-scale images. During this process, the network is trained to capture the contour and shape of different tissues in the sample and fill them with respective colors. Abbet *et al.* [75] introduce the image colorization task into survival analysis of colorectal cancer. They train a convolutional auto-encoder to convert the original input image into a two-channel image, namely, hematoxylin and eosin. Then, MSE loss is applied to measure the difference between the original input image and its converted counterpart.

The image inpainting task aims to predict and fill in missing parts based on the remaining regions of the input image. This proxy task allows the model to recognize the common features of identical objects, such as color and structure, and thus to predict the missing parts consistently with the rest of the image. Zhao *et al.* [90] propose a restoration module based on Self-SL to facilitate the anomaly detection of optical coherence tomography (OCT) and chest X-ray. It demonstrates that the restoration of missing regions facilitates the model's learning of the anatomic information.

In recent years, the multi-modal reconstruction task has emerged [68], [81]. In this task, the model uses the aligned multi-modal images of a patient to reconstruct an image in one modality by taking another modality as the input. Hervella *et al.* [68] propose this proxy task to enrich the model with joint representations of different modalities, arguing that each modality offers a complementary aspect of the object. Therefore, they take retinography and fluorescein angiography into consideration to facilitate retinal image understanding. Meanwhile, Cao *et al.* [81] develop a self-supervised collaborative learning algorithm, aiming at learning modality-invariant features for medical image synthesis by generating the missing modality with auto-encoder and GAN.

4.2 Context-Based Methods

Context-based methods utilize the inherent context information of the input image. Recent years have witnessed attempts to design novel predictive tasks for specific MIA tasks by training the network for prediction of the output class or localization of objects with the original image as the supervision signal [69], [70], [76]. Bai *et al.* [70] propose a proxy task to predict the anatomical positions from cardiac chamber view planes by applying an encoder-decoder structure. This proxy task properly employs the chamber view plane information, which is available from cardiac MR scans easily. Meanwhile, Srinidhi *et al.* [76] propose an MIA-specific proxy task, Resolution Sequence Prediction, which utilizes the multi-resolution information contained in the pyramid structure of WSIs. A neural network is employed to predict the order of multi-resolution image patches out of all possible sequences that can be generated from these patches. In this way, both contextual structure and local details can be captured by the network at lower and higher magnifications, respectively.

Other efforts have been made to explore the spatial context structure of input data, such as the order of different

TABLE 2
Overview of Self-supervised Learning-based Studies in Medical Image Analysis

	Reference ^{year}	Organ	Proxy Task Design	Dataset	Result
Classification	Li <i>et al.</i> [62] ₂₀₂₀	Retina	Multi-modal Contrastive Learning	ADAM; PALM	ADAM: AUC: 0.7458; PALM: AUC: 0.9855;
	Koohbanani <i>et al.</i> [63] ₂₀₂₁	Breast; Cervix; Colon	Magnification Prediction; Solving Magnification Puzzle; Hematoxylin Channel Prediction	CAMELYON 2016; KATHER; Private Dataset: 217 Images	CAMELYON 2016: AUC: 0.937; KATHER: AUC: 0.951; Private Dataset: AUC: 0.974
	Azizi <i>et al.</i> [64] ₂₀₂₁	Skin; Lung	Multi-Instance Contrastive Learning	Private Dermatology Dataset; CheXpert	Private: Top-1 Acc: 0.7002; CheXpert: AUC: 0.7729
	Tiu <i>et al.</i> [65] ₂₀₂₂	Lung	Contrastive Learning	CheXpert	AUC: 0.889
	Chen <i>et al.</i> [66] ₂₀₂₂	Breast; Lung; Kidney	Contrastive Learning	TCGA-BRCA; TCGA-NSCLS; TCGA-RCC	AUC: TCGA-Breast: 0.874; TCGA-NSCLS: 0.952; TCGA-RCC: 0.980
Segmentation	Mahapatra <i>et al.</i> [67] ₂₀₂₂	Lymph; Lung; Retina; Prostate	Contrastive Learning Variant	CAMELYON 2017; DRD; GGC ChestX-ray14; CheXpert;	Acc: CAMELYON 2017: 0.929; DRD: 0.951; GGC: 0.916; ChestX-ray14: Acc: 0.861; ChestXpert: Acc: 0.913
	Hervella <i>et al.</i> [68] ₂₀₁₈	Retina	Multi-modal Reconstruction	Isfahan MISP	AUC: 0.8183
	Spitzer <i>et al.</i> [69] ₂₀₁₈	Brain	Patch Distance Prediction	BigBrain	DSC: 0.80
	Bai <i>et al.</i> [70] ₂₀₁₉	Heart	Anatomical Position Prediction	Private Dataset: 3825 Subjects	DSC: 0.934
	Sahasrabudhe <i>et al.</i> [71] ₂₀₂₀	Multi-Organ	WSI Patch Magnification Identification	MoNuSeg	AJL: 0.5354; AHD (Average Hausdorff Distance): 7.7502
Regression	Tao <i>et al.</i> [72] ₂₀₂₀	Pancreas	Rubik's Cube Recovery	NIH PCT; MRBrainS18	NIH PCT: DSC: 0.8408; MRBrainS18: DSC: 0.7756
	Lu <i>et al.</i> [73] ₂₀₂₁	Brain	Fiber Streamlines Density Map Prediction; Registration-based Segmentation Imitation	dHCP	DSC: 0.822;
	Tang <i>et al.</i> [74] ₂₀₂₂	Abdomen; Liver; Prostate	Contrastive Learning; Masked Volume Inpainting; 3D Rotation Prediction	DECATHLON; BTCV	DECATHLON: DSC: 78.68; BTCV: DSC: 0.918
	Abbet <i>et al.</i> [75] ₂₀₂₀	Gland	Image Colorization	Private Dataset: 660 Images	Brier Score: 0.2725; C-Index: 0.6943
	Srinidhi <i>et al.</i> [76] ₂₀₂₀	Breast; Colon	WSI Patch Resolution Sequence Prediction	BreastPathQ; CAMELYON 2016; KATHER	BreastPathQ: ICC Coefficient: 0.907; CAMELYON 2016: AUC: 0.882; KATHER: Acc: 0.986; F1: 0.934
Others	Zhuang <i>et al.</i> [77] _{2019CS}	Brain	Rubik's Cube Recovery	BraTS 2018; Private Dataset: 1,486 Images	BraTS 2018: mIoU: 0.773; Private: Acc: 0.838
	Chen <i>et al.</i> [78] _{2019CDS}	Multi-Organ	Disturbed Image Context Restoration	Private Fetus Dataset: 2,694 Images; Private Multi-organ Dataset: 150 Images; BraTS 2017	Private Fetus Dataset: F1: 0.8942; Private Multi-organ Dataset: Mean Distance: 2.90 BraTS 2017: DSC: 0.8557
	Zhao <i>et al.</i> [79] _{2020SR}	Brain	Super-resolution Reconstruction	Private Dataset: 47 Images	S3 Sharpness: 0.5482
	Li <i>et al.</i> [80] _{2020DN}	Abdomen	CT Reconstruction	LDCTGC	PSNR: 22.1758; SSIM: 0.7800
	Cao <i>et al.</i> [81] _{2020IT}	Brain	Missing Modality Synthesis	BraTS 2015; ADNI	ADNI: IS (Inception Score): 2.15; FID: 64.29
	Haghighi <i>et al.</i> [82] _{2020CS}	Lung	Self-Discovery + Self-Classification + Self-Restoration	LUNA; LITS; CAD-PE; BraTS 2018; ChestX-ray14; LIDC-IDRI; SIIM-ACR	Classification: LUNA: AUC: 0.9847; Segmentation: IoU: LITS: 0.8560; BraTS 2018: 0.6882
	Taleb <i>et al.</i> [83] _{2020DS}	Brain; Retina; Pancreas	3D Contrastive Predictive Coding; 3D Jigsaw Puzzles; 3D Rotation Prediction; 3D Exemplar Networks Relative 3D Patch Location;	BraTS 2018; DECATHLON; DRD	BraTS 2018: DSC: 0.9080; DECATHLON: DSC \approx 0.635; DRD: DSC \approx 0.80
	Li <i>et al.</i> [84] _{2021SR}	Breast; Pancreas; Kidney	Super-resolution Reconstruction; Color Normalization	WTS; Private Dataset: 533 Images	PSNR: 28.32; SSIM: 0.8304
	Wang <i>et al.</i> [85] _{2021CS}	Multi-Organ	Contrastive Learning	TCGA; KATHER; MHIST PAIP; PatchCAMELYON	MHIST: F1: 0.8993; KATHER: F1: 0.9582; PatchCAMELYON: F1: 0.8983; AUC: 0.9779
	Zhou <i>et al.</i> [86] _{2021CS}	Lung; Brain; Liver	Contrastive Learning + Image Reconstruction	ChestX-ray14; CheXpert; LUNA BraTS 2018; LITS;	AUC: Chest: 0.831; LUNA: 0.922; DSC: LITS: 0.937; BraTS 2018: 0.85
	Yan <i>et al.</i> [87] _{2022RE}	Multi-Organ	Global and Local Contrastive Learning	DeepLesion; NIH LN; Private Dataset: 94 Patients	Mean Radial Error: 4.3; Maximum Radial Error: 16.4
	Cai <i>et al.</i> [88] _{2022CD}	Lung; Brain; Retina	Dual-Distribution Reconstruction	RSNA-Lung; LAG; VinDr-CXR; Brain Tumor MRI; Private Lung Dataset: 5,000 Images	AUC: RSNA-Lung: 0.913; Brain Tumor MRI: 0.972; VinDr-CXR: 0.859; LAG: 0.931; Private Lung Dataset: 0.710;
	Haghighi <i>et al.</i> [89] _{2022CS}	Lung	Contrastive Learning + Reconstruction + Adversarial Learning	ChestX-ray14; CheXpert; Montgomery	AUC: ChestX-ray14: 0.8112; CheXpert: 0.8759; Montgomery: DSC: 0.9824

¹ For the sake of brevity, we denote references that contain more than one task in the following abbreviations: C: Classification, S: Segmentation, D: Detection, SR: Super-resolution, DN: Denoising, IT: Image Translation, RE: Registration.

patches constituting an image, or the relative position of several patches in the same image, which can provide useful semantic features for the network. Chen *et al.* [78] focus on the proxy task, dubbed context restoration, of randomly switching the position of two patches in a given image iteratively and restoring the original image. During this process, semantic features can be learned in a straightforward way. Instead of concentrating on the inherent intensity distribution of an image, Li *et al.* [91] aims to improve the performance of a network with rotation angle prediction as the proxy task. The input retinal images are first augmented, generating several views, and then randomly rotated. The model is encouraged to predict the rotation angle and cluster the representations with similar features. More advanced proxy tasks such as Jigsaw Puzzles [92] and Rubik's Cube [93] are also attracting an increasing number of researchers. Taleb *et al.* [94] improve the Jigsaw Puzzle task with multi-modal data. Concretely, an input image is constituted of out-of-order patches of different modalities and the model is expected to restore the original image. Rubik's Cube is a task set for 3-dimensional data. Zhuang *et al.* [77] and Tao *et al.* [72] introduce Rubik's Cube into the MIA area, and significantly boost the performance of a deep learning

model on 3D data. In this method, the 3D volume will first be cut into a grid of cubes and a random rotation operation will be conducted on these cubes. The aim of this proxy task is to recover the original volume.

However, for histopathology images, common proxy tasks such as prediction of the rotation or relative position of objects may only provide minor improvements to the model in histopathology due to the lack of a sense of global orientation in WSIs [63], [95]. Therefore, Koohbanani *et al.* [63] propose proxy tasks targeted at histopathology, namely, magnification prediction, solving magnification puzzle, and hematoxylin channel prediction. In this way, their model can significantly integrate and learn the contextual, multi-resolution, and semantic features inside the WSIs.

4.3 Contrastive-Based Methods

Contrastive-based methods are based on the idea that the learned representations of different views of the same image should be similar and those of different images should be clearly distinguishable. Intriguingly, the ideas behind several high-performance algorithms such as SimCLR [96] and BYOL [97] have been incorporated into the MIA field [64], [85]. Multi-Instance Contrastive Learning

(MICLe), proposed by Azizi *et al.* [64], is a refinement and improvement of SimCLR. Instead of using one input to generate augmented views for contrastive learning, they propose to minimize the disagreement of several views from multiple input images of the same patient, creating more positive pairs. Meanwhile, Wang *et al.* [85] adopt the BYOL architecture to facilitate histopathology image classification. A contribution of their work was to collect the currently largest WSI dataset for Self-SL pre-training. It includes 2.7 million patches cropped from 32,529 WSIs covering over 25 anatomic sites and 32 classes of cancer subtypes. Similarly, Ghesu *et al.* [98] develop a contrastive learning and online clustering algorithm based on over 100 million radiography, CT, MRI, and ultrasound images. By leveraging this large unlabeled dataset for pre-training, the performance and convergence rate of the proposed model show a significant improvement over the state-of-the-art.

Further researchers take into account the global and local contrast for a better representation of learning. Their methods usually minimize the InfoNCE loss [99] to capture the global and local level information. In [87], Yan *et al.* implements the InfoNCE by encoding each pixel of the input image. Their goal is to generate embeddings that can precisely describe the anatomical location of that pixel. To achieve this, they developed a pixel-level contrastive learning framework to generate embeddings at both the global and local levels.

4.4 Hybrid Methods

Researchers have made efforts to combine some or all of the different types of Self-SL methods into a universal framework to learn latent representations from multiple perspectives, such as semantic features and structure information inside unlabeled data [74], [82], [86], [100]. For instance, Tang *et al.* [74] combine masked volume inpainting, contrastive coding, and image rotation tasks into a Swin Transformer encoder architecture for medical image segmentation.

4.5 Discussion

Self-SL methods aim to learn and obtain a model with prior knowledge by manipulating and exploiting unlabeled data. The key to the superior performance of Self-SL models is the design of proxy tasks. Numerous existing Self-SL methods directly adopt proxy tasks prevailing in natural image processing into the MIA field. However, the unique properties of medical images, such as CT, WSI, and MRI, should be exclusively considered and injected into the design process of proxy tasks. Further, proxy task design based on the combination of different medical image modalities is a prospective research direction, during which the model can capture disentangled features of each modality, leading to a robust pre-trained network. For example, large vision-language pre-trained models [101], [102] are emerging in chest X-ray and obtaining ever-increasing research interests.

5 MULTI-INSTANCE LEARNING IN MIA

5.1 Local Detection

Since we define **local detection** as detecting or localizing all the particular disease patterns of an input image, papers

with the purpose of segmentation or localization can be classified into this category. Most researchers design their local detection model to infer every patch label and thereby obtain both the local annotations and the global labels. Thus, the **local detection** methods often include **global detection** methods since inferring image-level labels after obtaining the local annotations.

Schwab *et al.* [130], apply the basic MIL algorithm to conduct the localization and classification of chest X-rays. They input every patch of the original sample into a CNN, and the model outputs a score for the patch representing its probability of containing a critical finding. Once the patch-level classifier is trained, the most straightforward way to perform slide-level classification is to integrate the patch-level predictions with max-pooling or average-pooling. The design for the pooling function plays an important role in the performance improvement of the MIL algorithm. For instance, in [105], the authors design a more general MIL aggregation method by utilizing a quantile function as the pooling function. By doing so, a more thorough description of the heterogeneity of each sample can be provided, enhancing the quality of global classification. Other studies [104], [108] propose learning-based aggregation operators to provide insight into the contribution of each instance to the bag. Among them, several are based on the attention-based MIL developed by Ilse *et al.* in [104]. By introducing the attention mechanism into MIL, their model can better capture the key features of regions of interest with interpretation. For the pancreatic ductal adenocarcinoma (PDAC) prediction problem, Wang *et al.* [131] design an inductive attention guidance network for both classification and segmentation. The attention mechanism works as a connection between the global classifier and local (instance) segmenter by guiding the location of PDAC regions.

Other intriguing improvements in **local detection** are springing up as well. Researchers have tried many different ways to facilitate instance prediction [103], [127], [128], [129]. Dov *et al.* [129] demonstrate that the general MIL methods perform poorly on cytopathology data for two reasons: instances that contain key information are located sparsely in a gigapixel pathology image, and the informative instances have various characteristics of abnormality. Thus, they propose a MIL structure involving maximum likelihood estimation to predict multiple labels, i.e., bag-level labels and diagnostic scores; instance-level labels and informativeness, simultaneously. Similarly, when studying the classification of the retinal nerve fiber layer (RNFL), Manivannan *et al.* [103] have observed that regions that contain the RNFL generally have strong intra-class variation, making them difficult to distinguish from other regions. Therefore, they map the instances into a discriminative subspace to increase the discrepancy for disentangled instance feature learning. Jia *et al.* [127] incorporate the multi-scale image feature into the learning process to obtain more latent information on histopathology images. Finally, to address the problem that only image-level labels are provided in MIL, Xu *et al.* [128] design an automatic instance-level label generation method. Their work has led to an interesting MIL algorithm design direction and may shed light on how to improve the performance of **local detection** algorithms.

Other studies on problems such as phenotype catego-

TABLE 3
Overview of Multi-instance Learning-based Studies in Medical Image Analysis

	Reference ^{Year}	Organ	MIL Algorithm Design	Dataset	Result
Classification	Manivannan <i>et al.</i> [103] ₂₀₁₇	Retina; Breast	Discriminative Subspace Transformation + Margin-based Loss	Messidor; TMA-UCSB; DR Dataset; Private Dataset: 884 Images	Messidor: Acc: 0.728; TMA-UCSB: AUC: 0.967; DR Dataset: Acc: 0.8793; Private: Kappa: 0.7212
	Ilse <i>et al.</i> [104] ₂₀₁₇	Breast; Colon	Attention-based MIL	TMA-UCSB; CRCHistoPhenotypes	TMA-UCSB: Acc: 0.755; CRCHistoPhenotypes: Acc: 0.898
	Couture <i>et al.</i> [105] ₂₀₁₈	Breast	Quantile Function-based MIL	CBCS3	Acc: 0.952
	Liu <i>et al.</i> [106] ₂₀₁₈	Brain	Landmark-based MIL	ADNI; MIRIAD	ADNI: AUC: 0.9586; MIRIAD: AUC: 0.9716
	Campanella <i>et al.</i> [107] ₂₀₁₉	Prostate; Skin; Lymph	MIL + RNN	Private Dataset: 44,732 Images	AUC: Prostate: 0.986; Skin: 0.986; Lymph: 0.965
	Wang <i>et al.</i> [108] ₂₀₁₉	Breast	Instance Features Recalibration	Private Dataset: 608 Images	Acc: 0.865
	Yao <i>et al.</i> [109] ₂₀₁₉	Lung; Brain	Multiple Instance FCN	NLST; TCGA	NLST: C-Index: 0.678; TCGA: C-Index: 0.657
	Wang <i>et al.</i> [110] ₂₀₂₀	Retina	Uncertainty-aware MIL + RNN Aggregation	Duke-AMD; Private Dataset: 4,644 Volumes	Acc: Duke-AMD: 0.979; Private Dataset: 0.951
	Zhao <i>et al.</i> [111] ₂₀₂₀	Colon	VAE-GAN Feature Extraction + GNN Bag-level Representation Learning	TCGA-COAD	Acc: 0.6761; F1: 0.6667; AUC: 0.7102
	Chikontwe <i>et al.</i> [112] ₂₀₂₀	Colon	Jointly Learning of Instance- and Bag-level Feature	Private Dataset: 366 Images	F1: 0.9236; P (Precision): 0.9254; R (Recall): 0.9231; Acc: 0.9231
	Raju <i>et al.</i> [113] ₂₀₂₀	Colon	Graph Attention MIL	MCO	Acc: 0.811; F1: 0.798
	Han <i>et al.</i> [114] ₂₀₂₀	Lung	Automatic Instance Generation	Private Dataset: 460 Examples	AUC: 0.99
	Yao <i>et al.</i> [115] ₂₀₂₀	Lung; Colon	Siamese Multi-instance FCN + Attention MIL	NLST; MCO	NLST: AUC: 0.7143; MCO: AUC: 0.644
	Hashimoto <i>et al.</i> [116] ₂₀₂₀	Lymph	Domain Adversarial + Multi-scale MIL	Private Dataset: 196 Images	Acc: 0.871
	Shao <i>et al.</i> [117] ₂₀₂₁	Breast; Lung; Kidney	Transformer-based MIL	CAMELYON 2016; TCGA-NSCLC; TCGA-RCC	Acc: CAMELYON: 0.8837; TCGA-NSCLC: 0.8835; TCGA-RCC: 0.9466
	Li <i>et al.</i> [118] ₂₀₂₁	Breast; Lung	Dual-stream MIL + Contrastive Learning	CAMELYON 2016; TCGA Lung Cancer	CAMELYON 2016: AUC: 0.9165; TCGA: AUC: 0.9815
	Li <i>et al.</i> [119] ₂₀₂₁	Lung	Virtual Bags + Self-SL Location Prediction	Private Dataset: 460 Examples	AUC: 0.981; Acc: 0.958; F1: 0.895; Sens: 0.936
	Lu <i>et al.</i> [120] ₂₀₂₁	Kidney; Lung; Lymph node	Attention-based MIL + Clustering	TCGA-RCC + Private Dataset: 135 WSIs; CPTAC-NSCLC + Private Dataset: 131 WSIs; CAMELYON 2016,17 + Private Dataset: 133 WSIs	Kidney: AUC: 0.972; Lung: AUC: 0.975; Lymph node: AUC: 0.940
	Wang <i>et al.</i> [121] ₂₀₂₂	Thyroid	Transformer-based MIL + Knowledge Distillation	Private Dataset: 595 Images	AUC: 0.9835; P: 0.9482; R: 0.9151; F1: 0.9297
	Zhang <i>et al.</i> [122] ₂₀₂₂	Breast; Lung	Double-Tier Feature Distillation MIL	CAMELYON 2016; TCGA-Lung	CAMELYON 2016: AUC: 0.946; TCGA-Lung: AUC: 0.961
	Schirris <i>et al.</i> [123] ₂₀₂₂	Breast; Colon	Heterogeneity-aware MIL + Contrastive Learning	TCGA-CRCR; TCGA-BC	TCGA-CRCR: AUC: 0.87; TCGA-BC: AUC: 0.81
	Su <i>et al.</i> [124] ₂₀₂₂	Breast; Kidney	Intelligent Sampling Method + Attention MIL	CAMELYON 2016; Private Dataset: 112 Images	CAMELYON 2016: AUC: 0.891; Private: AUC: 0.974
	Zhu <i>et al.</i> [125] ₂₀₂₂	Breast; Lung; Kidney	Reinforcement Learning + Contrastive Learning + MIL	CAMELYON 2016; TCGA-Lung; TCGA-Kidney	AUC: CAMELYON: 0.9452; TCGA-Lung: 0.9637; TCGA-Kidney: 0.9573
	Yang <i>et al.</i> [126] ₂₀₂₂	Colon; Muscle	Curriculum Learning + MIL	CRCHistoPhenotypes; Private Muscle Dataset: 266 Images	CRCHistoPhenotypes: AUC: 0.898; Private: AUC: 0.907
Segmentation	Jia <i>et al.</i> [127] ₂₀₁₇	Colon	Multi-scale MIL + Area Constraint Regularization	Private TMA/Colon Dataset: 60 Images/910 Images	F1: TMA: 0.622; Colon: 0.836
	Xu <i>et al.</i> [128] ₂₀₁₉	Breast	Instance-level and Pixel-level Label Generation	CAMELYON 2016	Image-level Acc: 0.929; Pixel-level IoU: 0.847
	Dov <i>et al.</i> [129] ₂₀₂₁	Thyroid	Maximum Likelihood Estimation-based MIL	Private Dataset: 908 Images	AUC: 0.87
Others	Schwab <i>et al.</i> [130] _{2020CD}	Lung	Jointly Classification and Localization	RSNA-Lung; MIMIC-CXR; Private Dataset: 1,003 Images	AUC: 0.93
	Wang <i>et al.</i> [131] _{2021CS}	Pancreas	Jointly Global-level Classification and Local-level Segmentation	Private Dataset: 800 Images	DSC: 0.6029; Sens: 0.9975

¹ For the sake of brevity, we denote references that contain more than one task in the following abbreviations: C: Classification, S: Segmentation, D: Detection.

rization [109], [115], [116] and multi-label classification [132] have also made promising progress with the MIL algorithm.

5.2 Global Detection

Global detection refers to methods that simply aim to find out whether or not target patterns exist. For example, for the COVID-19 screening problem, researchers [119] have designed MIL algorithms to classify an input sample as severe or not instead of locating every abnormal patch.

To facilitate the prediction of image-level labels (*e.g.* WSI-level label), researchers normally start from one of two aspects, namely instance- and bag-level. Most existing MIL algorithms [116], [120], [133], [134] are based on the basic assumption that instances of the same bag are independent and identically distributed. Consequently, the correlations among instances are neglected, which is not realistic. Recently several works have taken the correlation among instances or tissues into consideration [108], [113], [114], [117], [121]. In [117], Shao *et al.* introduce Vision Transformer (ViT) into MIL for gigapixel WSIs due to its great advantage in capturing the long-distance information and correlation among instances in a sequence. Meanwhile, to conduct precise lymph node metastasis prediction, Wang *et al.* [121] not only incorporate a pruned Transformer into MIL but also develop a knowledge distillation mechanism based on other similar datasets, such as a papillary thyroid carcinoma dataset, effectively avoiding the overfitting problem caused by the insufficient number of samples in the original dataset. Similarly, Raju *et al.* [113] design a graph

attention MIL algorithm for colorectal cancer staging, which utilizes different tissues as nodes to construct graphs for instance relation learning.

For bag-level improvement, recent years have witnessed two feasible approaches, namely, improved pooling methods and pseudo bags. On the one hand, in order to aggregate the instances with the most information, some researchers have developed novel aggregation methods in MIL algorithms instead of the traditional max pooling [112], [135]. For example, in [112], the authors design a pyramid feature aggregation method to directly obtain a bag-level feature vector. On the other hand, however, there is an inherent problem for MIA, especially for histopathology — the number of WSIs (bags) is usually small, while in contrast, one WSI has numerous patches, leading to an imbalance in the number of bags and instances. To address this problem, Zhang *et al.* [122] randomly split the instances of a bag into several smaller bags, called “pseudo bags”, with labels that are consistent with the original bag. A similar idea can also be seen in [119].

Other improvements in MIL algorithms are also worth mentioning [110], [124], [136]. In [124], an intelligent sampling method is developed to collect instances with high confidence. This method excludes patches shared among different classes and tends to select the patches that match with the bag-level label. In [136], the authors utilize the extreme value theory to measure the maximum feature deviations and consequently leverage them to recognize the positive instances, while in [110], Wang *et al.* introduce an uncertainty evaluation mechanism into MIL for the first

time, and train a robust classifier based on this mechanism to cope with OCT image classification problem.

5.3 Discussion

Multi-instance learning in MIA is mainly applied to whole slide image analysis, which can be described as “a needle in a haystack” problem, making bag-level decisions out of thousands of instances. MIL methods are developed to locate the discriminative patches as a basis for diagnosis. To achieve this goal, MIL research can be divided into several focuses. For the bag-instance correlation, a WSI is represented as a bag containing selected patches during training, which leads to the question of how the patches should be selected to make the bag representative of the WSI. Further, how to handle and leverage the imbalance of positive and negative samples could have a significant impact on model performance. For the instance-instance correlation, the proper modeling and utilization of instance relations can boost the performance of MIL algorithms and advance the interpretability of the model.

6 ACTIVE LEARNING IN MIA

6.1 Data Uncertainty-Based Methods

Developed from the conventional entropy uncertainty metrics³, Konyushkova *et al.* [141] defined geometric smoothness priors with boosted trees to classify the formed graph representation of electron microscopy images. Here, they flatten 3D images into supervoxels with the SLIC algorithm [147] to conduct graph representations. Yang *et al.* [140] use cosine similarity and a bootstrapping technique to evaluate the uncertainty and representativeness of the output feature with a DCAN [148]-like network. Zhou *et al.* [146] propose the concept of “active selection” policies, which is the highest confidence based on the entropy and diversity results from sampled data in the mean prediction results.

Aside from leveraging the conventional metrics, utilizing metrics from the deep learning model is another trend. Intuitively, Wu *et al.* [138] utilize network loss as well as the diversity condition as the uncertainty metric for sampling from a loss prediction network, and conduct the COVID-19 classification task from another classification network. Nath *et al.* [142] leverage marginal probabilities between the query images and the labeled ones, they build a mutual information metric as the diversity metric to serve as a regularizer. Moreover, they adopt Dice log-likelihood instead of its original entropy-based log-likelihood for Stein variational gradient descent optimizer [149] to solve the label imbalance problem. Zhao *et al.* [144] utilize Dice’s coefficient of the predicted mask calculated between the middle layer and the final layer of the model as the uncertainty metric for the image segmentation task. They use their DS-UNet with a denseCRF [150] refiner to annotate low uncertainty samples and oracle annotators for the others. Li *et al.* [139] use k-means clustering and curriculum classification (CC) based on the CurriculumNet [151] for uncertainty and representativeness estimation. Furthermore, they consider the condition under which noisy medical labels are present and accomplish their automatic exclusion using O2U-Net [152].

3. To aid the understanding of these metrics, a detailed description of the prior knowledge is provided in Appendix A.2.

6.2 Model Uncertainty-Based Methods

Bayesian neural networks have attracted increasing attention for their ability to represent and propagate the probability of the DL model. Gal *et al.* [137] employ Bayesian CNNs for skin cancer classification with Bayesian Active Learning by Disagreement (BALD) [153] Ozdemir *et al.* [143] form a Bayesian network and employ Monte Carlo dropout [154] to obtain the variance information as the model uncertainty. They also construct a representativeness metric produced by infoVAE [155] for the maximum likelihood sampling in the latent space. Mahapatra *et al.* [145] also uses a Bayesian neural network to sample the training data. Meanwhile, they use conditional GAN to generate realistic medical images for data augmentation.

6.3 Discussion

Whether from the data or from the model, uncertainty measurement is a critical task throughout the whole AL process. The current research directions regarding label-efficient AL methods in MIA focus primarily on the improvement of AL query strategies and the optimization of training methods. For the future, researchers could i) delve into hybrid AL query strategies together with diversity assessment, ii) concentrate on hybrid training schemes (*i.e.*, combined Semi-SL, Self-SL schemes) to yield an intermediate feature representation to further guide the training process, iii) mitigate the degradation of annotation quality when encountering noisy labels.

7 ANNOTATION-EFFICIENT LEARNING IN MIA

7.1 Tag Annotation

Tag annotation, which is a text/binary label for each image, is the most efficient form. Most of such are based on the concept of class activation mapping (CAM) [156]. Several works propose to use of CAM to generate object localization proposals or even to perform whole-object pixel-wise segmentation. For the **detection** task, Wang *et al.* [157] propose a two-branch network that jointly optimizes the classification and lesion detection tasks. In this approach, the CAM-based lesion detection network is supervised with only image-level annotations, and the two branches are mutually guided by the weight-sharing technique, where a weighting parameter is adopted to control the focus of learning from the classification task to the detection task. For lesion detection, Dubost *et al.* [158] propose a weakly-supervised regression network. The proposed method is validated on both 2D and 3D medical images. For the **segmentation** task, Li *et al.* [159] propose a breast tumor segmentation method with only image-level annotations based on CAM and deep-level set (CAM-DLS). It integrates domain-specific anatomical information from breast ultrasound to reduce the search space for breast tumor segmentation. Meanwhile, Chen *et al.* [160] proposes a causal CAM method for organ segmentation, which is based on the idea of causal inference with a category-causality chain and an anatomy-causality chain. In addition, several studies [161], [162] demonstrate that bridging the classification task and dense prediction task (*e.g.*, detection and segmentation) via CAM-based methods is beneficial for both tasks. Compared to natural

TABLE 4
Overview of Active Learning-based Studies in Medical Image Analysis

	Reference ^{Year}	Organ	Sampling Method	Dataset	Result
Classification	Gal <i>et al.</i> [137] ₂₀₁₇	Skin	BALD + KL-divergence	ISIC 2016	22% image input: AUC: 0.75
	Wu <i>et al.</i> [138] ₂₀₂₁	Lung	Loss Prediction Network	CC-CCII Dataset	42% Chest X-Ray input: Acc: 86.6%
	Li <i>et al.</i> [139] ₂₀₂₁	Prostate	CurriculumNet + O2U-Net	ISIC 2017; PANDA Dataset	60% input: QWK: 0.895
Segmentation	Yang <i>et al.</i> [140] ₂₀₁₇	Gland; Lymph	Cosine Similarity + Bootstrapping + FCN	GlaS 2015; Private Dataset: 80 US images	MICCAI 2015: 50% input: F1: 0.921; Private Dataset: 50% input: F1: 0.871
	Konyushkova <i>et al.</i> [141] ₂₀₁₉	Brain (Striatum; Hippocampus)	Geometric Priors + Boosted Trees	BraTS 2012; EFPL EM Dataset	MRI Data: 60% input: DSC≈0.76; EM Data: 40% input: DSC≈0.60
	Nath <i>et al.</i> [142] ₂₀₂₀	Brain	Entropy + SVGD Optimization	MSD 2018 Dataset	22.69% Hippocampus MRI input: DSC: 0.7241
	Ozdemir <i>et al.</i> [143] ₂₀₂₁	Shoulder	BNN + MMD Divergence	Private Dataset: 36 Volume of MRIs	48% MRI input: DSC≈0.85
	Zhao <i>et al.</i> [144] ₂₀₂₁	Hand; Skin	U-Net	RSNA-Bone; ISIC 2017	9 AL Iteration: DSC: 0.834
Others	Mahapatra <i>et al.</i> [145] _{2018CS}	Chest	Bayesian Neural Network + cGAN Data Augmentation	JSRT Database; ChestX-ray8	Classification: 35% input: AUC: 0.953; Segmentation: 35% input: DSC: 0.910
	Zhou <i>et al.</i> [146] _{2021CD}	Colon	Traditional Data Augmentation Entropy + Diversity	Private Dataset: 6 colonoscopy videos 38 polyp videos + 121 CTPA datasets	Classification: 4% input: AUC: 0.9204; Detection: 2.04% input: AUC: 0.9615

¹ For the sake of brevity, we denote references that contain more than one task in the following abbreviations: C: Classification, S: Segmentation, D: Detection.

images, medical images are usually from low contrast, limited texture, and varying acquisition protocols [163], which makes directly applying CAM-based methods less effective. Fortunately, incorporating the clinical priors (e.g., objects' size [164]) into the weakly supervised detection task is promising to improve the performance.

7.2 Point Annotation

Point annotation refers to the annotation of a single point of an object. Several studies [165], [166], [167] focus on using extreme points as the annotation to perform pixel-level segmentation. These methods typically consist of three steps: 1) extreme point selection; 2) initial segmentation with a random walk algorithm; 3) training of the segmentation model with the initial segmentation results. The last two steps can be iterated until the segmentation results are stable. However, these methods require the annotators to locate the boundary of the objects, which is still laborious in practice. In contrast, other studies [36], [168], [169], [170], [171], [172], [173], [174] use center point annotation to perform pixel-level segmentation for the task of cell/nuclear segmentation. These methods typically adopt the Voronoi [175] and cluster algorithms to perform coarse segmentation. Then different methods are used to refine the segmentation results, such as iterative optimization [36], [170], self-training [169], and co-training [173].

Compared with full annotation, point annotation can reduce the annotation time by around 80% [36]. However, some issues have not been addressed. First, existing methods typically derived pseudo labels from the point annotation, which are based on strong constraints or assumptions (e.g., Voronoi) from the data, restricting the generalization of these methods to other datasets [173]. Second, due to the lack of explicit boundary supervision, there is a non-negligible performance gap between the weakly supervised methods with points and the fully supervised methods.

7.3 Scribble Annotation

Scribble annotation, a set of scribbles drawn on an image by the annotators, has been recognized as a user-friendly alternative to bounding box annotation [186]. Compared with point annotation, it provides the rough shape and

size information of the objects, which is promising to improve the segmentation performance, especially for objects with complex shapes. Wang *et al.* [181] propose a self-training framework with differences in model predictions and user-provided scribbles. Can *et al.* [187] develop a random walk algorithm that incrementally performs region growing method around the scribble ground truth, while Lee *et al.* [188] introduce Scribble2Label, a method that integrates the supervision signals from both scribble annotations and pseudo labels with the exponential moving average. Furthermore, Dorent *et al.* [189] extend the Scribble-Pixel method to the domain adaptation scenario, where a new formulation of domain adaptation is proposed based on CRF and co-segmentation with the scribble annotation. In recent work, Zhang *et al.* [183] adopted mix augmentation and cycle consistency for the Scribble-Pixel method, demonstrating the improvement of both weakly and fully supervised segmentation methods.

7.4 Box Annotation

Box annotation encloses the segmented region within a rectangle, and various recent studies have focused on this Box-Pixel scenario. Rajchl *et al.* [184] employs a densely-connected random field (DCRF) with an iterative optimization method for MRI segmentation. Wang *et al.* [190], [191] adopt MIL and smooth maximum approximation based on the bounding box tightness prior [192], that is, an object instance should touch all four sides of its bounding box. Thus, a vertical or horizontal crossing line within a box yields a positive bag because it covers at least one foreground pixel. Studies [191] demonstrate that the Box-Pixel method yields promising performance, being only 1–2% inferior to the fully supervised methods.

7.5 Discussion

Points are most suitable for objects with uniform shapes and sizes, particularly when there is a large number of objects present. These points indicate the location of the objects. Scribbles, on the other hand, are used to label different semantic elements by marking them and are best suited for objects with uniform shapes but varied sizes. Boxes can provide an approximation of the shape and size information of objects, making them ideal for tasks such as segmentation

TABLE 5
Overview of Annotation-Efficient Learning Studies in Medical Image Analysis

	Reference _{Year}	Application	Organ	Method	Dataset	Results
Tag	Hwang <i>et al.</i> [157] ₂₀₁₆	Detection	Lung; Breast	CAM + Self-Transfer Learning	Private Dataset: 11K X-rays; DDSM; MIAS	AP Shenzhen set: 0.872; MC set: 0.892; MIAS set: 0.326
	Gondal <i>et al.</i> [176] ₂₀₁₇	Detection	Eye	CAM	DRD; DiaretDB1	Hemorrhages SE: 0.91; FP s/I 1.5; Hard Exudates SE: 0.87; FPs/I 1.5; Soft Exudates SE: 0.89; FPs/I: 1.5; RSD SE: 0.52; FPs/I: 1.5
	Wang <i>et al.</i> [177] ₂₀₁₈	Detection	Eye	Expectation-Maximization + Low-Rank Subspace Learning	DRD; Messidor	mAP Kaggle: 0.8394; Messidor: 0.9091
	Nguyen <i>et al.</i> [178] ₂₀₁₉	Segmentation	Eye	CAM + CRF + Active Shape Model	Private Dataset: 40 MRI Images	DSC: T1w: 0.845±0.056; T2w: 0.839±0.049
	Wang <i>et al.</i> [179] ₂₀₂₀	Detection	Lung	CAM + Unsupervised Segmentation	Private Dataset: 540 CT Images	Hit Rate: 0.865
	Shen <i>et al.</i> [180] ₂₀₂₁	Detection	Breast	Globally-aware Multiple Instance Classifier	NYUBCS; CBIS-DDSM	DSC malignant: 0.325 ± 0.231; DSC Benign: 0.240 ± 0.175; AP malignant: 0.396 ± 0.275; AP Benign: 0.283 ± 0.24
	Chen <i>et al.</i> [160] ₂₀₂₂	Segmentation	prostate; Cardiac; Abdominal Organ	Causal Inference; CAM	ACDC; ProMRI; CHAOS	ProMRI DSC: 0.864±0.004; ASD: 3.86±1.20; MSD: 3.85±1.33 ACDC DSC: 0.875±0.008; ASD: 1.62±0.41; MSD: 1.17±0.24 CHAOS DSC: 0.781
Point	Khan <i>et al.</i> [167] ₂₀₁₉	Segmentation	Multi-organ	Confidence Map Supervision	SegTHOR	DSC Aorta: 0.9441 ± 0.0187; Esophagus 0.8983 ± 0.0416;
	Zhao <i>et al.</i> [169] ₂₀₂₀	Segmentation	Cell	Self-/Co-/Hybrid-Training	PHC; Phase100	DSC PHC: 0.871; Phase 100: 0.811
	Dorent <i>et al.</i> [166] ₂₀₂₀	Segmentation	Brain	CNN + CRF	Vestibular-Schwannoma-SEG	DSC: 0.819±0.080; HD95: 3.7±7.4; P: 0.929±0.059
Scribble	Wang <i>et al.</i> [181] ₂₀₁₈	Segmentation	Body	Image-Specific Fine-Tuning	Private Dataset: 18 MRI Images; BRATS	Private DSC: 0.8937±0.0231; BRATS DSC: 0.8811±0.0609
	Lee <i>et al.</i> [182] ₂₀₂₀	Segmentation	Cell	Exponential Moving Average	MoNuSeg	DSC: 0.6408; mIoU: 0.5811
	Zhang <i>et al.</i> [183] ₂₀₂₂	Segmentation	Heart	Mixup + Consistency	ACDC; MSCMRseg	ACDC DSC: 0.848; MSCMRseg DSC: 0.800
Box	Rajchl <i>et al.</i> [184] ₂₀₁₆	Segmentation	Brain; Lung	DenseCRF	Private Dataset: 55 MRI Images	Brain DSC: 0.941±0.041; Lung DSC: 0.829±0.100
	Wang <i>et al.</i> [185] ₂₀₂₂	Segmentation	lymph; Lung; Skin	RECIST measurement propagation algorithm; RECIST Loss; RECIST3D Loss	TCIA; LIDC-IDRI; HAM10000;	TCIA ASSD: 0.866; HD95: 3.263; DSC: 0.785 TCIA ASSD: 0.990; HD95: 3.628; DSC: 0.753 HAM10000 ASSD: 0.314; HD95: 1.299; DSC: 0.832

or detection where objects have high variations in their shape and size. Out of all these annotation types, image tagging is the most efficient, requiring the least amount of annotation cost. Several studies have aimed to reduce the performance gap between different annotation-efficient methods based on various annotations. Future work could explore the following topics: i) integrating multiple supervision signals into a unified learning framework, such as multi-task learning and omni-supervised learning; ii) actively reducing the annotation cost through human-in-the-loop techniques, such as active learning; and iii) mining inherent knowledge from multi-modality data.

8 CHALLENGES AND FUTURE DIRECTIONS

Our comprehensive discussion of label-efficient learning schemes in MIA raises several challenges that should be taken into account to improve the performance of the DL model. In this section, we describe the crucial challenges and shed light on potential future directions for solving these challenges.

8.1 Omni-Supervised Learning

Although the methods we have presented have achieved promising performance, many of them are targeted at addressing *ad hoc* label shortage problems, *i.e.*, these methods do not utilize as much supervision as possible. Served as a special regime of Semi-SL, **Omni-supervised learning** is a crucial trend for label-efficient learning in MIA for the simultaneous utilization of different forms of supervision. Studies [193], [194] have demonstrated the feasibility of omni-supervised learning under teacher-student [57] and the dynamic label assignment [194] pipeline, respectively. In the teacher-student training approach, the model trained on fully annotated datasets serves as the teacher model, and features extracted from the weakly-/un-annotated datasets

serve as guidance to refine the model. Through designated mechanisms, the student model utilizes the teacher model with the provided guidance to further improve performance. Meanwhile, the dynamic label assignment approach forms the crafted metrics from different types of labels in the training process and dynamically gives the final predicted labels.

During the process of omni-supervised learning, however, centralizing or releasing different supervision health data raises multiple ethical, legal, regulatory, and technological issues [195]. On the one hand, collecting and maintaining a high-quality medical dataset consumes a large amount of expense, time, and effort. On the other hand, the privacy of patients may be compromised during the centralization or release of health datasets, even with techniques such as anonymization and safe transfer. To address the privacy preservation problem during model development, researchers proposed **federated learning (FL)** to conduct training in a data-decentralized manner. This approach has yielded fruitful results in The field of MIA [196], [197], [198]. However, current FL algorithms are primarily trained in a supervised manner. When applying the FL to real-world scenarios in MIA, a crucial problem, namely, label deficiency, may appear in local health datasets. Labels may be missing to varying degrees between medical centers, or the granularity of the labels will vary. A promising research direction is to design label-efficient federated learning methods to address this significant problem. For example, semi-supervised learning [199], active learning, and self-supervised learning [200] are suitable to be incorporated into this setting.

8.2 Human-in-the-loop Interaction

The application of expert knowledge to refine the output of the model is often carried out in practice, and there have been various efforts to investigate this field, known as

human-in-the-loop (HITL). The AL scheme can be considered a part of HITL as it involves the introduction of expert knowledge to refine data supervision. Meanwhile, expert knowledge can also be introduced as action supervision under the **reinforcement learning (RL)** schemes to improve the performance of the DL model [201], [202]. In RL scheme, a set of “agents” is formulated to learn expert behaviors in an interactive environment via trial and error. In MIA tasks, RL methods mainly treat the interactive refinement process as the Markov decision process (MDP) and give the solution by the RL process. RL-based interventional model training brings the potential for dealing with rare cases in MIA since the expert-provided interactions can refine the prediction result at the final stage to hinge samples that failed to process by the DL model. In addition, recent developments in diverse learning methodologies, including but not limited to few-shot learning [203], [204] and interpretability-guided learning [205], have contributed to improved efficacy of human-in-the-loop workflows, thereby reducing labor costs in MIA. This indicates a positive trend towards increased cost-effectiveness in this field.

8.3 Generation-based Data Augmentation

Data augmentation with synthesized images produced by generative-based methods is regarded as a way to unlock additional information from the dataset, and leads the way in computation speed and quality of results in the scope of generative methods [206]. In the field of MIA, numerous studies [207], [208] have investigated data augmentation with the original GAN [44] and its variations. However, the unique adversarial training procedure of GANs may suffer from training instability [209] and mode collapse [210], yielding “Copy GAN”, which only generates a limited set of samples [211]. Thus, synthesizing augmented data with high visual realism and diversity is the key challenge of GAN. Meanwhile, the **probabilistic diffusion model** [212], has recently sparked much interest in MIA applications [213]. This model establishes a forward diffusion stage in which the input data is gradually disrupted by adding Gaussian noise over multiple stages and then learns to reverse the diffusion process to obtain the required noise-free data from noisy data samples. Despite their recognized computational overhead [214], diffusion models are generally praised for their high mode coverage and sample quality, and various efforts have been made to ease the computational cost and further improve their generalization capability.

8.4 Generalization Across Domains and Datasets

From semi-supervised learning to annotation-efficient learning, we have introduced a considerable number of methods that address the problem of the low-quantity and/or -quality of labels. Nevertheless, recent results reveal that these novel methods may encounter significant performance degradation when shifting to different domains or datasets. The generalization problem in the MIA field arises due to multiple causes, such as variance among scanner manufacturers, scanning parameters, and subject cohorts. And various current deep learning algorithms cannot be robustly deployed in various real scenarios. To address this practical

problem, the concept of **domain generalization** has been introduced, of which the key idea is to learn a trained model that encapsulates general knowledge so as to adapt to unseen domains and new datasets with little effort and cost. A plethora of methods have been developed to tackle the domain generalization problem [215], such as domain alignment [216], meta-learning [217], data augmentation [218], and so on. MIA has also seen some publications with respect to domain generalization [219], [220]. Further, another challenge for generalization across domains and datasets is that the proposed methods may require numerous labeled multi-source data to extract domain-invariant features. For example, Yuan *et al.* [221] have made a successful attempt to achieve model generalization in source domains with limited annotations by leveraging active learning and semi-supervised domain generalization, eliminating the dilemma between domain generalization and expensive annotations.

8.5 Benchmark Establishment and Comparison

Label-efficient learning in MIA spans multiple tasks, such as classification, segmentation, and detection, as well as multiple organs, such as the retina, lung, and kidney. Differences and variances in tasks and target organs lead to confounding experiment settings and unfair performance comparisons. Meanwhile, a lack of sufficient public health datasets also contributes to this dilemma. For example, many researchers can only conduct experiments to measure the performance of their proposed algorithms based on their own private datasets due to reasons such as privacy. However, few publications have emerged [222] to address the problem, especially for label-efficient learning. Thus, benchmarking remains a pressing problem for model evaluation. On the one hand, the public should urge for the availability of large datasets. On the other hand, a clearly defined set of benchmarking tasks and the corresponding evaluation procedures should be established. Further, specific experimental details should be stipulated to facilitate the comparability of different label-efficient learning algorithms.

9 CONCLUSION

Despite significant advances in computer-aided MIA, the question of how to endow deep learning models with enormous data remains a daunting challenge. Deep learning models under label-efficient schemes have shown significant flexibility and superiority in dealing with high degree of quality- and quantity-variant data. To that end, we have presented the first comprehensive label-efficient learning survey in MIA. A variety of learning schemes, including semi-supervised, self-supervised, multi-instance, active and annotation-efficient learning in the general field are classified and analyzed thoroughly. We hope that by systematically sorting out the methodologies for each learning schemes, this survey will shed light on more progress in the future.

ACKNOWLEDGMENTS

This work was supported by National Natural Science Foundation of China (Project No. 62202403) and Hong Kong Innovation and Technology Fund (Project No. ITS/028/21FP).

APPENDIX A

CONCEPTS OF PRIOR KNOWLEDGE

A.1 Assumptions and Detail in Semi-supervised Learning

A.1.1 Assumptions in Semi-supervised Learning

In fact, Semi-SL is not effective in every scenario. As stated in [223], [224], a necessary condition for Semi-SL algorithms to work is that the marginal data distribution $p(x)$ contains underlying information about the posterior distribution $p(y|x)$, where x and y represent the data sample over input space \mathcal{X} and the associated label, respectively. Otherwise the additional unlabeled data will be useless to infer information about $p(y|x)$, which means the Semi-SL algorithms may achieve similar or even worse performance compared with supervised learning algorithms. Therefore, several assumptions over the input data distribution have been proposed to constrain the data structure and ensure the algorithms can be generalized from a limited labeled dataset to a large-scale unlabeled dataset. Following [224], [225], the assumptions in Semi-SL are introduced as follows:

Smoothness assumption. Suppose $x_1, x_2 \in X$ are two input data samples over input space \mathcal{X} . If the distance between x_1 and x_2 is very close, i.e., $D(x_1, x_2) < \varepsilon$, where ε is an artificially set threshold, then the associated labels y_1 and y_2 should also be the same. Note that sometimes there is an additional constraint in the smoothness assumption. In [225], x_1 and x_2 are required to belong to the same high-density region, so as to avoid the situation that these two samples reside on the brink of different high-density regions and are misclassified as one category.

Cluster assumption. In this assumption, we assume that data points with similar underlying information are likely to form high-density regions, i.e., clusters. If the two data points x_1 and x_2 lie in the same cluster, then they are expected to have the same label. In fact, the cluster assumption can be considered as a special case of the smoothness assumption. According to [226], if the two data points x_1 and x_2 can be connected with a line that does not pass through any low-density area, they belong to the same cluster.

Low-density assumption. The decision boundary of the classifier is assumed to lie in the low-density areas instead of high-density ones, which can be derived from the cluster assumption and smoothness assumption. On the one hand, if the decision boundary resides in the high-density regions, the two data points x_1 and x_2 located in the same cluster but opposite sided of the decision boundary will be categorized as different classes, which obviously violates the cluster assumption and smoothness assumption. On the other hand, following the cluster and smoothness assumption, data points in any high-density areas are expected to be assigned the same label, which means the decision boundary of the model can only lie in the low-density areas, thus satisfying the low-density assumption.

Manifold assumption. A manifold is a concept in geometry, that represents a geometric structure in a high-dimensional space, i.e., a collection of data points in the input space \mathcal{X} . For example, a curve in 2-dimensional space can be thought of as a 1-dimensional manifold, and a surface

in 3-dimensional space can be seen as a 2-dimensional manifold. The manifold assumption states that there is a certain geometry of the data distribution in the high-dimensional space, namely that the data are concentrated around a certain low-dimensional manifold. Due to the fact that high-dimensional data not only poses a challenge to machine learning algorithms, but also leads to a large computational load and the problem of dimensional catastrophe, it will be much more effective to estimate the data distribution if they lie in a low-dimensional manifold.

A.1.2 Details of Key Generative Methods

Researchers can obtain various generative methods according to different assumptions on the latent distribution. On the one hand, it can be easy to formulate a generative method once an assumption on the distribution is made, whereas on the other, the hypothetical generative model must match the real data distribution to avoid the unlabeled data in turn degrading the generalization performance. One can formulate the modeling process of generative methods as follows:

$$\begin{aligned} y^* &= \arg \max_y p(y|x) = \arg \max_y \frac{p(x|y)p(y)}{p(x)} \\ &= \arg \max_y p(x|y)p(y), \end{aligned} \quad (2)$$

where the generative methods models the joint distribution $p(x, y)$. Eq. (2) indicates that if the correct assumption on prior $p(y)$ and conditional distribution $p(x|y)$ is made, the input data can be expected to come from the latent distribution.

Definition of Generative Adversarial Network (GAN)

The aim of generator \mathcal{G} is to iteratively learn the latent distribution from real data x starting from generating data with random noise distribution $p(z)$. Meanwhile, the goal of discriminator \mathcal{D} is to correctly distinguish the fake input generated by \mathcal{G} and real data x . Formally, we can formulate the optimization problem of a GAN as follows:

$$\begin{aligned} \min_{\mathcal{G}} \max_{\mathcal{D}} \mathcal{L}(\mathcal{G}, \mathcal{D}) &= \mathbb{E}_{x \sim p(x)} [\log \mathcal{D}(x)] \\ &\quad + \mathbb{E}_{z \sim p(z)} [1 - \log(\mathcal{D}(\mathcal{G}(z)))], \end{aligned}$$

where \mathcal{L} represents the loss function of generator \mathcal{G} and discriminator \mathcal{D} . Concretely, \mathcal{G} aims to minimize the objective function by confusing \mathcal{D} with generated data $\mathcal{G}(z)$, while \mathcal{D} aims at maximizing the objective function by making correct predictions.

Definition of Variational Autoencoder (VAE) The typical VAE consists of two objectives: one is to minimize the discrepancy between input data x and its reconstruction version \hat{x} produced by the decoder, and the other is to model a latent space $p(z)$ following a simple distribution, such as a standard multivariate Gaussian distribution. Thus, the loss function for training a VAE can be formulated as follows:

$$\min_{\theta} \sum_{x \in X} \mathcal{L}(x, \theta) = \mathcal{L}_{MSE}(x, \hat{x}_{\theta}) + \mathcal{L}_{KL}(p_{\theta}(z|x) || p(z)),$$

where \mathcal{L}_{MSE} represents the mean square error; \hat{x}_{θ} is the reconstruction version of input data x generated by the decoder $p_{\phi}(x|z)$ given parameters ϕ ; $\mathcal{L}_{KL}(\cdot || \cdot)$ represents the

Kullback-Leibler divergence which measures the distance between two distributions; and $p_\theta(z|x)$ denotes the posterior distribution produced by the encoder given parameters θ .

A.2 Conventional Uncertainty Metrics in Active Learning

The uncertainty measure reflects the degree of dispersion of a random input. There are many ways to measure the uncertainty of inputs. Starting with simple metrics like standard deviation and variance, current studies in MIA mainly focus on **margin sampling** [227] and **entropy sampling** [228]. Denote the probability as p , we give the definition of these metrics as follows.

Margin sampling [227] estimates the probability difference \mathcal{M} between the first and second most likely labels \hat{y}_1, \hat{y}_2 according to the deep model parameter θ and expect the least residual value by the following notation:

$$\mathcal{M} = \underset{x}{\operatorname{argmin}} [p_\theta(\hat{y}_1 | x) - p_\theta(\hat{y}_2 | x)]$$

Entropy sampling [228] is another conventional metric for sampling. In a binary or multi-classification scenario, the sampled data with higher entropy can be selected as the expected annotation data. For a C -class task, entropy sampling metric \mathcal{E} can be denoted as follows:

$$\mathcal{E} = \underset{x}{\operatorname{argmax}} \left(- \sum_{c=1}^C p(y_c | x) \log p(y_c | x) \right)$$

APPENDIX B DATASETS

As a supplement to the main text, we summarize representative publicly available datasets across 16 different organs such as the brain, chest, prostate, *etc.* in Tab. 6. These publicly available MIA datasets can be leveraged to construct label-efficient learning algorithms for numerous purposes, including classification, detection, and segmentation.

APPENDIX C SURVEYED PAPERS

Due to space limitations, only a selection of representative papers is presented in the main text. In this section, we will list all the papers we surveyed in the scope of label-efficient learning.

TABLE 6
Summary of publicly available databases for label-efficient learning in MIA

Domain	Dataset (Year)	Task	Link
Brain	BraTS (2012)	Segmentation	http://www.imm.dtu.dk/projects/BRATS2012/data.html
	BraTS (2013) [229]	Segmentation	https://www.smir.ch/BRATS/Start2013#!/download
	BraTS (2015)	Segmentation	https://www.smir.ch/BRATS/Start2015
	BraTS (2017)	Segmentation	https://sites.google.com/site/braintumorsegmentation/
	BraTS (2018)	Segmentation	https://wiki.cancerimagingarchive.net/pages/viewpage.action?pagelId=37224922
	MSD (2018) [230]	Segmentation	https://drive.google.com/drive/folders/1HqEgzS8BV2c7xYNrZdEAnrHk7osJJ--2
	dHCP (2018) [231]	Segmentation	http://www.developingconnectome.org/data-release/
	JSRT Database (2000) [232]	Classification	http://db.jsrt.or.jp/eng.php
	MRBrainS18 (2018)	Segmentation	https://mrbrains18.isi.uu.nl/data/
	BigBrain (2013) [233]	Segmentation	https://bigbrainproject.org/maps-and-models.html#download
	MALC (2012)	Segmentation	http://www.neuromorphometrics.com/2012_MICCAI_Challenge_Data.html
	TCIA (2015) [234]	Segmentation	https://www.cancerimagingarchive.net/
	OASIS (2007)	Segmentation	https://www.oasis-brains.org/#data
	UKBB (2016)	Classification	https://www.ukbiobank.ac.uk/
	ADNI (2010)	Classification	https://www.adni-info.org/
	ABIDE (2016)	Classification	https://fcon_1000.projects.nitrc.org/indi/abide/
	MIRIAD (2012)	Classification	https://www.ucl.ac.uk/drc/research/research-methods/minimal-interval-resonance-imaging-alzheimers-disease-miriad
Chest	IS-COVID (2020) [21]	Segmentation	http://medicalsegmentation.com/covid19/
	CC-COVID (2020) [235]	Segmentation	https://ncov-ai.big.ac.cn/download?lang=en
	NLST (2009)	Detection	https://cdas.cancer.gov/datasets/nlst/
	NIH Chest (2017) [236]	X-ray Classification	https://www.kaggle.com/datasets/nih-chest-xrays/data
	TCGA-Lung	Classification	https://portal.gdc.cancer.gov/repository
	LDCTGC (2016)	Detection	https://www.aapm.org/grandchallenge/lowdosect/
	ChestX (2018) [237]	Classification	https://data.mendeley.com/datasets/rsbjbr9sj/3
	LUNA (2016)	Detection	https://luna16.grand-challenge.org/
	SegTHOR (2017) [238]	Segmentation	https://competitions.codalab.org/competitions/21145
	LIDC-IDRI (2011) [239]	Segmentation	https://wiki.cancerimagingarchive.net/pages/viewpage.action?pagelId=1966254
	CAD-PE (2019)	Segmentation	https://ieee-dataport.org/open-access/cad-pe
	SIIM-ACR (2019)	Segmentation	https://www.kaggle.com/c/siim-acr-pneumothorax-segmentation
	RSNA-Lung (2018)	Detection	https://www.kaggle.com/c/rsna-pneumonia-detection-challenge
	VinDr-CXR (2021)	Detection	https://vindr.ai/datasets/cxr
	Montgomery (2022)	Segmentation	https://www.kaggle.com/datasets/raddar/tuberculosis-chest-xrays-montgomery
	ChestXR (2021)	Classification	https://cxr-covid19.grand-challenge.org/Dataset/
	MIMIC-CXR (2019) [240]	Detection	https://physionet.org/content/mimic-cxr/2.0.0/
	CC-CCII (2020) [235]	Classification	http://ncov-ai.big.ac.cn/download/
	ChestX-ray8 (2017) [236]	Segmentation	https://nihcc.app.box.com/v/ChestXray-NIHCC/
	ChestX-ray14 (2019)	Classification	https://stanfordmlgroup.github.io/competitions/chexpert/
	CheXpert (2019) [236]	Segmentation	https://nihcc.app.box.com/v/ChestXray-NIHCC/

TABLE 6
Summary of publicly available databases for label-efficient learning in MIA (continued)

Domain	Dataset (Year)	Task	Link
Gland	GlaS (2015) [241]	Segmentation	https://warwick.ac.uk/fac/cross_fac/tia/data/glascontest/download/
	CRAG (2017)	Segmentation	https://warwick.ac.uk/fac/sci/dcs/research/tia/data/mildnet
Prostate	Prostate-MRI-US-Biopsy (2013) [242]	Segmentation	https://wiki.cancerimagingarchive.net/pages/viewpage.action?pageId=68550661
	PANDA (2020) [243]	Classification	https://www.kaggle.com/c/prostate-cancer-grade-assessment/data/
	ProMRI (2012) [244], [245]	Segmentation	https://promise12.grand-challenge.org/
	TMA-Zurich (2018) [246]	Classification	https://www.nature.com/articles/s41598-018-30535-1?source=app#data-availability
	GGC (2019)	Classification	https://gleason2019.grand-challenge.org/Register/
Heart	MSCMRseg [247]	Segmentation	https://zmiclab.github.io/zxh/0/mscmrseg19/
	MM-WHS (2017)	Segmentation	https://zmiclab.github.io/zxh/0/mmwhs/
	Endocardium-MRI (2008) [248]	Segmentation	https://www.sciencedirect.com/science/article/pii/S1361841508000029#aep-e-component-id41
	M&Ms (2020)	Segmentation	https://www.ub.edu/mnms/
	ASG (2018) [249]	Segmentation	http://atriaseg2018.cardiacatlas.org/
Eye	DRISHTI-GS (2014) [250]	Segmentation	https://www.kaggle.com/datasets/lokeshaipureddi/drishtigs-retina-dataset-for-onh-segmentation
	REFUGE [251]	Segmentation	https://ieee-dataport.org/documents/refuge-retinal-fundus-glaucoma-challenge
	DRD (2015) [252]	Detection	https://www.kaggle.com/competitions/diabetic-retinopathy-detection
	RetinalOCT (2018) [237]	Classification	https://www.kaggle.com/datasets/paultimothymooney/kernany2018
	ReTOUCH (2017) [253]	Classification	https://retouch.grand-challenge.org/
	ORIGA-light (2010) [254]	Classification	https://www.medicmind.tech/retinal-image-databases
	sjchoi86-HRF (2017)	Classification	https://github.com/cvblab/retina_dataset
	DRIVE (2004)	Classification	https://drive.grand-challenge.org/
	Isfahan MISP (2017)	Segmentation	https://www.ncbi.nlm.nih.gov/pmc/articles/PMC5394805/
	Duke-AMD (2014) [255]	Classification	https://people.duke.edu/~sf59/RPEDC_Opth_2013_dataset.htm
	ADAM (2020) [256]	Segmentation	https://amd.grand-challenge.org/
	PALM (2019) [257]	Segmentation	https://palm.grand-challenge.org/
	FFA (2012) [258]	Classification	http://misp.mui.ac.ir/data/eye-images.html
	OCTA-500 (2022)	Classification	https://ieee-dataport.org/open-access/octa-500
	GAMMA (2021)	Classification	https://aistudio.baidu.com/aistudio/competition/detail/119/0/introduction
Kidney	Messidor (2014) [259]	Classification	https://www.adcis.net/en/third-party/messidor/
	KiT5 (2019)	Segmentation	https://kits21.kits-challenge.org/
Skin	HAM10000 (2018) [260]	Segmentation	https://dataverse.harvard.edu/dataset.xhtml?persistentId=doi:10.7910/DVN/DBW86T
	ISIC (2016) [261]	Classification	https://challenge.isic-archive.com/data/#2016
	ISIC (2017) [262]	Segmentation	https://challenge.isic-archive.com/data/#2017/
	ISIC (2018) [263]	Segmentation	https://challenge.isic-archive.com/landing/2018/
Hand	RSNA-Bone (2017) [264]	Segmentation	https://www.rsna.org/education/ai-resources-and-training/ai-image-challenge/rsna-pediatric-bone-age-challenge-2017/
Colon	KATHER (2018) [265]	Classification	https://zenodo.org/record/1214456#.Y8fgV-zP1hE
	MHIST (2021)	Classification	https://bmirds.github.io/MHIST/
	CRCHistoPhenotypes (2016) [266]	Classification	https://warwick.ac.uk/fac/cross_fac/tia/data/crchistolabelednuclei
Abdomen	ACDC (2018) [267]	Segmentation	https://www.creatis.insa-lyon.fr/Challenge/acdc/databases.html
	CHAOS (2021) [268]	Segmentation	https://chaos.grand-challenge.org/

TABLE 6
Summary of publicly available databases for label-efficient learning in MIA (continued)

Domain	Dataset (Year)	Task	Link
Breast	BACH (2018) [269]	Classification	https://iciar2018-challenge.grand-challenge.org/Dataset/
	NYUBCS (2019) [270]	Segmentation	https://datacatalog.med.nyu.edu/dataset/10518
	CBIS-DDSM (2017) [271]	Segmentation	https://www.kaggle.com/datasets/awsaf49/cbis-ddsm-breast-cancer-image-dataset
	MIAS (2015) [272]	Detection	https://www.kaggle.com/datasets/kmader/mias-mammography
	TCGA-Breast	Classification	https://portal.gdc.cancer.gov/repository
	INBreast (2012)	Classification	https://biokeanos.com/source/INBreast
	BreastPathQ (2019)	Classification	https://breastpathq.grand-challenge.org/Overview/
	CAMELYON (2016)	Classification	https://camelyon16.grand-challenge.org/Data/
	CAMELYON (2017)	Classification	https://camelyon17.grand-challenge.org/Data/
	BreakHis (2016)	Classification	https://web.inf.ufpr.br/vri/databases/breast-cancer-histopathological-database-breakhis/
	CBCS3 (2018) [273]	Classification	https://unclineberger.org/cbcs/for-researchers/
	TNBC (2018) [274]	Segmentation	https://ega-archive.org/datasets/EGAD00001000063
	TUPAC (2016) [275]	Segmentation	https://github.com/CODAIT/deep-histopath
	MITOS12 [276]	Segmentation	http://ludo17.free.fr/mitos_2012/dataset.html
	MITOS14 [277]	Segmentation	https://mitos-atypia-14.grand-challenge.org/Dataset/
Cell	TMA-UCSB (2014) [278]	Classification	https://bioimage.ucsb.edu/research/biosegmentation
	PHC (2013) [279]	Segmentation	http://celltrackingchallenge.net/
Liver	CPM (2017) [280]	Segmentation	http://simbad.u-strasbg.fr/simbad/sim-id?Ident=CPM+17
	LiTS (2017)	Segmentation	https://competitions.codalab.org/competitions/17094
Lymph Node	PAIP (2019)	Segmentation	https://paip2019.grand-challenge.org/Dataset/
	PatchCAMELYON (2017)	Classification	https://patchcamelyon.grand-challenge.org/Download/
Pancreas	NIH LN (2016)	Classification	https://wiki.cancerimagingarchive.net/pages/viewpage.action?pageId=19726546
	NIH PCT	Segmentation	https://wiki.cancerimagingarchive.net/display/Public/Pancreas-CT
Multi-organ	DSB (2018)	Segmentation	https://www.kaggle.com/competitions/data-science-bowl-2018/data
	DeepLesion (2018) [281]	Detection	https://nihcc.app.box.com/v/DeepLesion
	WTS (2020) [282]	Super-resolution	https://www.nature.com/articles/s42003-020-01151-5#data-availability
	DECATHLON (2019) [230]	Segmentation	http://medicaldecathlon.com/
	MoNuSeg (2017) [283]	Segmentation	https://monuseg.grand-challenge.org/
	MoCTSeg (2018) [284]	Segmentation	https://www.synapse.org/#!Synapse:syn3376386
	BTCV (2017) [285]	Segmentation	https://zenodo.org/record/1169361#.Y8Ud-OxBwUE
	CT-ORG [286], [287]	Segmentation	https://wiki.cancerimagingarchive.net/pages/viewpage.action?pageId=61080890
	NIH PLCO (2011) [288]	Classification	https://cdas.cancer.gov/datasets/plco/
	BCV (2017)	Segmentation	https://www.synapse.org/#!Synapse:syn3193805/files/
	MIDOG [289]	Segmentation	https://imig.science/midog/the-dataset/

TABLE 7
Surveyed Semi-supervised Learning-based Studies in Medical Image Analysis

	Reference _{Year}	Organ	Semi-SL Algorithm Design	Dataset	Result
Classification	Madani <i>et al.</i> [6] ₂₀₁₈	Lung	Semi-supervised GAN	NIH PLCO; NIH Chest X-Ray	Acc (Accuracy): 0.851
	Diaz-Pinto <i>et al.</i> [7] ₂₀₁₉	Retina	Semi-supervised DCGAN	ORIGA-light; DRISHTI-GS; RIM-ONE; HRF; DRD; sjchoi86-HRF; ACRIMA; DRIVE; Messidor	AUC: 0.9017
	Gyawali <i>et al.</i> [55] ₂₀₁₉	Lung	Temporal Ensembling + VAE	Chexpert	AUC: 0.6697
	Su <i>et al.</i> [290] ₂₀₁₉	Nuclei	Mean Teacher + Label Propagation	MoNuseg; Private Dataset: 17516 nuleus	MoNuseg: F1: 0.783; Private Dataset: F1: 0.7991
	Shi <i>et al.</i> [8] ₂₀₂₀	Lung; Breast	Graph Temporal Ensembling	TCGA-Lung; TCGA-Breast	TCGA-Lung: F1: 0.893; TCGA-Breast: F1: 0.930
	Gyawali <i>et al.</i> [60] ₂₀₂₀	Lung; Skin	Mixup on Input and Latent Space	Chexpert; ISIC 2018	Chexpert: AUC: 0.6847; ISIC: AUC: 0.9073
	Kamran <i>et al.</i> [46] ₂₀₂₁	Retina	Semi-supervised GAN + ViT	FFA	FID (Fréchet inception distance): 17.3; KID (Kernel inception distance):0.0053
	Yu <i>et al.</i> [9] ₂₀₂₁	Colon	Mean Teacher	Private Dataset: 13,111 Images	Patch-level AUC: 0.980; Patient-level AUC: 0.974
	Marini <i>et al.</i> [291] ₂₀₂₁	Prostate	Teacher-student model	TMA-Zurich; TCGA-PRAD	QWK (Quadratic Weighted Kappa): TMA-Zurich: 0.7645; TCGA-PRAD: 0.4529
	Wang <i>et al.</i> [10] ₂₀₂₁	Breast; Retina	Virtual Adversarial Training + Self-training	RetinalOCT; Private Dataset: 39,904 Images	Acc: 0.9513; Macro-R (Macro-Recall): 0.9330
	Liu <i>et al.</i> [11] ₂₀₂₂	Lung; Skin	Anti-curriculum Self-training	ChestX-Ray14; ISIC 2018	ChestX-ray14: AUC: 0.8177; ISIC: AUC: 0.9436
	Wen <i>et al.</i> [292] ₂₀₂₂	Brain	Multi-scale clustering	UKBB; ADNI	Acc: 0.89
	Zhang <i>et al.</i> [12] ₂₀₂₂	Spinal cord	Consistency Regularization + Pseudo-labeling + Active Learning	Private Dataset: 7,295 Images;	Acc: 0.9582; Macro-P (Macro-Precision): 0.8609
	Sedai <i>et al.</i> [49] ₂₀₁₇	Retina	Teacher-student VAE	DRD	DSC: 0.80
	Bai <i>et al.</i> [13] ₂₀₁₇	Heart	CRF-based Self-training	Private Dataset: 8050 Images	DSC: 0.920
	Li <i>et al.</i> [14] ₂₀₁₈	Skin	II-model	ISIC 2017	DSC: 0.874; Acc: 0.943
	Nie <i>et al.</i> [15] ₂₀₁₈	Prostate	Self-training	Private Dataset: 70 Images	DSC: 0.970; ASD (Average Surface Distance): 1.401
	Yu <i>et al.</i> [16] ₂₀₁₉	Heart	Uncertainty-aware Mean Teacher	ASG	DSC: 0.8888; 95HD: 7.32; JI: 0.8021
	Sedai <i>et al.</i> [293] ₂₀₁₉	Retina	Uncertainty-aware Teacher-student model	Private Dataset: 570 Images	DSC: 0.91
	Zhou <i>et al.</i> [17] ₂₀₁₉	Multi-Organ	Multi-planar Co-training	Private Dataset: 310 Volumes	DSC: 0.7794
	Zhao <i>et al.</i> [40] ₂₀₁₉	Brain	Co-training + Knowledge Distillation	MALC; OASIS	MALC: DSC: 0.792
	Cao <i>et al.</i> [54] ₂₀₂₀	Breast	Uncertainty-aware Temporal Ensembling	Private Dataset: 170 Volumes; ISIC 2017	Private Dataset: DSC: 0.7287; ISIC 2017: DSC: 0.8178
	Li <i>et al.</i> [18] ₂₀₂₀	Liver; Retina; Skin	Transformation-consistent Mean Teacher	ISIC 2017; REFUGE; LITS	ISIC: DSC: 0.8344; REFUGE: DSC: 0.9543; LITS: DSC: 0.9427
	Liu <i>et al.</i> [19] ₂₀₂₀	Skin; Lung	Mean Teacher + Sample Relation Consistency	ISIC 2018; ChestX-ray14	ISIC: AUC: 0.9358; ChestX-ray8: AUC: 0.7923
	Xie <i>et al.</i> [294] ₂₀₂₀	Colon	Pairwise Relation Network	GlaS; CRAG	GlaS: DSC: 0.906; CRAG: DSC: 0.892
	Li <i>et al.</i> [20] ₂₀₂₀	Heart	Shape-aware Consistency Regularization	ASG	DSC: 0.8954; JI (Jaccard Index): 0.8124
	Wang <i>et al.</i> [58] ₂₀₂₀	Heart; Kidney	Double Uncertainty-Weighted Mean Teacher	ASG; KITS	ASG: DSC: 0.8965; KITS: DSC: 0.8879
	Zhou <i>et al.</i> [295] ₂₀₂₀	Cervix	Masked Mean Teacher	Private Dataset: 5,480 Images	AJI (Averaged Jaccard Index): 0.6694; mAP: 0.4052
	Qu <i>et al.</i> [36] ₂₀₂₀	Multi-Organ	Self-training + Background Propagation	MoNuSeg; Private Dataset: 40 Images	MoNuSeg: F1: 0.8282; Private Dataset: F1: 0.8879
	Xia <i>et al.</i> [41] ₂₀₂₀	Pancreas; Abdomen	Uncertainty-aware Co-training	NIH PCT; MoCTSeg	NIH PCT: DSC: 0.8118
	Li <i>et al.</i> [296] ₂₀₂₀	Multi-Organ	Self-training + Self-supervised Learning	MoNuSeg; ISIC 2017	MoNuSeg: F1: 0.7910; ISIC: F1: 0.8617
	Fan <i>et al.</i> [21] ₂₀₂₀	Lung	Attention Self-training	IS-COVID	DSC: 0.739
Segmentation	Fang <i>et al.</i> [43] ₂₀₂₀	Kidney; Brain	End-to-end Co-training	KITS; BraTS 2018	KITS: mIoU: 0.902; BraTS: mIoU: 0.854
	Chaitanya <i>et al.</i> [22] ₂₀₂₁	Heart; Prostate; Pancreas	Semi-supervised GAN + Deformation and Additive Intensity Field	ACDC; DECATHLON	ACDC: DSC (Dice coefficient): 0.834; DECATHLON: DSC: 0.529
	Xu <i>et al.</i> [297] ₂₀₂₁	Prostate	Shadow-consistent Mean Teacher	Prostate-MRI-US-Biopsy; Private Dataset: 662 volumes	Prostate: DSC: 0.9225; Private Dataset: DSC: 0.9012
	Huo <i>et al.</i> [298] ₂₀₂₁	Pancreas	Asynchronous Teacher-student	NIH PCT; DECATHLON	NIH PCT: DSC: 0.8370; DECATHLON: DSC: 0.7671
	Wang <i>et al.</i> [42] ₂₀₂₁	Heart; Spleen; Prostate	Self-paced Co-training	ACDC; DECATHLON; ProMRI	DSC: ACDC: 0.8778; DECATHLON: 0.8835; ProMRI: 0.7616
	Luo <i>et al.</i> [23] ₂₀₂₁	Nasopharynx	Uncertainty Rectified Pyramid Consistency	Private Dataset: 258 MR Images	DSC: 0.8076
	Shi <i>et al.</i> [299] ₂₀₂₁	Pancreas; Heart	Uncertainty Estimation + Self-training	NIH PCT; ACDC; Endocardium MRI	DSC: NIH PCT: 0.6701; ACDC: 0.8610; Endocardium MRI: 0.8667
	Hu <i>et al.</i> [300] ₂₀₂₁	Hippocampus; Heart	Semi-supervised Contrastive Learning	DECATHLON; MM-WHS	DECATHLON: DSC: 0.866; MM-WHS: DSC: 0.764;
	Luo <i>et al.</i> [24] ₂₀₂₁	Heart;	Dual-task Consistency	ASG; NIH PCT	ASG: DSC: 0.8942; NIH PCT: DSC: 0.7827;
	Li <i>et al.</i> [301] ₂₀₂₁	Lung	Uncertainty-guided Dual Consistency	Private Dataset: 852 Volumes	DSC: 0.774; JI: 0.645
	Li <i>et al.</i> [25] ₂₀₂₁	Lung; Skin; Liver	StyleGAN2	ChestX-ray14; JSRT Database; ISIC 2018; LITS; CHAOS	DSC: Lung: 0.9668; ISIC: 0.8329; LITS: 0.9169
	You <i>et al.</i> [26] ₂₀₂₂	Heart; Pancreas	Mean Teacher + Contrastive Learning	ASG; NIH PCT	ASG: DSC: 0.9085; NIH PCT: DSC: 0.7539
	Wang <i>et al.</i> [27] ₂₀₂₂	Heart; Prostate	Mean Teacher + Contrastive Learning	ACDC; ProMRI	ACDC: DSC: 0.914; ProMRI: DSC: 0.704
	Wu <i>et al.</i> [28] ₂₀₂₂	Heart; Pancreas	Uncertainty-based Mutual Consistency	ASG; NIH PCT; ACDC	DSC: ASG: 0.9107; NIH PCT: 0.8059; ACDC: 0.8851
	Wu <i>et al.</i> [302] ₂₀₂₂	Heart; Retina	Risk Minimization	ACDC; REFUGE; MM-WHS	DSC: ACDC: 0.8392; REFUGE: 0.9126; MM-WHS: 0.8317
	Wang <i>et al.</i> [50] ₂₀₂₂	Kidney; Heart; Liver	Generative Bayesian Deep Learning	KITS; ASG; DECATHLON	DSC: KITS: 0.898; ASG: 0.884; DECATHLON: 0.935
	Gao <i>et al.</i> [303] ₂₀₂₂	Heart	Mean Teacher	ACDC	DSC: 0.7954
	Luo <i>et al.</i> [29] ₂₀₂₂	Heart	Co-training Variant	ACDC	DSC: 0.864
Detection	Wang <i>et al.</i> [30] ₂₀₂₀	Lung	MixMatch + Focal Loss	LUNA; NLST	LUNA: CPM: 0.872
	Zhou <i>et al.</i> [31] ₂₀₂₁	Multi-Organ	Teacher-student Model + Adaptive Consistency Loss	DSB; DeepLesion	DSB: mAP: 0.694; DeepLesion: Sens (Sensitivity): 0.779

TABLE 8
Surveyed Self-supervised Learning-based Studies in Medical Image Analysis

	Reference _{Year}	Organ	Proxy Task Design	Dataset	Result
Classification	Li <i>et al.</i> [62] ₂₀₂₀	Retina	Multi-modal Contrastive Learning	ADAM; PALM	ADAM: AUC: 0.7458; PALM: AUC: 0.9855;
	Zhao <i>et al.</i> [90] ₂₀₂₁	Retina; Lung	Inpainting; Local Pixel Shuffling; Non-Linear Intensity Transformation	RetinalOCT; ChestX	RetinalOCT: AUC: 0.9642; F1: 0.9342 ChestX: AUC: 0.8265; F1: 0.8214
	Koohbanani <i>et al.</i> [63] ₂₀₂₁	Breast; Cervix; Colon	Magnification Prediction; Solving Magnification Puzzle; Hematoxylin Channel Prediction	CAMELYON 2016; KATHER; Private Dataset: 217 Images	CAMELYON 2016: AUC: 0.937; KATHER: AUC: 0.951; Private Dataset: AUC: 0.974
	Li <i>et al.</i> [91] ₂₀₂₁	Retina	Image Rotation	ADAM; PALM; DRD	ADAM: AUC: 0.7811; PALM: AUC: 0.9912
	Azizi <i>et al.</i> [64] ₂₀₂₁	Skin; Lung	Multi-Instance Contrastive Learning	Private Dermatology Dataset; CheXpert	Private: Top-1 Acc: 0.7002; CheXpert: AUC: 0.7729
	Yang <i>et al.</i> [100] ₂₀₂₂	Colon	Cross-stain prediction + Contrastive Learning	KATHER	Acc: 0.918
	Tiu <i>et al.</i> [65] ₂₀₂₂	Lung	Contrastive Learning	CheXpert	AUC: 0.889
	Chen <i>et al.</i> [66] ₂₀₂₂	Breast; Lung; Kidney	Contrastive Learning	TCGA-BRCA; TCGA-NSCLS; TCGA-RCC	AUC: TCGA-Breast: 0.874; TCGA-NSCLS: 0.952; TCGA-RCC: 0.980
	Mahapatra <i>et al.</i> [67] ₂₀₂₂	Lymph; Lung; Retina; Prostate	Contrastive Learning Variant	CAMELYON 2017; DRD; GGC ChestX-ray14; CheXpert;	Acc: CAMELYON 2017: 0.929; DRD: 0.951; GGC: 0.916; ChestX-ray14: Acc: 0.861; ChestXpert: Acc: 0.913
	Cai <i>et al.</i> [304] ₂₀₂₂	Retina	Masked Image Modeling	ADAM; PALM; OCTA-500; GAMMA	AUC: ADAM: 0.8585; PALM: 0.9853; OCTA(2D): 0.834; GAMMA(2D): 0.97; OCTA(3D): 0.8639; GAMMA(3D): 0.6618
Segmentation	Hervella <i>et al.</i> [68] ₂₀₁₈	Retina	Multi-modal Reconstruction	Isfahan MISP	AUC: 0.8183
	Spitzer <i>et al.</i> [69] ₂₀₁₈	Brain	Patch Distance Prediction	BigBrain	DSC: 0.80
	Bai <i>et al.</i> [70] ₂₀₂₀	Heart	Anatomical Position Prediction	Private Dataset: 3825 Subjects	DSC: 0.934
	Sahasrabudhe <i>et al.</i> [71] ₂₀₂₀	Multi-Organ	WSI Patch Magnification Identification	MoNuSeg	AJL: 0.5354; AHD (Average Hausdorff Distance): 7.7502
	Tao <i>et al.</i> [72] ₂₀₂₀	Pancreas	Rubik's Cube Recovery	NIH PCT; MRBrainS18	NIH PCT: DSC: 0.8408; MRBrainS18: DSC: 0.7756
Regression	Lu <i>et al.</i> [73] ₂₀₂₁	Brain	Fiber Streamlines Density Map Prediction; Registration-based Segmentation Imitation	dHCP	DSC: 0.822;
	Tang <i>et al.</i> [74] ₂₀₂₂	Abdomen; Liver; Prostate	Contrastive Learning; Masked Volume Inpainting; 3D Rotation Prediction	DECATHLON; BTCV	DECATHLON: DSC: 78.68; BTCV: DSC: 0.918
	Abbet <i>et al.</i> [75] ₂₀₂₀	Gland	Image Colorization	Private Dataset: 660 Images	Brier Score: 0.2725; C-Index: 0.6943
	Srinidhi <i>et al.</i> [76] ₂₀₂₀	Breast; Colon	WSI Patch Resolution Sequence Prediction	BreastPathQ; CAMELYON 2016; KATHER	BreastPathQ: ICC Coefficient: 0.907; CAMELYON 2016: AUC: 0.882; KATHER: Acc: 0.986; F1: 0.934
	Zhuang <i>et al.</i> [77] _{2019CS}	Brain	Rubik's Cube Recovery	BraTS 2018; Private Dataset: 1,486 Images	BraTS 2018: mIoU: 0.773; Private: Acc: 0.838
Others	Chen <i>et al.</i> [78] _{2019CDS}	Multi-Organ	Disturbed Image Context Restoration	Private Fetus Dataset: 2,694 Images; Private Multi-organ Dataset: 150 Images; BraTS 2017	Private Fetus Dataset: F1: 0.8942; Private Multi-organ Dataset: Mean Distance: 2.90 BraTS 2017: DSC: 0.8557
	Zhao <i>et al.</i> [79] _{2020SR}	Brain	Super-resolution Reconstruction	Private Dataset: 47 Images	S3 Sharpness: 0.5482
	Li <i>et al.</i> [80] _{2020DN}	Abdomen	CT Reconstruction	LDCTGC	PSNR: 22.1758; SSIM: 0.7800
	Cao <i>et al.</i> [81] _{2020IT}	Brain	Missing Modality Synthesis	BraTS 2015; ADNI	ADNI: IS (Inception Score): 2.15; FID: 64.29
	Haghighi <i>et al.</i> [82] _{2020CS}	Lung	Self-Discovery + Self-Classification +Self-Restoration	LUNA; LiTS; CAD-PE; BraTS 2018; ChestX-ray14; LIDC-IDRI; SIIM-ACR	Classification: LUNA: AUC: 0.9847; Segmentation: IoU: LiTS: 0.8560; BraTS 2018: 0.6882
	Taleb <i>et al.</i> [83] _{2020DS}	Brain; Retina; Pancreas	3D Contrastive Predictive Coding; 3D Jigsaw Puzzles; 3D Rotation Prediction; 3D Exemplar Networks Relative 3D Patch Location;	BraTS 2018; DECATHLON; DRD	BraTS 2018: DSC: 0.9080; DECATHLON: DSC \approx 0.635; DRD: DSC \approx 0.80
	Li <i>et al.</i> [84] _{2021SR}	Breast; Pancreas; Kidney	Super-resolution Reconstruction; Color Normalization	WTS; Private Dataset: 533 Images	PSNR: 28.32; SSIM: 0.8304
	Wang <i>et al.</i> [85] _{2021CS}	Multi-Organ	Contrastive Learning	TCGA; KATHER; MHIST PAIP; PatchCAMELYON	MHIST: F1: 0.0.8993; KATHER: F1: 0.9582; PatchCAMELYON: F1: 0.8983; AUC: 0.9779
	Zhou <i>et al.</i> [86] _{2021CS}	Lung; Brain; Liver	Contrastive Learning + Image Reconstruction	ChestX-ray14; CheXpert; LUNA BraTS 2018; LiTS;	AUC: Chest: 0.831; LUNA: 0.922; DSC: LiTS: 0.937; BraTS 2018: 0.85
	Yan <i>et al.</i> [87] _{2022RE}	Multi-Organ	Global and Local Contrastive Learning	DeepLesion; NIH LN; Private Dataset: 94 Patients	Mean Radial Error: 4.3; Maximum Radial Error: 16.4
	Cai <i>et al.</i> [88] _{2022CD}	Lung; Brain; Retina	Dual-Distribution Reconstruction	RSNA-Lung; LAG; VinDr-CXR; Brain Tumor MRI; Private Lung Dataset: 5,000 Images	AUC: RSNA-Lung: 0.913; Brain Tumor MRI: 0.972; VinDr-CXR: 0.859; LAG: 0.931; Private Lung Dataset: 0.710;
	Haghighi <i>et al.</i> [89] _{2022CS}	Lung	Contrastive Learning + Reconstruction + Adversarial Learning	ChestX-ray14; CheXpert; Montgomery	AUC: ChestX-ray14: 0.8112; CheXpert: 0.8759; Montgomery: DSC: 0.9824
	Xie <i>et al.</i> [305] _{2022CS}	Multi-Organ	Contrastive Learning	BCV; RICORD; JSRT Database; ChestXR	BCV: DSC: 0.8499; RICORD: AUC: 0.8906; JSRT Database: DSC: 0.9408; ChestXR: AUC: 0.9907

¹ For the sake of brevity, we denote references that contain more than one task in the following abbreviations: C: Classification, S: Segmentation, D: Detection, SR: Super-resolution, DN: Denoising, IT: Image Translation, RE: Registration.

TABLE 9
Surveyed Multi-instance Learning-based Studies in Medical Image Analysis

	Reference ^{Year}	Organ	MIL Algorithm Design	Dataset	Result
Classification	Manivannan <i>et al.</i> [103] ₂₀₁₇	Retina; Breast	Discriminative Subspace Transformation + Margin-based Loss	Messidor; TMA-UCSB; DR Dataset; Private Dataset: 884 Images	Messidor: Acc: 0.728; TMA-UCSB: AUC: 0.967; DR Dataset: Acc: 0.8793; Private: Kappa: 0.7212
	Zhu <i>et al.</i> [306] ₂₀₁₇	Breast	Sparse MIL	INBreast	AUC: 0.89
	Mercan <i>et al.</i> [132] ₂₀₁₇	Breast	Multi-Label MIL	BCSC	Average-P (Average-Precision): 0.8068
	Ilse <i>et al.</i> [104] ₂₀₁₇	Breast; Colon	Attention-based MIL	TMA-UCSB; CRCHistoPhenotypes	TMA-UCSB: Acc: 0.755; CRCHistoPhenotypes: Acc: 0.898
	Couture <i>et al.</i> [105] ₂₀₁₈	Breast	Quantile Function-based MIL	CBCS3	Acc: 0.952
	Das <i>et al.</i> [135] ₂₀₁₈	Breast	Multiple Instance Pooling	BreakHis	Acc: 0.8906
	Liu <i>et al.</i> [106] ₂₀₁₈	Brain	Landmark-based MIL	ADNI; MIRIAD	ADNI: AUC: 0.9586; MIRIAD: AUC: 0.9716
	Campanella <i>et al.</i> [107] ₂₀₁₉	Prostate; Skin; Lymph	MIL + RNN	Private Dataset: 44,732 Images	AUC: Prostate: 0.986; Skin: 0.986; Lymph: 0.965
	Wang <i>et al.</i> [108] ₂₀₁₉	Breast	Instance Features Recalibration	Private Dataset: 608 Images	Acc: 0.865
	Tennakoon <i>et al.</i> [136] ₂₀₁₉	Retina; Lung	Extreme Value Theorem-based MIL	ReTOUCH; DLCST	DLCST: AUC: 0.96
	Yao <i>et al.</i> [109] ₂₀₁₉	Lung; Brain	Multiple Instance FCN	NLST; TCGA	NLST: C-Index: 0.678; TCGA: C-Index: 0.657
	Wang <i>et al.</i> [110] ₂₀₂₀	Retina	Uncertainty-aware MIL + RNN Aggregation	Duke-AMD; Private Dataset: 4,644 Volumes	Acc: Duke-AMD: 0.979; Private Dataset: 0.951
	Zhao <i>et al.</i> [111] ₂₀₂₀	Colon	VAE-GAN Feature Extraction + GNN Bag-level Representation Learning	TCGA-COAD	Acc: 0.6761; F1: 0.6667; AUC: 0.7102
	Chikontwe <i>et al.</i> [112] ₂₀₂₀	Colon	Jointly Learning of Instance- and Bag-level Feature	Private Dataset: 366 Images	F1: 0.9236; P (Precision): 0.9254; R (Recall): 0.9231; Acc: 0.9231
	Raju <i>et al.</i> [113] ₂₀₂₀	Colon	Graph Attention MIL	MCO	Acc: 0.811; F1: 0.798
	Han <i>et al.</i> [114] ₂₀₂₀	Lung	Automatic Instance Generation	Private Dataset: 460 Examples	AUC: 0.99
	Yao <i>et al.</i> [115] ₂₀₂₀	Lung; Colon	Siamese Multi-instance FCN + Attention MIL	NLST; MCO	NLST: AUC: 0.7143; MCO: AUC: 0.644
	Hashimoto <i>et al.</i> [116] ₂₀₂₀	Lymph	Domain Adversarial + Multi-scale MIL	Private Dataset: 196 Images	Acc: 0.871
	Shao <i>et al.</i> [117] ₂₀₂₁	Breast; Lung; Kidney	Transformer-based MIL	CAMELYON 2016; TCGA-NSCLC; TCGA-RCC	Acc: CAMELYON: 0.8837; TCGA-NSCLC: 0.8835; TCGA-RCC: 0.9466
	Li <i>et al.</i> [118] ₂₀₂₁	Breast; Lung	Dual-stream MIL + Contrastive Learning	CAMELYON 2016; TCGA Lung Cancer	CAMELYON 2016: AUC: 0.9165; TCGA: AUC: 0.9815
	Li <i>et al.</i> [119] ₂₀₂₁	Lung	Virtual Bags + Self-SL Location Prediction	Private Dataset: 460 Examples	AUC: 0.981; Acc: 0.958; F1: 0.895; Sens: 0.936
	Lu <i>et al.</i> [120] ₂₀₂₁	Kidney; Lung; Lymph node	Attention-based MIL + Clustering	TCGA-RCC + Private Dataset: 135 WSIs; CPTAC-NSCLC + Private Dataset: 131 WSIs; CAMELYON 2016,17 + Private Dataset: 133 WSIs	Kidney: AUC: 0.972; Lung: AUC: 0.975; Lymph node: AUC: 0.940
	Wang <i>et al.</i> [121] ₂₀₂₂	Thyroid	Transformer-based MIL + Knowledge Distillation	Private Dataset: 595 Images	AUC: 0.9835; P: 0.9482; R: 0.9151; F1: 0.9297
	Zhang <i>et al.</i> [122] ₂₀₂₂	Breast; Lung	Double-Tier Feature Distillation MIL	CAMELYON 2016; TCGA-Lung	CAMELYON 2016: AUC: 0.946; TCGA-Lung: AUC: 0.961
	Schirris <i>et al.</i> [123] ₂₀₂₂	Breast; Colon	Heterogeneity-aware MIL + Contrastive Learning	TCGA-CRCK; TCGA-BC	TCGA-CRCK: AUC: 0.87; TCGA-BC: AUC: 0.81
Segmentation	Su <i>et al.</i> [124] ₂₀₂₂	Breast; Kidney	Intelligent Sampling Method + Attention MIL	CAMELYON 2016; Private Dataset: 112 Images	CAMELYON 2016: AUC: 0.891; Private: AUC: 0.974
	Zhu <i>et al.</i> [125] ₂₀₂₂	Breast; Lung; Kidney	Reinforcement Learning + Contrastive Learning + MIL	CAMELYON 2016; TCGA-Lung; TCGA-Kidney	AUC: CAMELYON: 0.9452; TCGA-Lung: 0.9637; TCGA-Kidney: 0.9573
Others	Yang <i>et al.</i> [126] ₂₀₂₂	Colon; Muscle	Curriculum Learning + MIL	CRCHistoPhenotypes; Private Muscle Dataset: 266 Images	CRCHistoPhenotypes: AUC: 0.898; Private: AUC: 0.907
	Jia <i>et al.</i> [127] ₂₀₁₇	Colon	Multi-scale MIL + Area Constraint Regularization	Private TMA/Colon Dataset: 60 Images/910 Images	F1: TMA: 0.622; Colon: 0.836
Segmentation	Xu <i>et al.</i> [128] ₂₀₁₉	Breast	Instance-level and Pixel-level Label Generation	CAMELYON 2016	Image-level Acc: 0.929; Pixel-level IoU: 0.847
	Dov <i>et al.</i> [129] ₂₀₂₁	Thyroid	Maximum Likelihood Estimation-based MIL	Private Dataset: 908 Images	AUC: 0.87
Others	Schwab <i>et al.</i> [130] _{2020CD}	Lung	Jointly Classification and Localization	RSNA-Lung; MIMIC-CXR; Private Dataset: 1,003 Images	AUC: 0.93
	Wang <i>et al.</i> [131] _{2021CS}	Pancreas	Jointly Global-level Classification and Local-level Segmentation	Private Dataset: 800 Images	DSC: 0.6029; Sens: 0.9975

¹ For the sake of brevity, we denote references that contain more than one task in the following abbreviations: C: Classification, S: Segmentation, D: Detection.

TABLE 10
Surveyed Active Learning-based Studies in Medical Image Analysis

	Reference ^{Year}	Organ	Sampling Method	Dataset	Result
Classification	Gal <i>et al.</i> [137] ₂₀₁₇	Skin	BALD + KL-divergence	ISIC 2016	22% image input: AUC: 0.75
	Wu <i>et al.</i> [138] ₂₀₂₁	Lung	Loss Prediction Network	CC-CCII Dataset	42% Chest X-Ray input: Acc: 86.6%
	Li <i>et al.</i> [139] ₂₀₂₁	Prostate	CurriculumNet + O2U-Net	ISIC 2017; PANDA Dataset	60% input: QWK: 0.895
Segmentation	Yang <i>et al.</i> [140] ₂₀₁₇	Gland; Lymph	Cosine Similarity + Bootstrapping + FCN	GlaS 2015; Private Dataset: 80 US images	MICCAI 2015: 50% input: F1: 0.921; Private Dataset: 50% input: F1: 0.871
	Konyushkova <i>et al.</i> [141] ₂₀₁₉	Brain (Striatum; Hippocampus)	Geometric Priors + Boosted Trees	BraTS 2012; EFPL EM Dataset	MRI Data: 60% input: DSC≈0.76; EM Data: 40% input: DSC≈0.60
	Nath <i>et al.</i> [142] ₂₀₂₀	Brain	Entropy + SVGD Optimization	MSD 2018 Dataset	22.69% Hippocampus MRI input: DSC: 0.7241
	Ozdemir <i>et al.</i> [143] ₂₀₂₁	Shoulder	BNN + MMD Divergence	Private Dataset: 36 Volume of MRIs	48% MRI input: DSC≈0.85
	Zhao <i>et al.</i> [144] ₂₀₂₁	Hand; Skin	U-Net	RSNA-Bone; ISIC 2017	9 AL Iteration: DSC: 0.834
Others	Mahapatra <i>et al.</i> [145] _{2018CS}	Chest	Bayesian Neural Network + cGAN Data Augmentation	JSRT Database; ChestX-ray8	Classification: 35% input: AUC: 0.953; Segmentation: 35% input: DSC: 0.910
	Zhou <i>et al.</i> [146] _{2021CD}	Colon	Traditional Data Augmentation Entropy + Diversity	Private Dataset: 6 colonoscopy videos 38 polyp videos + 121 CTPA datasets	Classification: 4% input: AUC: 0.9204; Detection: 2.04% input: AUC: 0.9615

¹ For the sake of brevity, we denote references that contain more than one task in the following abbreviations: C: Classification, S: Segmentation, D: Detection.

TABLE 11
Surveyed Annotation-Efficient Learning Studies in Medical Image Analysis

	Reference ^{Year}	Application	Organ	Method	Dataset	Results
Tag Label	Hwang <i>et al.</i> [157] ₂₀₁₆	Detection	Lung; Breast	CAM + Self-Transfer Learning	Private Dataset: 11K X-rays; DDSM; MIAS	AP Shenzhen set: 0.872; MC set: 0.892; MIAS set: 0.326
	Gondal <i>et al.</i> [176] ₂₀₁₇	Detection	Eye	CAM	DRD; DiaretDB1	Hemorrhages SE: 0.91; FP s/I 1.5; Hard Exudates SE: 0.87; FPs/I 1.5; Soft Exudates SE: 0.89; FPs/I: 1.5; RSD SE: 0.52; FPs/I: 1.5
	Wang <i>et al.</i> [177] ₂₀₁₈	Detection	Eye	Expectation-Maximization + Low-Rank Subspace Learning	DRD; Messidor	mAP Kaggle: 0.8394; Messidor: 0.9091
	Nguyen <i>et al.</i> [178] ₂₀₁₉	Segmentation	Eye	CAM + CRF + Active Shape Model	Private Dataset: 40 MRI Images	DSC: T1w: 0.845±0.056; T2w: 0.839±0.049
	Wang <i>et al.</i> [179] ₂₀₂₀	Detection	Lung	CAM + Unsupervised Segmentation	Private Dataset: 540 CT Images	Hit Rate: 0.865
	Dubost <i>et al.</i> [158] ₂₀₂₀	Detection	brain	CAM + Regression	Private 2k MRIs	FAUC: 0.720±0.133
	Shen <i>et al.</i> [180] ₂₀₂₁	Detection	Breast	Globally-aware Multiple Instance	NYUBCS; CBIS-DDSM	DSC malignant: 0.325 ± 0.231; DSC Benign: 0.240 ± 0.175; AP malignant: 0.396 ± 0.275; AP Benign: 0.283 ± 0.24
	Fruh <i>et al.</i> [164] ₂₀₂₁	Segmentation	Body	CAM	Private Dataset: 454 PET/CT Images	DSC: 0.47
	Belharbi <i>et al.</i> [172] ₂₀₂₁	Segmentation	Colon	Active Learning + Self-training	GlaS	DSC: 0.8148 ± 0.0103
	Patel <i>et al.</i> [307] ₂₀₂₁	Segmentation	Brain; Prostate	CAM; cross-modality equivariant constraints	BraTS2013; DECATHLON	BraTS DSC: 0.594±0.119, ASSD: 10.04±5.1 DECATHLON DSC: 0.711±0.146, ASSD: 4.32±2.58
	Li <i>et al.</i> [159] ₂₀₂₁	Segmentation	Breast	CAM + Level-Set	Private dataset: 3062 BUS images	DSC: fat 0.830 ± 0.118; mammary gland 0.843 ± 0.100; muscle 0.807 ± 0.154; thorax layers 0.910 ± 0.114;
	Chikontwe <i>et al.</i> [308] ₂₀₂₂	Segmentation	Multi-Organ	CAM; Pretraining; Neural Compression	Private: 656 WSIs	DSC: 0.831 ± 0.004; IoU: 0.724 ± 0.007
	Chen <i>et al.</i> [160] ₂₀₂₂	Segmentation	prostate; Cardiac; Abdominal Organ	Causal Inference; CAM	ACDC; ProMRI; CHAOS	ProMRI DSC: 0.864±0.004; ASD: 3.86±1.20; MSD: 3.85±1.33 ACDC DSC: 0.875±0.008; ASD: 1.62±0.41; MSD: 1.17±0.24 CHAOS DSC: 0.781
	Qi <i>et al.</i> [309] ₂₀₂₂	Detection	Lung	Graph Regularization	NIH Chest X-ray	T(IoU) 0.5: 0.41; 0.7: 0.33
Point	Meng <i>et al.</i> [310] ₂₀₂₂	Detection	Eye	CAM; Attention	ADAM; PALM	ADAM Acc: 0.76; mAP: 0.83; PALM Acc: 0.75; mAP: 0.80;
	Khan <i>et al.</i> [167] ₂₀₁₉	Segmentation	Multi-organ	Confidence Map Supervision	SegTHOR	DSC Aorta: 0.9441 ± 0.0187; Esophagus 0.8983 ± 0.0416; Heart: 0.9653 ± 0.0194; Trachea 0.9124 ± 0.0427;
	Yoo <i>et al.</i> [168] ₂₀₁₉	Segmentation	Multi-organ	Sobel Filter + Pseudo Label	MoNuSeg; TNBC	DSC MoNuSeg: 0.6136±0.04; TNBC: 0.6038±0.03
	Zhao <i>et al.</i> [169] ₂₀₂₀	Segmentation	Cell	Self-/Co-/Hybrid-Training	PHC; Phase100	DSC PHC: 0.871; Phase 100: 0.811
	Tian <i>et al.</i> [171] ₂₀₂₀	Segmentation	Multi-organ	Voronoi + Cluster + Iterative training	MoNuSeg; TNBC	MoNuSeg DSC: 0.7132 ± 0.02; AJI: 0.4927 ± 0.04; TNBC DSC: 0.7413 ± 0.03; AJI 0.5509 ± 0.04
	Dorent <i>et al.</i> [166] ₂₀₂₀	Segmentation	Brain	CNN + CRF	Vestibular-Schwannoma-SEG	DSC: 0.819±0.080; HD95: 3.7±7.4; P: 0.929±0.059
	Roth <i>et al.</i> [165] ₂₀₂₁	Segmentation	Multi-organ	Random Walker + Iterative Training	BTCV; MSD; CT-ORG	DSC: MSD-spleen 0.958 ± 0.007; MO-Spleen 0.954 ± 0.027; MO-Liver 0.956 ± 0.010; MO-Pancreas 0.747 ± 0.082; MO-L Kidney 0.913 ± 0.013; MO-Gallbladder 0.702 ± 0.184
	Lin <i>et al.</i> [173] ₂₀₂₂	Segmentation	Multi-organ	Co-/Self-Training	MoNuSeg; CPM	MoNuSeg DSC: 0.7441; AJI: 0.5620; CPM DSC: 0.7337; AJI: 0.5132
	Wang <i>et al.</i> [181] ₂₀₁₈	Segmentation	Body	Image-Specific Fine-Tuning	Private Dataset: 18 MRI Images; BRATS	Private DSC: 0.8937±0.0231; BRATS DSC: 0.8811±0.0609
	Lee <i>et al.</i> [182] ₂₀₂₀	Segmentation	Cell	Exponential Moving Average	MoNuSeg	DSC: 0.6408; mIoU: 0.5811
	Dorent <i>et al.</i> [189] ₂₀₂₀	Segmentation	Brain	Structured learning + Domain Adaptation	Private Dataset: 254 MRI Images	DSC: 0.933±0.040; ASSD: 0.2±0.2
	Zhang <i>et al.</i> [183] ₂₀₂₂	Segmentation	Heart	Mixup + Consistency	ACDC; MSCMRseg	ACDC DSC: 0.848; MSCMRseg DSC: 0.800
	Liu <i>et al.</i> [311] ₂₀₂₂	Segmentation	Lung	Mean Teacher	IS-COVID; CC-COVID	IS-COVID DSC: 0.725; CC-COVID DSC: 0.723
	Huang <i>et al.</i> [312] ₂₀₂₂	Segmentation	Lymph	Atrous Spatial Pyramid Pooling; Cosine Similarity	Private: 147 PET/CT	DSC: 0.714
Box	Rajchl <i>et al.</i> [184] ₂₀₁₆	Segmentation	Brain; Lung	DenseCRF	Private Dataset: 55 MRI Images	Brain DSC: 0.941±0.041; Lung DSC: 0.829±0.100
	Xiong <i>et al.</i> [313] ₂₀₂₂	Segmentation	Eye	Bayesian U-Net; Expectation-Maximization	DRISHTI-GS; RIM-ONE; REFUGE	DRISHTI-GS DSC: 0.9436; RIM-ONE DSC: 0.8756 REFUGE validation DSC: 0.903; test DSC: 0.8963
	Wang <i>et al.</i> [185] ₂₀₂₂	Segmentation	lymph; Lung; Skin	RECIST measurement propagation algorithm; RECIST Loss; RECIST3D Loss	TCIA; LIDC-IDRI; HAM10000;	TCIA ASSD: 0.866; HD95: 3.263; DSC: 0.785 TCIA ASSD: 0.990; HD95: 3.628; DSC: 0.753 HAM10000 ASSD: 0.314; HD95: 1.299; DSC: 0.832
	Mahani <i>et al.</i> [314] ₂₀₂₂	Segmentation	Skin	CRF loss	ISIC 2018	DSC: 0.823±0.16; P: 0.821±0.17; R: 0.866±0.19
	Gao <i>et al.</i> [303] ₂₀₂₂	Segmentation	Cardiac	Multi-angle Projection Reconstruction loss	ACDC	10% data DSC: 0.760±0.009; HD: 16.41±1.71; ASSD: 4.46±0.61
	Li <i>et al.</i> [315] ₂₀₂₂	Segmentation	Breast	Box-supervised instance-aware head; Pseudo-mask-supervised semantic head	TUPAC16; MITOS12; MITOS14; MIDOG	TUPAC16 P: 0.787; R: 0.778; F1: 0.782; MITOS12 P: 0.810; R: 0.842; F1: 0.825; MITOS14 P: 0.581; R: 0.691; F1: 0.631; MIDOG P: 0.747; R: 0.854; F1: 0.797;
	Cai <i>et al.</i> [316] ₂₀₂₂	Segmentation	Brain; Prostate	Channel & Spatial Attention; Confidence Ranking Loss	MSD; PROMISE12	MSD DSC: 0.774; HD95: 6.34; PROMISE12 DSC: 0.869; HD95: 1.41;

REFERENCES

- [1] H. Yu, L. T. Yang, Q. Zhang, D. Armstrong, and M. J. Deen, "Convolutional neural networks for medical image analysis: state-of-the-art, comparisons, improvement and perspectives," *Neurocomputing*, vol. 444, pp. 92–110, 2021.
- [2] Z. Lu and J. Chen, "National pathology quality report in 2019," *Chinese J. Pathol.*, vol. 49, no. 7, pp. 667–669, 2020.
- [3] V. Cheplygina, M. de Bruijne, and J. P. Pluim, "Not-so-supervised: a survey of semi-supervised, multi-instance, and transfer learning in medical image analysis," *Med. Image Anal.*, vol. 54, pp. 280–296, 2019.
- [4] S. Budd, E. C. Robinson, and B. Kainz, "A survey on active learning and human-in-the-loop deep learning for medical image analysis," *Med. Image Anal.*, vol. 71, p. 102062, 2021.
- [5] L. Jing and Y. Tian, "Self-supervised visual feature learning with deep neural networks: A survey," *IEEE Trans. Pattern Anal. Mach. Intell.*, vol. 43, no. 11, pp. 4037–4058, 2020.
- [6] A. Madani, M. Moradi, A. Karargyris, and T. Syeda-Mahmood, "Semi-supervised learning with generative adversarial networks for chest x-ray classification with ability of data domain adaptation," in *Proc. IEEE Int. Symp. Biomed. Imaging*. IEEE, 2018, pp. 1038–1042.
- [7] A. Diaz-Pinto, A. Colomer, V. Naranjo, S. Morales, Y. Xu, and A. F. Frangi, "Retinal image synthesis and semi-supervised learning for glaucoma assessment," *IEEE Trans. Med. Imaging*, vol. 38, no. 9, pp. 2211–2218, 2019.
- [8] X. Shi, H. Su, F. Xing, Y. Liang, G. Qu, and L. Yang, "Graph temporal ensembling based semi-supervised convolutional neural network with noisy labels for histopathology image analysis," *Med. Image Anal.*, vol. 60, p. 101624, 2020.
- [9] G. Yu, K. Sun, C. Xu, X.-H. Shi, C. Wu, T. Xie, R.-Q. Meng, X.-H. Meng, K.-S. Wang, H.-M. Xiao *et al.*, "Accurate recognition of colorectal cancer with semi-supervised deep learning on pathological images," *Nat. Commun.*, vol. 12, no. 1, pp. 1–13, 2021.
- [10] X. Wang, H. Chen, H. Xiang, H. Lin, X. Lin, and P.-A. Heng, "Deep virtual adversarial self-training with consistency regularization for semi-supervised medical image classification," *Med. Image Anal.*, vol. 70, p. 102010, 2021.
- [11] F. Liu, Y. Tian, Y. Chen, Y. Liu, V. Belagiannis, and G. Carneiro, "Acpl: Anti-curriculum pseudo-labelling for semi-supervised medical image classification," in *Proc. IEEE Conf. Comput. Vis. Pattern Recogn.*, 2022, pp. 20 697–20 706.
- [12] W. Zhang, L. Zhu, J. Hallinan, S. Zhang, A. Makmur, Q. Cai, and B. C. Ooi, "Boostmis: Boosting medical image semi-supervised learning with adaptive pseudo labeling and informative active annotation," in *Proc. IEEE Conf. Comput. Vis. Pattern Recogn.*, 2022, pp. 20 666–20 676.
- [13] W. Bai, O. Oktay, M. Sinclair, H. Suzuki, M. Rajchl, G. Tarroni, B. Glocker, A. King, P. M. Matthews, and D. Rueckert, "Semi-supervised learning for network-based cardiac mr image segmentation," in *Proc. Int. Conf. Med. Image Comput. Comput.-Assisted Intervention*. Springer, 2017, pp. 253–260.
- [14] X. Li, L. Yu, H. Chen, C.-W. Fu, and P.-A. Heng, "Semi-supervised skin lesion segmentation via transformation consistent self-ensembling model," *arXiv preprint arXiv:1808.03887*, 2018.
- [15] D. Nie, Y. Gao, L. Wang, and D. Shen, "Asdnet: attention based semi-supervised deep networks for medical image segmentation," in *Proc. Int. Conf. Med. Image Comput. Comput.-Assisted Intervention*. Springer, 2018, pp. 370–378.
- [16] L. Yu, S. Wang, X. Li, C.-W. Fu, and P.-A. Heng, "Uncertainty-aware self-ensembling model for semi-supervised 3d left atrium segmentation," in *Proc. Int. Conf. Med. Image Comput. Comput.-Assisted Intervention*. Springer, 2019, pp. 605–613.
- [17] Y. Zhou, Y. Wang, P. Tang, S. Bai, W. Shen, E. Fishman, and A. Yuille, "Semi-supervised 3d abdominal multi-organ segmentation via deep multi-planar co-training," in *IEEE Winter Conf. Appl. Comput.*. IEEE, 2019, pp. 121–140.
- [18] X. Li, L. Yu, H. Chen, C.-W. Fu, L. Xing, and P.-A. Heng, "Transformation-consistent self-ensembling model for semi-supervised medical image segmentation," *IEEE Trans. Neural Networks Learn. Syst.*, vol. 32, no. 2, pp. 523–534, 2020.
- [19] Q. Liu, L. Yu, L. Luo, Q. Dou, and P. A. Heng, "Semi-supervised medical image classification with relation-driven self-ensembling model," *IEEE Trans. Med. Imaging*, vol. 39, no. 11, pp. 3429–3440, 2020.
- [20] S. Li, C. Zhang, and X. He, "Shape-aware semi-supervised 3d semantic segmentation for medical images," in *Proc. Int. Conf. Med. Image Comput. Comput.-Assisted Intervention*. Springer, 2020, pp. 552–561.
- [21] D.-P. Fan, T. Zhou, G.-P. Ji, Y. Zhou, G. Chen, H. Fu, J. Shen, and L. Shao, "Inf-net: Automatic covid-19 lung infection segmentation from ct images," *IEEE Trans. Med. Imaging*, vol. 39, no. 8, pp. 2626–2637, 2020.
- [22] K. Chaitanya, N. Karani, C. F. Baumgartner, E. Erdil, A. Becker, O. Donati, and E. Konukoglu, "Semi-supervised task-driven data augmentation for medical image segmentation," *Med. Image Anal.*, vol. 68, p. 101934, 2021.
- [23] X. Luo, W. Liao, J. Chen, T. Song, Y. Chen, S. Zhang, N. Chen, G. Wang, and S. Zhang, "Efficient semi-supervised gross target volume of nasopharyngeal carcinoma segmentation via uncertainty rectified pyramid consistency," in *Proc. Int. Conf. Med. Image Comput. Comput.-Assisted Intervention*. Springer, 2021, pp. 318–329.
- [24] X. Luo, J. Chen, T. Song, and G. Wang, "Semi-supervised medical image segmentation through dual-task consistency," in *AAAI Conf. Artif. Intell.*, vol. 35, no. 10, 2021, pp. 8801–8809.
- [25] D. Li, J. Yang, K. Kreis, A. Torralba, and S. Fidler, "Semantic segmentation with generative models: Semi-supervised learning and strong out-of-domain generalization," in *Proc. IEEE Conf. Comput. Vis. Pattern Recogn.*, 2021, pp. 8300–8311.
- [26] C. You, Y. Zhou, R. Zhao, L. Staib, and J. S. Duncan, "Simcvt: Simple contrastive voxel-wise representation distillation for semi-supervised medical image segmentation," *IEEE Trans. Med. Imaging*, 2022.
- [27] K. Wang, B. Zhan, C. Zu, X. Wu, J. Zhou, L. Zhou, and Y. Wang, "Semi-supervised medical image segmentation via a tripled-uncertainty guided mean teacher model with contrastive learning," *Med. Image Anal.*, vol. 79, p. 102447, 2022.
- [28] Y. Wu, Z. Ge, D. Zhang, M. Xu, L. Zhang, Y. Xia, and J. Cai, "Mutual consistency learning for semi-supervised medical image segmentation," *Med. Image Anal.*, vol. 81, p. 102530, 2022.
- [29] X. Luo, M. Hu, T. Song, G. Wang, and S. Zhang, "Semi-supervised medical image segmentation via cross teaching between cnn and transformer," in *Proc. Int. Conf. Medical Imaging Deep Learn.*. PMLR, 2022, pp. 820–833.
- [30] D. Wang, Y. Zhang, K. Zhang, and L. Wang, "Focalmix: Semi-supervised learning for 3d medical image detection," in *Proc. IEEE Conf. Comput. Vis. Pattern Recogn.*, 2020, pp. 3951–3960.
- [31] H.-Y. Zhou, C. Wang, H. Li, G. Wang, S. Zhang, W. Li, and Y. Yu, "Ssmc: semi-supervised medical image detection with adaptive consistency and heterogeneous perturbation," *Med. Image Anal.*, vol. 72, p. 102117, 2021.
- [32] Y. Grandvalet and Y. Bengio, "Semi-supervised learning by entropy minimization," *Proc. Adv. Neural Inf. Process. Syst.*, vol. 17, 2004.
- [33] D.-H. Lee *et al.*, "Pseudo-label: The simple and efficient semi-supervised learning method for deep neural networks," in *Workshop on challenges in representation learning, ICML*, vol. 3, no. 2, 2013, p. 896.
- [34] G. Wang, S. Zhai, G. Lasio, B. Zhang, B. Yi, S. Chen, T. J. Macvittie, D. Metaxas, J. Zhou, and S. Zhang, "Semi-supervised segmentation of radiation-induced pulmonary fibrosis from lung ct scans with multi-scale guided dense attention," *IEEE Trans. Med. Imaging*, vol. 41, no. 3, pp. 531–542, 2021.
- [35] Y. Zhou, X. He, L. Huang, L. Liu, F. Zhu, S. Cui, and L. Shao, "Collaborative learning of semi-supervised segmentation and classification for medical images," in *Proc. IEEE Conf. Comput. Vis. Pattern Recogn.*, 2019, pp. 2079–2088.
- [36] H. Qu, P. Wu, Q. Huang, J. Yi, Z. Yan, K. Li, G. M. Riedlinger, S. De, S. Zhang, and D. N. Metaxas, "Weakly supervised deep nuclei segmentation using partial points annotation in histopathology images," *IEEE Trans. Med. Imaging*, vol. 39, no. 11, pp. 3655–3666, 2020.
- [37] X. Yang, Z. Song, I. King, and Z. Xu, "A survey on deep semi-supervised learning," *arXiv preprint arXiv:2103.00550*, 2021.
- [38] Z.-H. Zhou and M. Li, "Tri-training: Exploiting unlabeled data using three classifiers," *IEEE Transactions on knowledge and Data Engineering*, vol. 17, no. 11, pp. 1529–1541, 2005.
- [39] W. Dong-Dong Chen and Z.-H. Wei Gao, "Tri-net for semi-supervised deep learning," in *Proceedings of twenty-seventh international joint conference on artificial intelligence*, 2018, pp. 2014–2020.

- [40] Y.-X. Zhao, Y.-M. Zhang, M. Song, and C.-L. Liu, "Multi-view semi-supervised 3d whole brain segmentation with a self-ensemble network," in *Proc. Int. Conf. Med. Image Comput. Comput.-Assisted Intervention*. Springer, 2019, pp. 256–265.
- [41] Y. Xia, D. Yang, Z. Yu, F. Liu, J. Cai, L. Yu, Z. Zhu, D. Xu, A. Yuille, and H. Roth, "Uncertainty-aware multi-view co-training for semi-supervised medical image segmentation and domain adaptation," *Med. Image Anal.*, vol. 65, p. 101766, 2020.
- [42] P. Wang, J. Peng, M. Pedersoli, Y. Zhou, C. Zhang, and C. Desrosiers, "Self-paced and self-consistent co-training for semi-supervised image segmentation," *Med. Image Anal.*, vol. 73, p. 102146, 2021.
- [43] K. Fang and W.-J. Li, "Dmnet: difference minimization network for semi-supervised segmentation in medical images," in *Proc. Int. Conf. Med. Image Comput. Comput.-Assisted Intervention*. Springer, 2020, pp. 532–541.
- [44] I. Goodfellow, J. Pouget-Abadie, M. Mirza, B. Xu, D. Warde-Farley, S. Ozair, A. Courville, and Y. Bengio, "Generative adversarial nets," *Proc. Adv. Neural Inf. Process. Syst.*, vol. 27, 2014.
- [45] J. Hou, X. Ding, and J. D. Deng, "Semi-supervised semantic segmentation of vessel images using leaking perturbations," in *Proc. IEEE Winter Conf. App. Comput. Vis.*, 2022, pp. 2625–2634.
- [46] S. A. Kamran, K. F. Hossain, A. Tavakkoli, S. L. Zuckerbrod, and S. A. Baker, "Vtgan: Semi-supervised retinal image synthesis and disease prediction using vision transformers," in *Proc. IEEE Conf. Comput. Vis. Pattern Recogn.*, 2021, pp. 3235–3245.
- [47] A. Odena, "Semi-supervised learning with generative adversarial networks," *arXiv preprint arXiv:1606.01583*, 2016.
- [48] D. P. Kingma and M. Welling, "Auto-encoding variational bayes," *arXiv preprint arXiv:1312.6114*, 2013.
- [49] S. Sedai, D. Mahapatra, S. Hewavitharanage, S. Maetschke, and R. Garnavi, "Semi-supervised segmentation of optic cup in retinal fundus images using variational autoencoder," in *Proc. Int. Conf. Med. Image Comput. Comput.-Assisted Intervention*. Springer, 2017, pp. 75–82.
- [50] J. Wang and T. Lukasiewicz, "Rethinking bayesian deep learning methods for semi-supervised volumetric medical image segmentation," in *Proc. IEEE Conf. Comput. Vis. Pattern Recogn.*, 2022, pp. 182–190.
- [51] M. Sajjadi, M. Javanmardi, and T. Tasdizen, "Regularization with stochastic transformations and perturbations for deep semi-supervised learning," *Proc. Adv. Neural Inf. Process. Syst.*, vol. 29, 2016.
- [52] G. Bortsova, F. Dubost, L. Hogeweg, I. Katramados, and M. d. Bruijne, "Semi-supervised medical image segmentation via learning consistency under transformations," in *Proc. Int. Conf. Med. Image Comput. Comput.-Assisted Intervention*. Springer, 2019, pp. 810–818.
- [53] S. Laine and T. Aila, "Temporal ensembling for semi-supervised learning," *arXiv preprint arXiv:1610.02242*, 2016.
- [54] X. Cao, H. Chen, Y. Li, Y. Peng, S. Wang, and L. Cheng, "Uncertainty aware temporal-ensembling model for semi-supervised abus mass segmentation," *IEEE Trans. Med. Imaging*, vol. 40, no. 1, pp. 431–443, 2020.
- [55] P. K. Gyawali, Z. Li, S. Ghimire, and L. Wang, "Semi-supervised learning by disentangling and self-ensembling over stochastic latent space," in *Proc. Int. Conf. Med. Image Comput. Comput.-Assisted Intervention*. Springer, 2019, pp. 766–774.
- [56] L. Luo, L. Yu, H. Chen, Q. Liu, X. Wang, J. Xu, and P.-A. Heng, "Deep mining external imperfect data for chest x-ray disease screening," *TMI*, vol. 39, no. 11, pp. 3583–3594, 2020.
- [57] A. Tarvainen and H. Valpola, "Mean teachers are better role models: Weight-averaged consistency targets improve semi-supervised deep learning results," *Proc. Adv. Neural Inf. Process. Syst.*, vol. 30, 2017.
- [58] Y. Wang, Y. Zhang, J. Tian, C. Zhong, Z. Shi, Y. Zhang, and Z. He, "Double-uncertainty weighted method for semi-supervised learning," in *Proc. Int. Conf. Med. Image Comput. Comput.-Assisted Intervention*. Springer, 2020, pp. 542–551.
- [59] H. Zhang, M. Cisse, Y. N. Dauphin, and D. Lopez-Paz, "mixup: Beyond empirical risk minimization," *arXiv preprint arXiv:1710.09412*, 2017.
- [60] P. K. Gyawali, S. Ghimire, P. Bajracharya, Z. Li, and L. Wang, "Semi-supervised medical image classification with global latent mixing," in *Proc. Int. Conf. Med. Image Comput. Comput.-Assisted Intervention*. Springer, 2020, pp. 604–613.
- [61] D. Berthelot, N. Carlini, I. Goodfellow, N. Papernot, A. Oliver, and C. A. Raffel, "Mixmatch: A holistic approach to semi-supervised learning," *Proc. Adv. Neural Inf. Process. Syst.*, vol. 32, 2019.
- [62] X. Li, M. Jia, M. T. Islam, L. Yu, and L. Xing, "Self-supervised feature learning via exploiting multi-modal data for retinal disease diagnosis," *IEEE Trans. Med. Imaging*, vol. 39, no. 12, pp. 4023–4033, 2020.
- [63] N. A. Koohbanani, B. Unnikrishnan, S. A. Khurram, P. Krishnaswamy, and N. Rajpoot, "Self-path: Self-supervision for classification of pathology images with limited annotations," *IEEE Trans. Med. Imaging*, vol. 40, no. 10, pp. 2845–2856, 2021.
- [64] S. Azizi, B. Mustafa, F. Ryan, Z. Beaver, J. Freyberg, J. Deaton, A. Loh, A. Karthikesalingam, S. Kornblith, T. Chen *et al.*, "Big self-supervised models advance medical image classification," in *Proc. IEEE Conf. Comput. Vis. Pattern Recogn.*, 2021, pp. 3478–3488.
- [65] E. Tiu, E. Talias, P. Patel, C. P. Langlotz, A. Y. Ng, and P. Rajpurkar, "Expert-level detection of pathologies from unannotated chest x-ray images via self-supervised learning," *Nat. Biomed. Eng.*, pp. 1–8, 2022.
- [66] R. J. Chen, C. Chen, Y. Li, T. Y. Chen, A. D. Trister, R. G. Krishnan, and F. Mahmood, "Scaling vision transformers to gigapixel images via hierarchical self-supervised learning," in *Proc. IEEE Conf. Comput. Vis. Pattern Recogn.*, 2022, pp. 16 144–16 155.
- [67] D. Mahapatra, Z. Ge, and M. Reyes, "Self-supervised generalized zero shot learning for medical image classification using novel interpretable saliency maps," *IEEE Trans. Med. Imaging*, 2022.
- [68] Á. S. Hervella, J. Rouco, J. Novo, and M. Ortega, "Retinal image understanding emerges from self-supervised multimodal reconstruction," in *Proc. Int. Conf. Med. Image Comput. Comput.-Assisted Intervention*. Springer, 2018, pp. 321–328.
- [69] H. Spitzer, K. Kiwitz, K. Amunts, S. Harmeling, and T. Dickscheid, "Improving cytoarchitectonic segmentation of human brain areas with self-supervised siamese networks," in *Proc. Int. Conf. Med. Image Comput. Comput.-Assisted Intervention*. Springer, 2018, pp. 663–671.
- [70] W. Bai, C. Chen, G. Tarroni, J. Duan, F. Guitton, S. E. Petersen, Y. Guo, P. M. Matthews, and D. Rueckert, "Self-supervised learning for cardiac mr image segmentation by anatomical position prediction," in *Proc. Int. Conf. Med. Image Comput. Comput.-Assisted Intervention*. Springer, 2019, pp. 541–549.
- [71] M. Sahasrabudhe, S. Christodoulidis, R. Salgado, S. Michiels, S. Loi, F. André, N. Paragios, and M. Vakalopoulou, "Self-supervised nuclei segmentation in histopathological images using attention," in *Proc. Int. Conf. Med. Image Comput. Comput.-Assisted Intervention*. Springer, 2020, pp. 393–402.
- [72] X. Tao, Y. Li, W. Zhou, K. Ma, and Y. Zheng, "Revisiting rubik's cube: self-supervised learning with volume-wise transformation for 3d medical image segmentation," in *Proc. Int. Conf. Med. Image Comput. Comput.-Assisted Intervention*. Springer, 2020, pp. 238–248.
- [73] Q. Lu, Y. Li, and C. Ye, "Volumetric white matter tract segmentation with nested self-supervised learning using sequential pretext tasks," *Med. Image Anal.*, vol. 72, p. 102094, 2021.
- [74] Y. Tang, D. Yang, W. Li, H. R. Roth, B. Landman, D. Xu, V. Nath, and A. Hatamizadeh, "Self-supervised pre-training of swin transformers for 3d med. image anal." in *Proc. IEEE Conf. Comput. Vis. Pattern Recogn.*, 2022, pp. 20 730–20 740.
- [75] C. Abbet, I. Zlobec, B. Bozorgtabar, and J.-P. Thiran, "Divide-and-rule: self-supervised learning for survival analysis in colorectal cancer," in *Proc. Int. Conf. Med. Image Comput. Comput.-Assisted Intervention*. Springer, 2020, pp. 480–489.
- [76] C. L. Srinidhi, S. W. Kim, F.-D. Chen, and A. L. Martel, "Self-supervised driven consistency training for annotation efficient histopathology image analysis," *Med. Image Anal.*, vol. 75, p. 102256, 2022.
- [77] X. Zhuang, Y. Li, Y. Hu, K. Ma, Y. Yang, and Y. Zheng, "Self-supervised feature learning for 3d medical images by playing a rubik's cube," in *Proc. Int. Conf. Med. Image Comput. Comput.-Assisted Intervention*. Springer, 2019, pp. 420–428.
- [78] L. Chen, P. Bentley, K. Mori, K. Misawa, M. Fujiwara, and D. Rueckert, "Self-supervised learning for medical image analysis using image context restoration," *Med. Image Anal.*, vol. 58, p. 101539, 2019.
- [79] C. Zhao, B. E. Dewey, D. L. Pham, P. A. Calabresi, D. S. Reich, and J. L. Prince, "Smore: a self-supervised anti-aliasing and super-

- resolution algorithm for mri using deep learning," *IEEE Trans. Med. Imaging*, vol. 40, no. 3, pp. 805–817, 2020.
- [80] M. Li, W. Hsu, X. Xie, J. Cong, and W. Gao, "Sacnn: Self-attention convolutional neural network for low-dose ct denoising with self-supervised perceptual loss network," *IEEE Trans. Med. Imaging*, vol. 39, no. 7, pp. 2289–2301, 2020.
- [81] B. Cao, H. Zhang, N. Wang, X. Gao, and D. Shen, "Auto-gan: self-supervised collaborative learning for medical image synthesis," in *AAAI Conf. Artif. Intell.*, vol. 34, no. 07, 2020, pp. 10 486–10 493.
- [82] F. Haghighi, M. R. Hosseinzadeh Taher, Z. Zhou, M. B. Gotway, and J. Liang, "Learning semantics-enriched representation via self-discovery, self-classification, and self-restoration," in *Proc. Int. Conf. Med. Image Comput. Comput.-Assisted Intervention*. Springer, 2020, pp. 137–147.
- [83] A. Taleb, W. Loetzsch, N. Danz, J. Severin, T. Gaertner, B. Bergner, and C. Lippert, "3d self-supervised methods for medical imaging," *Proc. Adv. Neural Inf. Process. Syst.*, vol. 33, pp. 18 158–18 172, 2020.
- [84] B. Li, A. Keikhosravi, A. G. Loeffler, and K. W. Eliceiri, "Single image super-resolution for whole slide image using convolutional neural networks and self-supervised color normalization," *Med. Image Anal.*, vol. 68, p. 101938, 2021.
- [85] X. Wang, S. Yang, J. Zhang, M. Wang, J. Zhang, J. Huang, W. Yang, and X. Han, "Transpath: Transformer-based self-supervised learning for histopathological image classification," in *Proc. Int. Conf. Med. Image Comput. Comput.-Assisted Intervention*. Springer, 2021, pp. 186–195.
- [86] H.-Y. Zhou, C. Lu, S. Yang, X. Han, and Y. Yu, "Preservational learning improves self-supervised medical image models by reconstructing diverse contexts," in *Proc. IEEE Conf. Comput. Vis. Pattern Recogn.*, 2021, pp. 3499–3509.
- [87] K. Yan, J. Cai, D. Jin, S. Miao, D. Guo, A. P. Harrison, Y. Tang, J. Xiao, J. Lu, and L. Lu, "Sam: Self-supervised learning of pixel-wise anatomical embeddings in radiological images," *IEEE Trans. Med. Imaging*, 2022.
- [88] Y. Cai, H. Chen, X. Yang, Y. Zhou, and K.-T. Cheng, "Dual-distribution discrepancy with self-supervised refinement for anomaly detection in medical images," *arXiv preprint arXiv:2210.04227*, 2022.
- [89] F. Haghighi, M. R. H. Taher, M. B. Gotway, and J. Liang, "Dira: Discriminative, restorative, and adversarial learning for self-supervised medical image analysis," in *Proc. IEEE Conf. Comput. Vis. Pattern Recogn.*, 2022, pp. 20 824–20 834.
- [90] H. Zhao, Y. Li, N. He, K. Ma, L. Fang, H. Li, and Y. Zheng, "Anomaly detection for medical images using self-supervised and translation-consistent features," *IEEE Trans. Med. Imaging*, vol. 40, no. 12, pp. 3641–3651, 2021.
- [91] X. Li, X. Hu, X. Qi, L. Yu, W. Zhao, P.-A. Heng, and L. Xing, "Rotation-oriented collaborative self-supervised learning for retinal disease diagnosis," *IEEE Trans. Med. Imaging*, vol. 40, no. 9, pp. 2284–2294, 2021.
- [92] H. Freeman and L. Garder, "Apictorial jigsaw puzzles: The computer solution of a problem in pattern recognition," *IEEE Transactions on Electronic Computers*, no. 2, pp. 118–127, 1964.
- [93] R. E. Korf, "Macro-operators: A weak method for learning," *Artif. Intell.*, vol. 26, no. 1, pp. 35–77, 1985.
- [94] A. Taleb, C. Lippert, T. Klein, and M. Nabi, "Multimodal self-supervised learning for medical image analysis," in *International Conference on Information Processing in Medical Imaging*. Springer, 2021, pp. 661–673.
- [95] S. Graham, D. Epstein, and N. Rajpoot, "Dense steerable filter cnns for exploiting rotational symmetry in histology images," *IEEE Trans. Med. Imaging*, vol. 39, no. 12, pp. 4124–4136, 2020.
- [96] T. Chen, S. Kornblith, M. Norouzi, and G. Hinton, "A simple framework for contrastive learning of visual representations," in *Proc. Int. Conf. Mach. Learn.*. PMLR, 2020, pp. 1597–1607.
- [97] J.-B. Grill, F. Strub, F. Althé, C. Tallec, P. Richemond, E. Buchatskaya, C. Doersch, B. Avila Pires, Z. Guo, M. Gheshlaghi Azar *et al.*, "Bootstrap your own latent-a new approach to self-supervised learning," *Proc. Adv. Neural Inf. Process. Syst.*, vol. 33, pp. 21 271–21 284, 2020.
- [98] F. C. Ghesu, B. Georgescu, A. Mansoor, Y. Yoo, D. Neumann, P. Patel, R. Vishwanath, J. M. Balter, Y. Cao, S. Grbic *et al.*, "Self-supervised learning from 100 million medical images," *arXiv preprint arXiv:2201.01283*, 2022.
- [99] A. v. d. Oord, Y. Li, and O. Vinyals, "Representation learning with contrastive predictive coding," *arXiv preprint arXiv:1807.03748*, 2018.
- [100] P. Yang, X. Yin, H. Lu, Z. Hu, X. Zhang, R. Jiang, and H. Lv, "Cs-co: A hybrid self-supervised visual representation learning method for h&e-stained histopathological images," *Med. Image Anal.*, vol. 81, p. 102539, 2022.
- [101] H.-Y. Zhou, C. Lian, L. Wang, and Y. Yu, "Advancing radiograph representation learning with masked record modeling," *arXiv preprint arXiv:2301.13155*, 2023.
- [102] H.-Y. Zhou, X. Chen, Y. Zhang, R. Luo, L. Wang, and Y. Yu, "Generalized radiograph representation learning via cross-supervision between images and free-text radiology reports," *Nat. Mach. Intell.*, vol. 4, no. 1, pp. 32–40, 2022.
- [103] S. Manivannan, C. Cobb, S. Burgess, and E. Trucco, "Subcategory classifiers for multiple-instance learning and its application to retinal nerve fiber layer visibility classification," *IEEE Trans. Med. Imaging*, vol. 36, no. 5, pp. 1140–1150, 2017.
- [104] M. Ilse, J. Tomczak, and M. Welling, "Attention-based deep multiple instance learning," in *Proc. Int. Conf. Mach. Learn.*. PMLR, 2018, pp. 2127–2136.
- [105] H. D. Couture, J. S. Marron, C. M. Perou, M. A. Troester, and M. Niethammer, "Multiple instance learning for heterogeneous images: Training a cnn for histopathology," in *Proc. Int. Conf. Med. Image Comput. Comput.-Assisted Intervention*. Springer, 2018, pp. 254–262.
- [106] M. Liu, J. Zhang, E. Adeli, and D. Shen, "Landmark-based deep multi-instance learning for brain disease diagnosis," *Med. Image Anal.*, vol. 43, pp. 157–168, 2018.
- [107] G. Campanella, M. G. Hanna, L. Geneslaw, A. Miraflor, V. Werneck Krauss Silva, K. J. Busam, E. Brogi, V. E. Reuter, D. S. Klimstra, and T. J. Fuchs, "Clinical-grade computational pathology using weakly supervised deep learning on whole slide images," *Nat. Med.*, vol. 25, no. 8, pp. 1301–1309, 2019.
- [108] S. Wang, Y. Zhu, L. Yu, H. Chen, H. Lin, X. Wan, X. Fan, and P.-A. Heng, "Rmdl: Recalibrated multi-instance deep learning for whole slide gastric image classification," *Med. Image Anal.*, vol. 58, p. 101549, 2019.
- [109] J. Yao, X. Zhu, and J. Huang, "Deep multi-instance learning for survival prediction from whole slide images," in *Proc. Int. Conf. Med. Image Comput. Comput.-Assisted Intervention*. Springer, 2019, pp. 496–504.
- [110] X. Wang, F. Tang, H. Chen, L. Luo, Z. Tang, A.-R. Ran, C. Y. Cheung, and P.-A. Heng, "Ud-mil: uncertainty-driven deep multiple instance learning for oct image classification," *IEEE J. Biomed. Health. Inf.*, vol. 24, no. 12, pp. 3431–3442, 2020.
- [111] Y. Zhao, F. Yang, Y. Fang, H. Liu, N. Zhou, J. Zhang, J. Sun, S. Yang, B. Menze, X. Fan *et al.*, "Predicting lymph node metastasis using histopathological images based on multiple instance learning with deep graph convolution," in *Proc. IEEE Conf. Comput. Vis. Pattern Recogn.*, 2020, pp. 4837–4846.
- [112] P. Chikontwe, M. Kim, S. J. Nam, H. Go, and S. H. Park, "Multiple instance learning with center embeddings for histopathology classification," in *Proc. Int. Conf. Med. Image Comput. Comput.-Assisted Intervention*. Springer, 2020, pp. 519–528.
- [113] A. Raju, J. Yao, M. M. Haq, J. Jonnagaddala, and J. Huang, "Graph attention multi-instance learning for accurate colorectal cancer staging," in *Proc. Int. Conf. Med. Image Comput. Comput.-Assisted Intervention*. Springer, 2020, pp. 529–539.
- [114] Z. Han, B. Wei, Y. Hong, T. Li, J. Cong, X. Zhu, H. Wei, and W. Zhang, "Accurate screening of covid-19 using attention-based deep 3d multiple instance learning," *IEEE Trans. Med. Imaging*, vol. 39, no. 8, pp. 2584–2594, 2020.
- [115] J. Yao, X. Zhu, J. Jonnagaddala, N. Hawkins, and J. Huang, "Whole slide images based cancer survival prediction using attention guided deep multiple instance learning networks," *Med. Image Anal.*, vol. 65, p. 101789, 2020.
- [116] N. Hashimoto, D. Fukushima, R. Koga, Y. Takagi, K. Ko, K. Kohno, M. Nakaguro, S. Nakamura, H. Hontani, and I. Takeuchi, "Multi-scale domain-adversarial multiple-instance cnn for cancer subtype classification with unannotated histopathological images," in *Proc. IEEE Conf. Comput. Vis. Pattern Recogn.*, 2020, pp. 3852–3861.
- [117] Z. Shao, H. Bian, Y. Chen, Y. Wang, J. Zhang, X. Ji *et al.*, "Transmil: Transformer based correlated multiple instance learning for whole slide image classification," *Proc. Adv. Neural Inf. Process. Syst.*, vol. 34, pp. 2136–2147, 2021.

- [118] B. Li, Y. Li, and K. W. Eliceiri, "Dual-stream multiple instance learning network for whole slide image classification with self-supervised contrastive learning," in *Proc. IEEE Conf. Comput. Vis. Pattern Recogn.*, 2021, pp. 14318–14328.
- [119] Z. Li, W. Zhao, F. Shi, L. Qi, X. Xie, Y. Wei, Z. Ding, Y. Gao, S. Wu, J. Liu *et al.*, "A novel multiple instance learning framework for covid-19 severity assessment via data augmentation and self-supervised learning," *Med. Image Anal.*, vol. 69, p. 101978, 2021.
- [120] M. Y. Lu, D. F. Williamson, T. Y. Chen, R. J. Chen, M. Barbieri, and F. Mahmood, "Data-efficient and weakly supervised computational pathology on whole-slide images," *Nat. Biomed. Eng.*, vol. 5, no. 6, pp. 555–570, 2021.
- [121] Z. Wang, L. Yu, X. Ding, X. Liao, and L. Wang, "Lymph node metastasis prediction from whole slide images with transformer-guided multi-instance learning and knowledge transfer," *IEEE Trans. Med. Imaging*, 2022.
- [122] H. Zhang, Y. Meng, Y. Zhao, Y. Qiao, X. Yang, S. E. Coupland, and Y. Zheng, "Dtfd-mil: Double-tier feature distillation multiple instance learning for histopathology whole slide image classification," in *Proc. IEEE Conf. Comput. Vis. Pattern Recogn.*, 2022, pp. 18802–18812.
- [123] Y. Schirris, E. Gavves, I. Nederlof, H. M. Horlings, and J. Teuwen, "Deepsmile: Contrastive self-supervised pre-training benefits msi and hrd classification directly from h&e whole-slide images in colorectal and breast cancer," *Med. Image Anal.*, vol. 79, p. 102464, 2022.
- [124] Z. Su, T. E. Tavorola, G. Carreno-Galeano, S. J. Lee, M. N. Gurcan, and M. Niazi, "Attention2majority: Weak multiple instance learning for regenerative kidney grading on whole slide images," *Med. Image Anal.*, vol. 79, p. 102462, 2022.
- [125] Z. Zhu, L. Yu, W. Wu, R. Yu, D. Zhang, and L. Wang, "Murcl: Multi-instance reinforcement contrastive learning for whole slide image classification," *IEEE Trans. Med. Imaging*, 2022.
- [126] M. Yang, Z. Xie, Z. Wang, Y. Yuan, and J. Zhang, "Sumicl: Severity-guided multiple instance curriculum learning for histopathology image interpretable classification," *IEEE Trans. Med. Imaging*, vol. 41, no. 12, pp. 3533–3543, 2022.
- [127] Z. Jia, X. Huang, I. Eric, C. Chang, and Y. Xu, "Constrained deep weak supervision for histopathology image segmentation," *IEEE Trans. Med. Imaging*, vol. 36, no. 11, pp. 2376–2388, 2017.
- [128] G. Xu, Z. Song, Z. Sun, C. Ku, Z. Yang, C. Liu, S. Wang, J. Ma, and W. Xu, "Camel: A weakly supervised learning framework for histopathology image segmentation," in *Proc. IEEE Conf. Comput. Vis. Pattern Recogn.*, 2019, pp. 10682–10691.
- [129] D. Dov, S. Z. Kovalsky, S. Assaad, J. Cohen, D. E. Range, A. A. Pendse, R. Henao, and L. Carin, "Weakly supervised instance learning for thyroid malignancy prediction from whole slide cytopathology images," *Med. Image Anal.*, vol. 67, p. 101814, 2021.
- [130] E. Schwab, A. Gooßen, H. Deshpande, and A. Saalbach, "Localization of critical findings in chest x-ray without local annotations using multi-instance learning," in *Proc. IEEE Int. Symp. Biomed. Imaging*. IEEE, 2020, pp. 1879–1882.
- [131] Y. Wang, P. Tang, Y. Zhou, W. Shen, E. K. Fishman, and A. L. Yuille, "Learning inductive attention guidance for partially supervised pancreatic ductal adenocarcinoma prediction," *IEEE Trans. Med. Imaging*, vol. 40, no. 10, pp. 2723–2735, 2021.
- [132] C. Mercan, S. Aksoy, E. Mercan, L. G. Shapiro, D. L. Weaver, and J. G. Elmore, "Multi-instance multi-label learning for multi-class classification of whole slide breast histopathology images," *IEEE Trans. Med. Imaging*, vol. 37, no. 1, pp. 316–325, 2017.
- [133] N. Tomita, B. Abdollahi, J. Wei, B. Ren, A. Suriawinata, and S. Hassanpour, "Attention-based deep neural networks for detection of cancerous and precancerous esophagus tissue on histopathological slides," *JAMA network open*, vol. 2, no. 11, pp. e1914645–e1914645, 2019.
- [134] N. Naik, A. Madani, A. Esteva, N. S. Keskar, M. F. Press, D. Ruderman, D. B. Agus, and R. Socher, "Deep learning-enabled breast cancer hormonal receptor status determination from base-level h&e stains," *Nat. Commun.*, vol. 11, no. 1, pp. 1–8, 2020.
- [135] K. Das, S. Conjeti, A. G. Roy, J. Chatterjee, and D. Sheet, "Multiple instance learning of deep convolutional neural networks for breast histopathology whole slide classification," in *Proc. IEEE Int. Symp. Biomed. Imaging*. IEEE, 2018, pp. 578–581.
- [136] R. Tennakoon, G. Bortsova, S. Ørting, A. K. Gostar, M. M. Wille, Z. Saghir, R. Hoseinnezhad, M. de Bruijne, and A. Bab-Hadiashar, "Classification of volumetric images using multi-instance learning and extreme value theorem," *IEEE Trans. Med. Imaging*, vol. 39, no. 4, pp. 854–865, 2019.
- [137] Y. Gal, R. Islam, and Z. Ghahramani, "Deep bayesian active learning with image data," in *Proc. Int. Conf. Mach. Learn.* PMLR, 2017, pp. 1183–1192.
- [138] X. Wu, C. Chen, M. Zhong, J. Wang, and J. Shi, "Covid-al: The diagnosis of covid-19 with deep active learning," *Med. Image Anal.*, vol. 68, p. 101913, 2021.
- [139] W. Li, J. Li, Z. Wang, J. Polson, A. E. Sisk, D. P. Sajed, W. Speier, and C. W. Arnold, "Pathal: An active learning framework for histopathology image analysis," *IEEE Trans. Med. Imaging*, 2021.
- [140] L. Yang, Y. Zhang, J. Chen, S. Zhang, and D. Z. Chen, "Suggestive annotation: A deep active learning framework for biomedical image segmentation," in *Proc. Int. Conf. Med. Image Comput. Comput.-Assisted Intervention*. Springer, 2017, pp. 399–407.
- [141] K. Konyushkova, R. Sznitman, and P. Fua, "Geometry in active learning for binary and multi-class image segmentation," *Comput. Vis. Image Underst.*, vol. 182, pp. 1–16, 2019.
- [142] V. Nath, D. Yang, B. A. Landman, D. Xu, and H. R. Roth, "Diminishing uncertainty within the training pool: Active learning for medical image segmentation," *IEEE Trans. Med. Imaging*, vol. 40, no. 10, pp. 2534–2547, 2020.
- [143] F. Ozdemir, Z. Peng, P. Fuernstahl, C. Tanner, and O. Goksel, "Active learning for segmentation based on bayesian sample queries," *Knowledge-Based Systems*, vol. 214, p. 106531, 2021.
- [144] Z. Zhao, Z. Zeng, K. Xu, C. Chen, and C. Guan, "Dsal: Deeply supervised active learning from strong and weak labelers for biomedical image segmentation," *IEEE J. Biomed. Health. Inf.*, vol. 25, no. 10, pp. 3744–3751, 2021.
- [145] D. Mahapatra, B. Bozorgtabar, J.-P. Thiran, and M. Reyes, "Efficient active learning for image classification and segmentation using a sample selection and conditional generative adversarial network," in *Proc. Int. Conf. Med. Image Comput. Comput.-Assisted Intervention*. Springer, 2018, pp. 580–588.
- [146] Z. Zhou, J. Y. Shin, S. R. Gurudu, M. B. Gotway, and J. Liang, "Active, continual fine tuning of convolutional neural networks for reducing annotation efforts," *Med. Image Anal.*, vol. 71, p. 101997, 2021.
- [147] R. Achanta, A. Shaji, K. Smith, A. Lucchi, P. Fua, and S. Süsstrunk, "Slic superpixels compared to state-of-the-art superpixel methods," *IEEE Trans. Pattern Anal. Mach. Intell.*, vol. 34, no. 11, pp. 2274–2282, 2012.
- [148] H. Chen, X. Qi, L. Yu, and P.-A. Heng, "Dcan: deep contour-aware networks for accurate gland segmentation," in *Proc. IEEE Conf. Comput. Vis. Pattern Recogn.*, 2016, pp. 2487–2496.
- [149] Q. Liu, "Stein variational gradient descent as gradient flow," *Proc. Adv. Neural Inf. Process. Syst.*, vol. 30, 2017.
- [150] P. Krähenbühl and V. Koltun, "Efficient inference in fully connected crfs with gaussian edge potentials," *Proc. Adv. Neural Inf. Process. Syst.*, vol. 24, 2011.
- [151] S. Guo, W. Huang, H. Zhang, C. Zhuang, D. Dong, M. R. Scott, and D. Huang, "Curriculumnet: Weakly supervised learning from large-scale web images," in *Proc. Eur. Conf. Comput. Vis.*, 2018, pp. 135–150.
- [152] J. Huang, L. Qu, R. Jia, and B. Zhao, "O2u-net: A simple noisy label detection approach for deep neural networks," in *Proc. IEEE Conf. Comput. Vis. Pattern Recogn.*, 2019, pp. 3326–3334.
- [153] N. Houlsby, F. Huszar, Z. Ghahramani, and M. Lengyel, "Bayesian active learning for classification and preference learning," *arXiv preprint arXiv:1112.5745*, 2011.
- [154] Y. Gal and Z. Ghahramani, "Dropout as a bayesian approximation: Representing model uncertainty in deep learning," in *Proc. Int. Conf. Mach. Learn.* PMLR, 2016, pp. 1050–1059.
- [155] S. Zhao, J. Song, and S. Ermon, "Infovae: Information maximizing variational autoencoders," *arXiv preprint arXiv:1706.02262*, 2017.
- [156] B. Zhou, A. Khosla, A. Lapedriza, A. Oliva, and A. Torralba, "Learning deep features for discriminative localization," in *Proc. IEEE Conf. Comput. Vis. Pattern Recogn.*, 2016, pp. 2921–2929.
- [157] S. Hwang and H.-E. Kim, "Self-transfer learning for weakly supervised lesion localization," in *Proc. Int. Conf. Med. Image Comput. Comput.-Assisted Intervention*. Springer, 2016, pp. 239–246.
- [158] F. Dubost, H. Adams, P. Yilmaz, G. Bortsova, G. van Tulder, M. A. Ikram, W. Niessen, M. W. Vernooij, and M. de Bruijne, "Weakly supervised object detection with 2d and 3d regression neural networks," *Med. Image Anal.*, vol. 65, p. 101767, 2020.

- [159] Y. Li, Y. Liu, L. Huang, Z. Wang, and J. Luo, "Deep weakly-supervised breast tumor segmentation in ultrasound images with explicit anatomical constraints," *Med. Image Anal.*, vol. 76, p. 102315, 2022.
- [160] Z. Chen, Z. Tian, J. Zhu, C. Li, and S. Du, "C-cam: Causal cam for weakly supervised semantic segmentation on medical image," in *Proc. IEEE Conf. Comput. Vis. Pattern Recogn.*, 2022, pp. 11 676–11 685.
- [161] Y. Lin, H.-Y. Zhou, K. Ma, X. Yang, and Y. Zheng, "Seg4reg networks for automated spinal curvature estimation," in *Workshop of Proc. Int. Conf. Med. Image Comput. Comput.-Assisted Intervention*. Springer, 2019, pp. 69–74.
- [162] Y. Lin, L. Liu, K. Ma, and Y. Zheng, "Seg4reg+: Consistency learning between spine segmentation and cobb angle regression," in *Proc. Int. Conf. Med. Image Comput. Comput.-Assisted Intervention*. Springer, 2021, pp. 490–499.
- [163] D. Zhang, B. Chen, J. Chong, and S. Li, "Weakly-supervised teacher-student network for liver tumor segmentation from non-enhanced images," *Med. Image Anal.*, vol. 70, p. 102005, 2021.
- [164] M. Früh, M. Fischer, A. Schilling, S. Gatidis, and T. Hepp, "Weakly supervised segmentation of tumor lesions in pet-ct hybrid imaging," *J. Med. Imaging*, vol. 8, no. 5, p. 054003, 2021.
- [165] H. R. Roth, D. Yang, Z. Xu, X. Wang, and D. Xu, "Going to extremes: weakly supervised medical image segmentation," *Mach. Learn. Knowl. Extr.*, vol. 3, no. 2, pp. 507–524, 2021.
- [166] R. Dorent, S. Joutard, J. Shapey, A. Kujawa, M. Modat, S. Ourselin, and T. Vercauteren, "Inter extreme points geodesics for end-to-end weakly supervised image segmentation," in *Proc. Int. Conf. Med. Image Comput. Comput.-Assisted Intervention*. Springer, 2021, pp. 615–624.
- [167] S. Khan, A. H. Shahin, J. Villafruela, J. Shen, and L. Shao, "Extreme points derived confidence map as a cue for class-agnostic interactive segmentation using deep neural network," in *Proc. Int. Conf. Med. Image Comput. Comput.-Assisted Intervention*. Springer, 2019, pp. 66–73.
- [168] I. Yoo, D. Yoo, and K. Paeng, "Pseudoedgenet: Nuclei segmentation only with point annotations," in *Proc. Int. Conf. Med. Image Comput. Comput.-Assisted Intervention*. Springer, 2019, pp. 731–739.
- [169] T. Zhao and Z. Yin, "Weakly supervised cell segmentation by point annotation," *IEEE Trans. Med. Imaging*, vol. 40, no. 10, pp. 2736–2747, 2020.
- [170] H. Qu, P. Wu, Q. Huang, J. Yi, G. M. Riedlinger, S. De, and D. N. Metaxas, "Weakly supervised deep nuclei segmentation using points annotation in histopathology images," in *Proc. Int. Conf. Mach. Learn.* PMLR, 2019, pp. 390–400.
- [171] K. Tian, J. Zhang, H. Shen, K. Yan, P. Dong, J. Yao, S. Che, P. Luo, and X. Han, "Weakly-supervised nucleus segmentation based on point annotations: A coarse-to-fine self-stimulated learning strategy," in *Proc. Int. Conf. Med. Image Comput. Comput.-Assisted Intervention*. Springer, 2020, pp. 299–308.
- [172] S. Belharbi, I. Ben Ayed, L. McCaffrey, and E. Granger, "Deep active learning for joint classification & segmentation with weak annotator," in *Proc. IEEE Winter Conf. App. Comput. Vis.*, 2021, pp. 3338–3347.
- [173] Y. Lin, Z. Qu, H. Chen, Z. Gao, Y. Li, L. Xia, K. Ma, Y. Zheng, and K.-T. Cheng, "Label propagation for annotation-efficient nuclei segmentation from pathology images," *arXiv preprint arXiv:2202.08195*, 2022.
- [174] G. Valvano, A. Leo, and S. A. Tsaftaris, "Learning to segment from scribbles using multi-scale adversarial attention gates," *IEEE Trans. Med. Imaging*, vol. 40, no. 8, pp. 1990–2001, 2021.
- [175] K. Kise, A. Sato, and M. Iwata, "Segmentation of page images using the area voronoi diagram," *Comput. Vis. Image Underst.*, vol. 70, no. 3, pp. 370–382, 1998.
- [176] W. M. Gondal, J. M. Köhler, R. Grzeszick, G. A. Fink, and M. Hirsch, "Weakly-supervised localization of diabetic retinopathy lesions in retinal fundus images," in *Proc. IEEE Int. Conf. Image Process.* IEEE, 2017, pp. 2069–2073.
- [177] R. Wang, B. Chen, D. Meng, and L. Wang, "Weakly supervised lesion detection from fundus images," *IEEE Trans. Med. Imaging*, vol. 38, no. 6, pp. 1501–1512, 2018.
- [178] H.-G. Nguyen, A. Pica, J. Hrbacek, D. C. Weber, F. La Rosa, A. Schalenbourg, R. Sznitman, and M. B. Cuadra, "A novel segmentation framework for uveal melanoma in magnetic resonance imaging based on class activation maps," in *Proc. Int. Conf. Mach. Learn.* PMLR, 2019, pp. 370–379.
- [179] X. Wang, X. Deng, Q. Fu, Q. Zhou, J. Feng, H. Ma, W. Liu, and C. Zheng, "A weakly-supervised framework for covid-19 classification and lesion localization from chest ct," *IEEE Trans. Med. Imaging*, vol. 39, no. 8, pp. 2615–2625, 2020.
- [180] Y. Shen, N. Wu, J. Phang, J. Park, K. Liu, S. Tyagi, L. Heacock, S. G. Kim, L. Moy, K. Cho *et al.*, "An interpretable classifier for high-resolution breast cancer screening images utilizing weakly supervised localization," *Med. Image Anal.*, vol. 68, p. 101908, 2021.
- [181] G. Wang, W. Li, M. A. Zuluaga, R. Pratt, P. A. Patel, M. Aertsen, T. Doel, A. L. David, J. Deprest, S. Ourselin *et al.*, "Interactive medical image segmentation using deep learning with image-specific fine tuning," *IEEE Trans. Med. Imaging*, vol. 37, no. 7, pp. 1562–1573, 2018.
- [182] H. Lee and W.-K. Jeong, "Scribble2label: Scribble-supervised cell segmentation via self-generating pseudo-labels with consistency," in *Proc. Int. Conf. Med. Image Comput. Comput.-Assisted Intervention*. Springer, 2020, pp. 14–23.
- [183] K. Zhang and X. Zhuang, "Cyclemix: A holistic strategy for medical image segmentation from scribble supervision," in *Proc. IEEE Conf. Comput. Vis. Pattern Recogn.*, 2022, pp. 11 656–11 665.
- [184] M. Rajchl, M. C. Lee, O. Oktay, K. Kamnitsas, J. Passerat-Palmbach, W. Bai, M. Damodaram, M. A. Rutherford, J. V. Hajnal, B. Kainz *et al.*, "Deepcut: Object segmentation from bounding box annotations using convolutional neural networks," *IEEE Trans. Med. Imaging*, vol. 36, no. 2, pp. 674–683, 2016.
- [185] H. Wang, F. Yi, J. Wang, Z. Yi, and H. Zhang, "Recistsup: Weakly-supervised lesion volume segmentation using recist measurement," *IEEE Trans. Med. Imaging*, 2022.
- [186] N. Tajbakhsh, L. Jeyaseelan, Q. Li, J. N. Chiang, Z. Wu, and X. Ding, "Embracing imperfect datasets: A review of deep learning solutions for medical image segmentation," *Med. Image Anal.*, vol. 63, p. 101693, 2020.
- [187] Y. B. Can, K. Chaitanya, B. Mustafa, L. M. Koch, E. Konukoglu, and C. F. Baumgartner, "Learning to segment medical images with scribble-supervision alone," in *Deep Learning in Medical Image Analysis and Multimodal Learning for Clinical Decision Support*. Springer, 2018, pp. 236–244.
- [188] H. Lee and W.-K. Jeong, "Scribble2label: Scribble-supervised cell segmentation via self-generating pseudo-labels with consistency," in *Proc. Int. Conf. Med. Image Comput. Comput.-Assisted Intervention*. Springer, 2020, pp. 14–23.
- [189] R. Dorent, S. Joutard, J. Shapey, S. Bisdas, N. Kitchen, R. Bradford, S. Saeed, M. Modat, S. Ourselin, and T. Vercauteren, "Scribble-based domain adaptation via co-segmentation," in *Proc. Int. Conf. Med. Image Comput. Comput.-Assisted Intervention*. Springer, 2020, pp. 479–489.
- [190] J. Wang and B. Xia, "Accurate cup-to-disc ratio measurement with tight bounding box supervision in fundus photography," *arXiv preprint arXiv:2110.00943*, 2021.
- [191] J. wang and B. Xia, "Bounding box tightness prior for weakly supervised image segmentation," in *Proc. Int. Conf. Med. Image Comput. Comput.-Assisted Intervention*. Springer, 2021, pp. 526–536.
- [192] C.-C. Hsu, K.-J. Hsu, C.-C. Tsai, Y.-Y. Lin, and Y.-Y. Chuang, "Weakly supervised instance segmentation using the bounding box tightness prior," *Proc. Adv. Neural Inf. Process. Syst.*, vol. 32, 2019.
- [193] L. Luo, H. Chen, Y. Zhou, H. Lin, and P.-A. Heng, "Oxnet: Deep omni-supervised thoracic disease detection from chest x-rays," in *Proc. Int. Conf. Med. Image Comput. Comput.-Assisted Intervention*. Springer, 2021, pp. 537–548.
- [194] Z. Chai, H. Lin, L. Luo, P.-A. Heng, and H. Chen, "Orf-net: Deep omni-supervised rib fracture detection from chest ct scans," in *Proc. Int. Conf. Med. Image Comput. Comput.-Assisted Intervention*. Springer, 2022, pp. 238–248.
- [195] N. Rieke, J. Hancox, W. Li, F. Milletari, H. R. Roth, S. Albarqouni, S. Bakas, M. N. Galtier, B. A. Landman, K. Maier-Hein *et al.*, "The future of digital health with federated learning," *NPJ Digit. Med.*, vol. 3, no. 1, pp. 1–7, 2020.
- [196] I. Dayan, H. R. Roth, A. Zhong, A. Harouni, A. Gentili, A. Z. Abidin, A. Liu, A. B. Costa, B. J. Wood, C.-S. Tsai *et al.*, "Federated learning for predicting clinical outcomes in patients with covid-19," *Nat. Med.*, vol. 27, no. 10, pp. 1735–1743, 2021.
- [197] X. Li, Y. Gu, N. Dvornek, L. H. Staib, P. Ventola, and J. S. Duncan, "Multi-site fmri analysis using privacy-preserving federated

- learning and domain adaptation: Abide results," *Med. Image Anal.*, vol. 65, p. 101765, 2020.
- [198] M. Y. Lu, R. J. Chen, D. Kong, J. Lipkova, R. Singh, D. F. Williamson, T. Y. Chen, and F. Mahmood, "Federated learning for computational pathology on gigapixel whole slide images," *Med. Image Anal.*, vol. 76, p. 102298, 2022.
- [199] Q. Liu, H. Yang, Q. Dou, and P.-A. Heng, "Federated semi-supervised medical image classification via inter-client relation matching," in *MICCAI*. Springer, 2021, pp. 325–335.
- [200] N. Dong and I. Voiculescu, "Federated contrastive learning for decentralized unlabeled medical images," in *MICCAI*. Springer, 2021, pp. 378–387.
- [201] X. Liao, W. Li, Q. Xu, X. Wang, B. Jin, X. Zhang, Y. Wang, and Y. Zhang, "Iteratively-refined interactive 3d medical image segmentation with multi-agent reinforcement learning," in *Proc. IEEE Conf. Comput. Vis. Pattern Recogn.*, 2020, pp. 9394–9402.
- [202] C. Ma, Q. Xu, X. Wang, B. Jin, X. Zhang, Y. Wang, and Y. Zhang, "Boundary-aware supervoxel-level iteratively refined interactive 3d image segmentation with multi-agent reinforcement learning," *IEEE Trans. Med. Imaging*, vol. 40, no. 10, pp. 2563–2574, 2020.
- [203] R. Feng, X. Zheng, T. Gao, J. Chen, W. Wang, D. Z. Chen, and J. Wu, "Interactive few-shot learning: Limited supervision, better medical image segmentation," *IEEE Trans. Med. Imaging*, vol. 40, no. 10, pp. 2575–2588, 2021.
- [204] D. Al Chantj, V. G. Duque, M. Crouzier, A. Nordez, L. Lacourpaille, and D. Mateus, "Ifss-net: Interactive few-shot siamese network for faster muscle segmentation and propagation in volumetric ultrasound," *IEEE Trans. Med. Imaging*, vol. 40, no. 10, pp. 2615–2628, 2021.
- [205] D. Mahapatra, A. Poellinger, L. Shao, and M. Reyes, "Interpretability-driven sample selection using self supervised learning for disease classification and segmentation," *IEEE Trans. Med. Imaging*, vol. 40, no. 10, pp. 2548–2562, 2021.
- [206] C. Shorten and T. M. Khoshgoftaar, "A survey on image data augmentation for deep learning," *J. Big Data*, vol. 6, no. 1, pp. 1–48, 2019.
- [207] Z. Wang, Y. Lin, K.-T. T. Cheng, and X. Yang, "Semi-supervised mp-mri data synthesis with stitchlayer and auxiliary distance maximization," *Med. Image Anal.*, vol. 59, p. 101565, 2020.
- [208] Y. Lin, Z. Wang, K.-T. Cheng, and H. Chen, "Insmix: Towards realistic generative data augmentation for nuclei instance segmentation," in *Proc. Int. Conf. Med. Image Comput. Comput.-Assisted Intervention*. Springer, 2022, pp. 140–149.
- [209] I. Gulrajani, F. Ahmed, M. Arjovsky, V. Dumoulin, and A. C. Courville, "Improved training of wasserstein gans," *Proc. Adv. Neural Inf. Process. Syst.*, vol. 30, 2017.
- [210] Z. Lin, A. Khetan, G. Fanti, and S. Oh, "Pacgan: The power of two samples in generative adversarial networks," *Proc. Adv. Neural Inf. Process. Syst.*, vol. 31, 2018.
- [211] X. Yang, Y. Lin, Z. Wang, X. Li, and K.-T. Cheng, "Bi-modality medical image synthesis using semi-supervised sequential generative adversarial networks," *IEEE J. Biomed. Health. Inf.*, vol. 24, no. 3, pp. 855–865, 2019.
- [212] J. Ho, A. Jain, and P. Abbeel, "Denoising diffusion probabilistic models," *Adv. Neural Inf. Process. Syst.*, vol. 33, pp. 6840–6851, 2020.
- [213] A. Kazerouni, E. K. Aghdam, M. Heidari, R. Azad, M. Fayyaz, I. Hacıhaliloglu, and D. Merhof, "Diffusion models for medical image analysis: A comprehensive survey," *arXiv preprint arXiv:2211.07804*, 2022.
- [214] Z. Xiao, K. Kreis, and A. Vahdat, "Tackling the generative learning trilemma with denoising diffusion gans," in *Proc. Int. Conf. Learn. Represent.*, 2022.
- [215] K. Zhou, Z. Liu, Y. Qiao, T. Xiang, and C. C. Loy, "Domain generalization: A survey," *IEEE Trans. Pattern Anal. Mach. Intell.*, 2022.
- [216] H. Li, S. J. Pan, S. Wang, and A. C. Kot, "Domain generalization with adversarial feature learning," in *Proc. IEEE Conf. Comput. Vis. Pattern Recogn.*, 2018, pp. 5400–5409.
- [217] Y. Li, Y. Yang, W. Zhou, and T. Hospedales, "Feature-critic networks for heterogeneous domain generalization," in *Proc. Int. Conf. Mach. Learn.*. PMLR, 2019, pp. 3915–3924.
- [218] F. Qiao, L. Zhao, and X. Peng, "Learning to learn single domain generalization," in *Proc. IEEE Conf. Comput. Vis. Pattern Recogn.*, 2020, pp. 12 556–12 565.
- [219] H. Li, Y. Wang, R. Wan, S. Wang, T.-Q. Li, and A. Kot, "Domain generalization for medical imaging classification with linear-dependency regularization," *NIPS*, vol. 33, pp. 3118–3129, 2020.
- [220] Q. Liu, C. Chen, J. Qin, Q. Dou, and P.-A. Heng, "Feddg: Federated domain generalization on medical image segmentation via episodic learning in continuous frequency space," in *CVPR*, 2021, pp. 1013–1023.
- [221] J. Yuan, X. Ma, D. Chen, K. Kuang, F. Wu, and L. Lin, "Label-efficient domain generalization via collaborative exploration and generalization," in *Proc. ACM Int. Conf. Multimedia*, 2022, pp. 2361–2370.
- [222] D. Gut, Z. Tabor, M. Szymkowski, M. Rozynek, I. Kucybała, and W. Wojciechowski, "Benchmarking of deep architectures for segmentation of medical images," *IEEE Trans. Med. Imaging*, vol. 41, no. 11, pp. 3231–3241, 2022.
- [223] Z. Xiaojin, "Semi-supervised learning literature survey," *Computer Sciences TR*, vol. 1530, 2008.
- [224] J. E. Van Engelen and H. H. Hoos, "A survey on semi-supervised learning," *Machine Learning*, vol. 109, no. 2, pp. 373–440, 2020.
- [225] Y. Ouali, C. Hudelot, and M. Tami, "An overview of deep semi-supervised learning," *arXiv preprint arXiv:2006.05278*, 2020.
- [226] O. Chapelle, B. Scholkopf, and A. Zien, "Semi-supervised learning (chapelle, o. et al., eds.; 2006)[book reviews]," *IEEE Trans. Neural Netw.*, vol. 20, no. 3, pp. 542–542, 2009.
- [227] C. Campbell, N. Cristianini, A. Smola et al., "Query learning with large margin classifiers," in *Proc. Int. Conf. Mach. Learn.*, vol. 20, no. 0, 2000, p. 0.
- [228] A. Holub, P. Perona, and M. C. Burl, "Entropy-based active learning for object recognition," in *Proc. IEEE Conf. Comput. Vis. Pattern Recogn.*. IEEE, 2008, pp. 1–8.
- [229] B. H. Menze, A. Jakab, S. Bauer, J. Kalpathy-Cramer, K. Farahani, J. Kirby, Y. Burren, N. Porz, J. Slotboom, R. Wiest et al., "The multimodal brain tumor image segmentation benchmark (brats)," *IEEE Trans. Med. Imaging*, vol. 34, no. 10, pp. 1993–2024, 2014.
- [230] A. L. Simpson, M. Antonelli, S. Bakas, M. Bilello, K. Farahani, B. Van Ginneken, A. Kopp-Schneider, B. A. Landman, G. Litjens, B. Menze et al., "A large annotated medical image dataset for the development and evaluation of segmentation algorithms," *arXiv preprint arXiv:1902.09063*, 2019.
- [231] A. Makropoulos, E. C. Robinson, A. Schuh, R. Wright, S. Fitzgibbon, J. Bozek, S. J. Counsell, J. Steinweg, K. Vecchiato, J. Passerat-Palmbach et al., "The developing human connectome project: A minimal processing pipeline for neonatal cortical surface reconstruction," *Neuroimage*, vol. 173, pp. 88–112, 2018.
- [232] J. Shiraishi, S. Katsuragawa, J. Ikezoe, T. Matsumoto, T. Kobayashi, K.-i. Komatsu, M. Matsui, H. Fujita, Y. Kodera, and K. Doi, "Development of a digital image database for chest radiographs with and without a lung nodule: receiver operating characteristic analysis of radiologists' detection of pulmonary nodules," *AJR. Am. J. Roentgenol.*, vol. 174, no. 1, pp. 71–74, 2000.
- [233] K. Amunts, C. Lepage, L. Borgeat, H. Mohlberg, T. Dickscheid, M.-É. Rousseau, S. Bludau, P.-L. Bazin, L. B. Lewis, A.-M. Oros-Peusquens et al., "Bigbrain: an ultrahigh-resolution 3d human brain model," *Science*, vol. 340, no. 6139, pp. 1472–1475, 2013.
- [234] A. Seff, L. Lu, A. Barbu, H. Roth, H.-C. Shin, and R. M. Summers, "Leveraging mid-level semantic boundary cues for automated lymph node detection," in *Proc. Int. Conf. Med. Image Comput. Comput.-Assisted Intervention*. Springer, 2015, pp. 53–61.
- [235] K. Zhang, X. Liu, J. Shen, Z. Li, Y. Sang, X. Wu, Y. Zha, W. Liang, C. Wang, K. Wang et al., "Clinically applicable ai system for accurate diagnosis, quantitative measurements, and prognosis of covid-19 pneumonia using computed tomography," *Cell*, vol. 181, no. 6, pp. 1423–1433, 2020.
- [236] X. Wang, Y. Peng, L. Lu, Z. Lu, M. Bagheri, and R. M. Summers, "Chestx-ray8: Hospital-scale chest x-ray database and benchmarks on weakly-supervised classification and localization of common thorax diseases," in *Proc. IEEE Conf. Comput. Vis. Pattern Recogn.*, 2017, pp. 2097–2106.
- [237] D. S. Kermany, M. Goldbaum, W. Cai, C. C. Valentim, H. Liang, S. L. Baxter, A. McKeown, G. Yang, X. Wu, F. Yan et al., "Identifying medical diagnoses and treatable diseases by image-based deep learning," *Cell*, vol. 172, no. 5, pp. 1122–1131, 2018.
- [238] R. Trullo, C. Petitjean, S. Ruan, B. Dubray, D. Nie, and D. Shen, "Segmentation of organs at risk in thoracic ct images using a sharpmask architecture and conditional random fields," in *Proc. IEEE Int. Symp. Biomed. Imaging*. IEEE, 2017, pp. 1003–1006.

- [239] S. G. Armato III, G. McLennan, L. Bidaut, M. F. McNitt-Gray, C. R. Meyer, A. P. Reeves, B. Zhao, D. R. Aberle, C. I. Henschke, E. A. Hoffman *et al.*, "The lung image database consortium (lidc) and image database resource initiative (idri): a completed reference database of lung nodules on ct scans," *Med. Phys.*, vol. 38, no. 2, pp. 915–931, 2011.
- [240] A. E. Johnson, T. J. Pollard, S. J. Berkowitz, N. R. Greenbaum, M. P. Lungren, C.-y. Deng, R. G. Mark, and S. Horng, "Mimic-cxr, a de-identified publicly available database of chest radiographs with free-text reports," *Sci. Data*, vol. 6, no. 1, pp. 1–8, 2019.
- [241] K. Sirinukunwattana, D. R. Snead, and N. M. Rajpoot, "A stochastic polygons model for glandular structures in colon histology images," *IEEE Trans. Med. Imaging*, vol. 34, no. 11, pp. 2366–2378, 2015.
- [242] G. A. Sonn, S. Natarajan, D. J. Margolis, M. MacAiran, P. Lieu, J. Huang, F. J. Dorey, and L. S. Marks, "Targeted biopsy in the detection of prostate cancer using an office based magnetic resonance ultrasound fusion device," *J. Urol.*, vol. 189, no. 1, pp. 86–92, 2013.
- [243] W. Bulten, G. Litjens, H. Pinckaers, P. Ström, M. Eklund, K. Kartasalo, M. Demkin, and S. Dane, "The panda challenge: Prostate cancer grade assessment using the gleason grading system," *MICCAI challenge*, 2020.
- [244] G. Litjens, R. Toth, W. van de Ven, C. Hoeks, S. Kerkstra, B. van Ginneken, G. Vincent, G. Guillard, N. Birbeck, J. Zhang *et al.*, "Evaluation of prostate segmentation algorithms for mri: the promise12 challenge," *Med. Image Anal.*, vol. 18, no. 2, pp. 359–373, 2014.
- [245] Z. Tian, L. Liu, Z. Zhang, and B. Fei, "Superpixel-based segmentation for 3d prostate mr images," *IEEE Trans. Med. Imaging*, vol. 35, no. 3, pp. 791–801, 2015.
- [246] E. Arvaniti, K. S. Fricker, M. Moret, N. Rupp, T. Hermanns, C. Fankhauser, N. Wey, P. J. Wild, J. H. Rueschoff, and M. Claassen, "Automated gleason grading of prostate cancer tissue microarrays via deep learning," *Scientific reports*, vol. 8, no. 1, pp. 1–11, 2018.
- [247] X. Zhuang, "Multivariate mixture model for cardiac segmentation from multi-sequence mri," in *Proc. Int. Conf. Med. Image Comput. Comput.-Assisted Intervention*. Springer, 2016, pp. 581–588.
- [248] A. Andreopoulos and J. K. Tsotsos, "Efficient and generalizable statistical models of shape and appearance for analysis of cardiac mri," *Med. Image Anal.*, vol. 12, no. 3, pp. 335–357, 2008.
- [249] Z. Xiong, Q. Xia, Z. Hu, N. Huang, C. Bian, Y. Zheng, S. Vesal, N. Ravikumar, A. Maier, X. Yang *et al.*, "A global benchmark of algorithms for segmenting the left atrium from late gadolinium-enhanced cardiac magnetic resonance imaging," *Med. Image Anal.*, vol. 67, p. 101832, 2021.
- [250] J. Sivaswamy, S. Krishnadas, G. D. Joshi, M. Jain, and A. U. S. Tabish, "Drishti-gs: Retinal image dataset for optic nerve head (onh) segmentation," in *Proc. IEEE Int. Symp. Biomed. Imaging*. IEEE, 2014, pp. 53–56.
- [251] J. I. Orlando, H. Fu, J. B. Breda, K. van Keer, D. R. Bathula, A. Diaz-Pinto, R. Fang, P.-A. Heng, J. Kim, J. Lee *et al.*, "Refuge challenge: A unified framework for evaluating automated methods for glaucoma assessment from fundus photographs," *Med. Image Anal.*, vol. 59, p. 101570, 2020.
- [252] "Diabetic retinopathy detection challenge," <https://www.kaggle.com/c/diabetic-retinopathy-detection>, 2015.
- [253] H. Bogunović, F. Venhuizen, S. Klimescha, S. Apostolopoulos, A. Bab-Hadiashar, U. Bagci, M. F. Beg, L. Bekalo, Q. Chen, C. Ciller *et al.*, "Retouch: the retinal oct fluid detection and segmentation benchmark and challenge," *IEEE Trans. Med. Imaging*, vol. 38, no. 8, pp. 1858–1874, 2019.
- [254] Z. Zhang, F. S. Yin, J. Liu, W. K. Wong, N. M. Tan, B. H. Lee, J. Cheng, and T. Y. Wong, "Origa-light: An online retinal fundus image database for glaucoma analysis and research," in *2010 Annual international conference of the IEEE engineering in medicine and biology*. IEEE, 2010, pp. 3065–3068.
- [255] S. Farsiu, S. J. Chiu, R. V. O'Connell, F. A. Folgar, E. Yuan, J. A. Izatt, C. A. Toth, A.-R. E. D. S. . A. S. D. O. C. T. S. Group *et al.*, "Quantitative classification of eyes with and without intermediate age-related macular degeneration using optical coherence tomography," *Ophthalmology*, vol. 121, no. 1, pp. 162–172, 2014.
- [256] H. Fang, F. Li, H. Fu, X. Sun, X. Cao, F. Lin, J. Son, S. Kim, G. Queller, S. Matta *et al.*, "Adam challenge: Detecting age-related macular degeneration from fundus images," *IEEE Trans. Med. Imaging*, 2022.
- [257] H. Fu, F. Li, J. I. Orlando, H. Bogunovic, X. Sun, J. Liao, Y. Xu, S. Zhang, and X. Zhang, "Palm: Pathologic myopia challenge," *IEEE Dataport*, 2019.
- [258] S. Hajeb Mohammad Alipour, H. Rabbani, and M. R. Akhlaghi, "Diabetic retinopathy grading by digital curvelet transform," *Comput. Math. Methods Med.*, vol. 2012, 2012.
- [259] E. Decencière, X. Zhang, G. Cazuguel, B. Lay, B. Cochener, C. Trone, P. Gain, R. Ordóñez, P. Massin, A. Erginay *et al.*, "Feedback on a publicly distributed image database: the messidor database," *Image Anal. Stereol.*, vol. 33, no. 3, pp. 231–234, 2014.
- [260] P. Tschandl, C. Rosendahl, and H. Kittler, "The ham10000 dataset, a large collection of multi-source dermatoscopic images of common pigmented skin lesions," *Sci. Data*, vol. 5, no. 1, pp. 1–9, 2018.
- [261] D. Gutman, N. C. Codella, E. Celebi, B. Helba, M. Marchetti, N. Mishra, and A. Halpern, "Skin lesion analysis toward melanoma detection: A challenge at the international symposium on biomedical imaging (isbi) 2016, hosted by the international skin imaging collaboration (isic)," *arXiv preprint arXiv:1605.01397*, 2016.
- [262] N. C. Codella, D. Gutman, M. E. Celebi, B. Helba, M. A. Marchetti, S. W. Dusza, A. Kalloo, K. Liopyris, N. Mishra, H. Kittler *et al.*, "Skin lesion analysis toward melanoma detection: A challenge at the 2017 international symposium on biomedical imaging (isbi), hosted by the international skin imaging collaboration (isic)," in *Proc. IEEE Int. Symp. Biomed. Imaging*. IEEE, 2018, pp. 168–172.
- [263] M. A. A. Milton, "Automated skin lesion classification using ensemble of deep neural networks in isic 2018: Skin lesion analysis towards melanoma detection challenge," *arXiv preprint arXiv:1901.10802*, 2019.
- [264] S. S. Halabi, L. M. Prevedello, J. Kalpathy-Cramer, A. B. Mamonov, A. Bilbily, M. Cicero, I. Pan, L. A. Pereira, R. T. Sousa, N. Abdala *et al.*, "The rsna pediatric bone age machine learning challenge," *Radiology*, vol. 290, no. 2, p. 498, 2019.
- [265] J. N. Kather, J. Krisam, P. Charoentong, T. Luedde, E. Herpel, C.-A. Weis, T. Gaiser, A. Marx, N. A. Valous, D. Ferber *et al.*, "Predicting survival from colorectal cancer histology slides using deep learning: A retrospective multicenter study," *PLoS Med.*, vol. 16, no. 1, p. e1002730, 2019.
- [266] K. Sirinukunwattana, S. E. A. Raza, Y.-W. Tsang, D. R. Snead, I. A. Cree, and N. M. Rajpoot, "Locality sensitive deep learning for detection and classification of nuclei in routine colon cancer histology images," *IEEE Trans. Med. Imaging*, vol. 35, no. 5, pp. 1196–1206, 2016.
- [267] O. Bernard, A. Lalande, C. Zotti, F. Cervenansky, X. Yang, P.-A. Heng, I. Cetin, K. Lekadir, O. Camara, M. A. G. Ballester *et al.*, "Deep learning techniques for automatic mri cardiac multi-structures segmentation and diagnosis: is the problem solved?" *IEEE Trans. Med. Imaging*, vol. 37, no. 11, pp. 2514–2525, 2018.
- [268] A. E. Kavur, N. S. Gezer, M. Barış, S. Aslan, P.-H. Conze, V. Groza, D. D. Pham, S. Chatterjee, P. Ernst, S. Özkan *et al.*, "Chaos challenge-combined (ct-mrj) healthy abdominal organ segmentation," *Med. Image Anal.*, vol. 69, p. 101950, 2021.
- [269] G. Aresta, T. Araújo, S. Kwok, S. S. Chennamsetty, M. Safwan, V. Alex, B. Marami, M. Prastawa, M. Chan, M. Donovan *et al.*, "Bach: Grand challenge on breast cancer histology images," *Med. Image Anal.*, vol. 56, pp. 122–139, 2019.
- [270] N. Wu, J. Phang, J. Park, Y. Shen, S. G. Kim, L. Heacock, L. Moy, K. Cho, and K. J. Geras, "The nyu breast cancer screening dataset v1.0," *New York Univ., New York, NY, USA, Tech. Rep.*, 2019.
- [271] R. S. Lee, F. Gimenez, A. Hoogi, K. K. Miyake, M. Gorovoy, and D. L. Rubin, "A curated mammography data set for use in computer-aided detection and diagnosis research," *Sci. Data*, vol. 4, no. 1, pp. 1–9, 2017.
- [272] J. Suckling, J. Parker, D. Dance, S. Astley, I. Hutt, C. Boggis, I. Ricketts, E. Stamatakis, N. Cerneaz, S. Kok *et al.*, "Mammographic image analysis society (mias) database v1.21," 2015.
- [273] M. A. Troester, X. Sun, E. H. Allott, J. Geradts, S. M. Cohen, C.-K. Tse, E. L. Kirk, L. B. Thorne, M. Mathews, Y. Li *et al.*, "Racial differences in pam50 subtypes in the carolina breast cancer study," *J. Natl. Cancer Inst.*, vol. 110, no. 2, pp. 176–182, 2018.
- [274] P. Naylor, M. Laé, F. Reyat, and T. Walter, "Segmentation of nuclei

- in histopathology images by deep regression of the distance map," *IEEE Trans. Med. Imaging*, vol. 38, no. 2, pp. 448–459, 2018.
- [275] M. Veta, Y. J. Heng, N. Stathonikos, B. E. Bejnordi, F. Beca, T. Wollmann, K. Rohr, M. A. Shah, D. Wang, M. Rousson *et al.*, "Predicting breast tumor proliferation from whole-slide images: the tucap16 challenge," *Med. Image Anal.*, vol. 54, pp. 111–121, 2019.
- [276] R. Ludovic, R. Daniel, L. Nicolas, K. Maria, I. Humayun, K. Jacques, C. Frédérique, G. Catherine *et al.*, "Mitosis detection in breast cancer histological images an icpr 2012 contest," *J. Pathol. Inform.*, vol. 4, no. 1, p. 8, 2013.
- [277] "Icpr 2014 mitosis detection dataset." <https://mitos-atypia-14.grand-challenge.org/home/>.
- [278] M. Kandemir, C. Zhang, and F. A. Hamprecht, "Empowering multiple instance histopathology cancer diagnosis by cell graphs," in *Proc. Int. Conf. Med. Image Comput. Comput.-Assisted Intervention*. Springer, 2014, pp. 228–235.
- [279] M. Maška, V. Ulman, D. Svoboda, P. Matula, P. Matula, C. Ederra, A. Urbíola, T. España, S. Venkatesan, D. M. Balak *et al.*, "A benchmark for comparison of cell tracking algorithms," *Bioinformatics*, vol. 30, no. 11, pp. 1609–1617, 2014.
- [280] Q. D. Vu, S. Graham, T. Kurc, M. N. N. To, M. Shaban, T. Qaiser, N. A. Koohbanani, S. A. Khurram, J. Kalpathy-Cramer, T. Zhao *et al.*, "Methods for segmentation and classification of digital microscopy tissue images," *Front. Bioeng. Biotechnol.*, p. 53, 2019.
- [281] K. Yan, X. Wang, L. Lu, and R. M. Summers, "Deeplesion: automated mining of large-scale lesion annotations and universal lesion detection with deep learning," *J. Med. Imaging*, vol. 5, no. 3, p. 036501, 2018.
- [282] A. Keikhosravi, B. Li, Y. Liu, M. W. Conklin, A. G. Loeffler, and K. W. Eliceiri, "Non-disruptive collagen characterization in clinical histopathology using cross-modality image synthesis," *Communications biology*, vol. 3, no. 1, pp. 1–12, 2020.
- [283] N. Kumar, R. Verma, S. Sharma, S. Bhargava, A. Vahadane, and A. Sethi, "A dataset and a technique for generalized nuclear segmentation for computational pathology," *IEEE Trans. Med. Imaging*, vol. 36, no. 7, pp. 1550–1560, 2017.
- [284] E. Gibson, F. Giganti, Y. Hu, E. Bonmati, S. Bandula, K. Gurusamy, B. Davidson, S. P. Pereira, M. J. Clarkson, and D. C. Barratt, "Automatic multi-organ segmentation on abdominal ct with dense v-networks," *IEEE Trans. Med. Imaging*, vol. 37, no. 8, pp. 1822–1834, 2018.
- [285] E. Gibson, F. Giganti, Y. Hu, E. Bon-Mati, S. Bandula, K. Gurusamy, B. Davidson, S. P. Pereira, M. J. Clarkson, and D. C. Barratt, "Multi-organ abdominal ct reference standard segmentations," *This data set was developed as part of independent research supported by Cancer Research UK (Multidisciplinary C28070/A19985) and the National Institute for Health Research UCL/UCL Hospitals Biomedical Research Centre*, 2018.
- [286] H. R. Roth, L. Lu, A. Farag, H.-C. Shin, J. Liu, E. B. Turkbey, and R. M. Summers, "Deeporgan: Multi-level deep convolutional networks for automated pancreas segmentation," in *Proc. Int. Conf. Med. Image Comput. Comput.-Assisted Intervention*. Springer, 2015, pp. 556–564.
- [287] B. Rister, D. Yi, K. Shivakumar, T. Nobashi, and D. L. Rubin, "Ct-org, a new dataset for multiple organ segmentation in computed tomography," *Sci. Data*, vol. 7, no. 1, pp. 1–9, 2020.
- [288] M. M. Oken, W. G. Hocking, P. A. Kvale, G. L. Andriole, S. S. Buys, T. R. Church, E. D. Crawford, M. N. Fouad, C. Isaacs, D. J. Reding *et al.*, "Screening by chest radiograph and lung cancer mortality: the prostate, lung, colorectal, and ovarian (plco) randomized trial," *Jama*, vol. 306, no. 17, pp. 1865–1873, 2011.
- [289] M. Aubreville, C. Bertram, M. Veta, R. Klopfeisch, N. Stathonikos, K. Breininger, N. ter Hoeve, F. Ciompi, and A. Maier, "Mitosis domain generalization challenge," in *Proc. Int. Conf. Med. Image Comput. Comput.-Assisted Intervention*, 2021, pp. 1–15.
- [290] H. Su, X. Shi, J. Cai, and L. Yang, "Local and global consistency regularized mean teacher for semi-supervised nuclei classification," in *Proc. Int. Conf. Med. Image Comput. Comput.-Assisted Intervention*. Springer, 2019, pp. 559–567.
- [291] N. Marini, S. Otálora, H. Müller, and M. Atzori, "Semi-supervised training of deep convolutional neural networks with heterogeneous data and few local annotations: An experiment on prostate histopathology image classification," *Med. Image Anal.*, vol. 73, p. 102165, 2021.
- [292] J. Wen, E. Varol, A. Sotiras, Z. Yang, G. B. Chand, G. Erus, H. Shou, A. Abdulkadir, G. Hwang, D. B. Dwyer *et al.*, "Multi-scale semi-supervised clustering of brain images: Deriving disease subtypes," *Med. Image Anal.*, vol. 75, p. 102304, 2022.
- [293] S. Sedai, B. Antony, R. Rai, K. Jones, H. Ishikawa, J. Schuman, W. Gadi, and R. Garnavi, "Uncertainty guided semi-supervised segmentation of retinal layers in oct images," in *Proc. Int. Conf. Med. Image Comput. Comput.-Assisted Intervention*. Springer, 2019, pp. 282–290.
- [294] Y. Xie, J. Zhang, Z. Liao, J. Verjans, C. Shen, and Y. Xia, "Pairwise relation learning for semi-supervised gland segmentation," in *Proc. Int. Conf. Med. Image Comput. Comput.-Assisted Intervention*. Springer, 2020, pp. 417–427.
- [295] Y. Zhou, H. Chen, H. Lin, and P.-A. Heng, "Deep semi-supervised knowledge distillation for overlapping cervical cell instance segmentation," in *Proc. Int. Conf. Med. Image Comput. Comput.-Assisted Intervention*. Springer, 2020, pp. 521–531.
- [296] Y. Li, J. Chen, X. Xie, K. Ma, and Y. Zheng, "Self-loop uncertainty: A novel pseudo-label for semi-supervised medical image segmentation," in *Proc. Int. Conf. Med. Image Comput. Comput.-Assisted Intervention*. Springer, 2020, pp. 614–623.
- [297] X. Xu, T. Sanford, B. Turkbey, S. Xu, B. J. Wood, and P. Yan, "Shadow-consistent semi-supervised learning for prostate ultrasound segmentation," *IEEE Trans. Med. Imaging*, vol. 41, no. 6, pp. 1331–1345, 2021.
- [298] X. Huo, L. Xie, J. He, Z. Yang, W. Zhou, H. Li, and Q. Tian, "Atso: Asynchronous teacher-student optimization for semi-supervised image segmentation," in *Proc. IEEE Conf. Comput. Vis. Pattern Recogn.*, 2021, pp. 1235–1244.
- [299] Y. Shi, J. Zhang, T. Ling, J. Lu, Y. Zheng, Q. Yu, L. Qi, and Y. Gao, "Inconsistency-aware uncertainty estimation for semi-supervised medical image segmentation," *IEEE Trans. Med. Imaging*, vol. 41, no. 3, pp. 608–620, 2021.
- [300] X. Hu, D. Zeng, X. Xu, and Y. Shi, "Semi-supervised contrastive learning for label-efficient medical image segmentation," in *Proc. Int. Conf. Med. Image Comput. Comput.-Assisted Intervention*. Springer, 2021, pp. 481–490.
- [301] Y. Li, L. Luo, H. Lin, H. Chen, and P.-A. Heng, "Dual-consistency semi-supervised learning with uncertainty quantification for covid-19 lesion segmentation from ct images," in *Proc. Int. Conf. Med. Image Comput. Comput.-Assisted Intervention*. Springer, 2021, pp. 199–209.
- [302] F. Wu and X. Zhuang, "Minimizing estimated risks on unlabeled data: A new formulation for semi-supervised medical image segmentation," *IEEE Trans. Pattern Anal. Mach. Intell.*, 2022.
- [303] F. Gao, M. Hu, M.-E. Zhong, S. Feng, X. Tian, X. Meng, Z. Huang, M. Lv, T. Song, X. Zhang *et al.*, "Segmentation only uses sparse annotations: Unified weakly and semi-supervised learning in medical images," *Med. Image Anal.*, vol. 80, p. 102515, 2022.
- [304] Z. Cai, L. Lin, H. He, and X. Tang, "Uni4eye: Unified 2d and 3d self-supervised pre-training via masked image modeling transformer for ophthalmic image classification," in *Proc. Int. Conf. Med. Image Comput. Comput.-Assisted Intervention*. Springer, 2022, pp. 88–98.
- [305] Y. Xie, J. Zhang, Y. Xia, and Q. Wu, "Unimiss: Universal medical self-supervised learning via breaking dimensionality barrier," in *Proc. Eur. Conf. Comput. Vis.*. Springer, 2022, pp. 558–575.
- [306] W. Zhu, Q. Lou, Y. S. Vang, and X. Xie, "Deep multi-instance networks with sparse label assignment for whole mammogram classification," in *Proc. Int. Conf. Med. Image Comput. Comput.-Assisted Intervention*. Springer, 2017, pp. 603–611.
- [307] G. Patel and J. Dolz, "Weakly supervised segmentation with cross-modality equivariant constraints," *Med. Image Anal.*, vol. 77, p. 102374, 2022.
- [308] P. Chikontwe, H. J. Sung, J. Jeong, M. Kim, H. Go, S. J. Nam, and S. H. Park, "Weakly supervised segmentation on neural compressed histopathology with self-equivariant regularization," *Med. Image Anal.*, p. 102482, 2022.
- [309] B. Qi, G. Zhao, X. Wei, C. Du, C. Pan, Y. Yu, and J. Li, "Gren: graph-regularized embedding network for weakly-supervised disease localization in x-ray images," *IEEE J. Biomed. Health. Inf.*, vol. 26, no. 10, pp. 5142–5153, 2022.
- [310] Q. Meng, L. Liao, and S. Satoh, "Weakly-supervised learning with complementary heatmap for retinal disease detection," *IEEE Trans. Med. Imaging*, 2022.
- [311] X. Liu, Q. Yuan, Y. Gao, K. He, S. Wang, X. Tang, J. Tang, and D. Shen, "Weakly supervised segmentation of covid19 infection

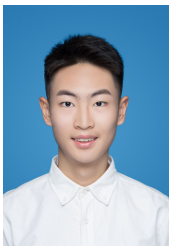
with scribble annotation on ct images," *Pattern Recognit.*, vol. 122, p. 108341, 2022.

- [312] Z. Huang, Y. Guo, N. Zhang, X. Huang, P. Decazes, S. Becker, and S. Ruan, "Multi-scale feature similarity-based weakly supervised lymphoma segmentation in pet/ct images," *Comput. Biol. Med.*, vol. 151, p. 106230, 2022.
- [313] H. Xiong, S. Liu, R. V. Sharan, E. Coiera, and S. Berkovsky, "Weak label based bayesian u-net for optic disc segmentation in fundus images," *Artificial Intelligence in Medicine*, vol. 126, p. 102261, 2022.
- [314] G. K. Mahani, R. Li, N. Evangelou, S. Sotiropoulos, P. S. Morgan, A. P. French, and X. Chen, "Bounding box based weakly supervised deep convolutional neural network for medical image segmentation using an uncertainty guided and spatially constrained loss," in *Proc. IEEE Int. Symp. Biomed. Imaging*. IEEE, 2022, pp. 1–5.
- [315] Y. Li, Y. Xue, L. Li, X. Zhang, and X. Qian, "Domain adaptive box-supervised instance segmentation network for mitosis detection," *IEEE Trans. Med. Imaging*, 2022.
- [316] W. Cai, L. Xie, W. Yang, Y. Li, Y. Gao, and T. Wang, "Dftnet: Dual-path feature transfer network for weakly supervised medical image segmentation," *IEEE/ACM Trans. Comput. Biol. Bioinform.*, 2022.



Cheng Jin (Student Member, IEEE) received his B.S. degree in Optoelectronic Information Science and Engineering from University of Electronic Science and Technology of China (UESTC). He is pursuing the Ph.D. degree with the Computer Science and Engineering Department, The Hong Kong University of Science and Technology (HKUST). His research interests include utilizing artificial intelligence (AI) algorithms for computer-aided diagnosis (CAD) systems. He serves as the Regular Reviewer of

multiple journals including Information Fusion, IEEE Transactions on Neural Networks and Learning Systems, IEEE Journal of Biomedical and Health Informatics, etc.



Zhengrui Guo (Student Member, IEEE) received his B.S. degree in Mathematics and Applied Mathematics from the Harbin Institute of Technology, China. He is currently pursuing the Ph.D. degree in Computer Science and Engineering with the School of Engineering, The Hong Kong University of Science and Technology (HKUST). His research interests include deep learning and medical image analysis.



Yi Lin is now a Ph.D. candidate at the Department of Computer Science and Engineering (CSE), Hong Kong University of Science and Technology (HKUST). Before that, he was a research engineer in Jarvis Lab at Tencent. He received his M.S. degree and B.S. degree from Huazhong University of Science and Technology (HUST) in 2020 and 2012, respectively. His research interests include medical image analysis and deep learning.



Luyang Luo (Member, IEEE) is a Post-doctoral Fellow at the Department of Computer Science and Engineering (CSE), Hong Kong University of Science and Technology (HKUST). He obtained his Ph.D. and B.E. in the Department of Computer Science and Engineering from The Chinese University of Hong Kong (CUHK). He has published a dozen of papers in top-tiered conferences and journals, including MICCAI, IEEE TMI, MIA, Lancet Digital Health, Radiology Artificial Intelligence, JMRI, etc. He served as a reviewer for conferences and journals including MICCAI, AAAI, ISBI, IEEE TMI, MIA, Scientific Reports, Medical Physics, JMRI, etc. His current research interest is in trustworthy machine learning for medical image analysis, focusing on fairness, debiasing, and efficiency.



Hao Chen (Senior Member, IEEE) is an Assistant Professor at the Department of Computer Science and Engineering, The Hong Kong University of Science and Technology. His interests focus on developing trustworthy artificial intelligence (AI) for healthcare. He received the Ph.D. degree from The Chinese University of Hong Kong (CUHK) in 2017. He was a postdoctoral research fellow in CUHK previously. He has 100+ publications in MICCAI, IEEE-TMI, MIA, CVPR, AAAI, Radiology, Lancet Digital Health, Nature

Machine Intelligence, JAMA, etc. He also holds a dozen of patents in AI and medical image analysis. He received several premium awards such as MICCAI Young Scientist Impact Award in 2019 and several best paper awards. He serves as the Associate Editor of multiple journals including IEEE Transactions on Neural Networks and Learning Systems, IEEE Journal of Biomedical and Health Informatics, etc.